Geometric Controls on Partially Saturated Flow through Natural Rock Fractures

by

Mampho Maoyi

12199062

UNIVERSITEIT VAN PRETORIA
UNIVERSITY OF PRETORIA
YUNIBESITHI YA PRETORIA

Submitted in accordance with the requirements for the degree

Master of Science Engineering Geology

Faculty of Natural and Agricultural Sciences

Department of Geology

University of Pretoria

Supervisor: Dr M.A. Dippenaar

April 2019

DECLARATION OF ORIGINALITY / DECLARATION ON PLAGIARISM

The ***Department of Geology (University of Pretoria)*** places great emphasis upon integrity and ethical conduct in the preparation of all written work submitted for academic evaluation. While academic staff teaches you about referencing techniques and how to avoid plagiarism, you too have a responsibility in this regard. If you are at any stage uncertain as to what is required, you should speak to your lecturer before any written work is submitted.

You are guilty of plagiarism if you copy something from another author's work (e.g. a book, an article or a website) without acknowledging the source and pass it off as your own. In effect you are stealing something that belongs to someone else. This is not only the case when you copy work word-for-word (verbatim), but also when you submit someone else's work in a slightly altered form (paraphrase) or use a line of argument without acknowledging it. You are not allowed to use work previously produced by another student. You are also not allowed to let anybody copy your work with the intention of passing if off as his/her work.

Students who commit plagiarism will not be given any credit for plagiarised work. The matter may also be referred to the Disciplinary Committee (Students) for a ruling. Plagiarism is regarded as a serious contravention of the University's rules and can lead to expulsion from the University.

The declaration which follows must accompany all written work submitted while you are a student of the ***Department of Geology (University of Pretoria)***. No written work will be accepted unless the declaration has been completed and attached.

I, the undersigned, declare that:

1. I understand what plagiarism is and am aware of the University's policy in this regard.
2. I declare that this assignment (e.g. essay, report, project, assignment, dissertation, thesis, etc) is my own original work. Where other people's work has been used (either from a printed source, Internet or any other source), this has been properly acknowledged and referenced in accordance with Departmental requirements.
3. I have not used work previously produced by another student or any other person to hand in as my own.
4. I have not allowed, and will not allow, anyone to copy my work with the intention of passing it off as his or her own work.

Full names of student: Mampho Maoyi

Student number: 12199062

Date submitted: April 2019

Topic of work: Geometric Controls on Partially Saturated Flow through Natural Rock Fractures

Signature:

Supervisor: Dr M.A. Dippenaar

ABSTRACT

Partially saturated rock fracture flow informs on groundwater recharge processes, water affecting infrastructure, and water quality deterioration. This study examines partially saturated flow through natural fractures in double porosity media. Rock samples are characterised in terms of bulk mineralogical composition, as well as its geomechanical properties including, for instance, fracture aperture and roughness, representing the overall rock mass geometry. Samples are tested at different angles of inclination, being 0°, 23°, 60°, and 90° orientation. Samples are wetted while observing inflow and outflows from the dry to wetting and to the rewetting phase conditions; calculating water budgets, linear flow velocities, and Reynolds numbers. The change in the hydraulic head and the flow of water in the different cross-sectional areas follows the Bernoulli and continuity principle. The observed flow mechanism for shale is finger flow, and the flow regime is transitional turbulent flow at low flow meter discharge rates, and turbulent rotational flow for high flow meter rates. Conversely, the flow mechanism for quartzite is film flow, while the flow regime at high and low flow meter rates are turbulent and laminar rotational flow, respectively. These flow mechanisms show fluid instabilities and rapid infiltration of water under unsaturated continuous influx conditions. Preferential flow prevails in the fracture as water exits the fracture parallel or perpendicular to the flow direction. Subsequently, water may rewet the pre-existing flow paths from the initially dry phase, form new paths, merge flow paths, or the wetting front-width increases. Inclination affects the formation of the overall flow pattern in the fractures, but not the flow rate. The aperture of the shale is smaller than that of quartzite, and the width of the aperture influences the observed flow mechanisms, as tight discontinuities are more likely to have forces counteracting free water movement, affecting the permeability. Capillary forces are significant in narrower apertures, whereas gravitational forces are prominent in quartzite. Joint roughness coefficients show that the fracture surfaces are not identical; roughness induces turbulence and accounts for flow channelling.

ACKNOWLEDGEMENTS

Since I started this journey in 2018, I have been looking forward to writing this section, because I have successfully closed another chapter of my academic career. In the past year, there has been no difference between Monday, Sunday or public holidays, only "research working days". Perseverance, resilience and having faith in God got me here.

To my supervisor, Matthys, I remember how this research conversation started on a Saturday afternoon at Eastwoods. All I can say is that great things come from geologists sharing a drink. Honestly, I do not think I would be where I am today if it was not for you encouraging me to do this. Thank you for choosing me. You have been the most supportive in this project, from sitting with me through experiments, and always reminding me that "Yes Mampho! it is supposed to be difficult". I admire your incredible work ethic and how you let me figure things out on my own, where I learnt so much by doing so. You have also taught me some valuable life lessons from the in-between pep talks. It has been a stressful journey, but I would not mind doing it again with you as my supervisor. I cannot thank you enough for all that you have done for me.

Prof. Louis, I've always wanted to tell you that a lot about you reminds me of my Dad. He is a strict, kind-hearted man, and those who do not understand him assume that he is a difficult person. With that being said, you always had an open-door policy for me despite your busy schedule, thank you. I value the times I came into your office and asked you questions, and you would pose thought provoking questions to me about the research. A lot of those questions you asked, which I did not have answers for by then and your advice has helped me a great deal. You shared relevant literature with me, and many of your books are filling up my parent's house. I will certainly miss the moments when I walked into Rocklab and Dr Chen would treat me like royalty, because I would always say "Prof. Louis sent me" – the reach of your name has really worked in my favour. Hopefully, we will work on more projects together. I do not want to miss the chance of countlessly knocking on your office door before you retire. Thank you for your selfless assistance, I truly appreciate it.

Other comments will follow at Eastwoods, where all of this started alongside Brendon. Dr Jones, thank you for having suggestions regarding the project and sharing relevant literature with me. I believe we are yet to co-author papers together. I'd also like to

thank Luke Brouwers for always giving me advice, even though you have never met me in your entire life, that goes a long way for me.

My deepest gratitude goes out to my amazing family. Mom and Dad, you always support me in everything that I do, and I do not think that I would be where I am in life if it was not for your principles instilled in me. I am truly blessed with you two – Ka 'nete Molimo o entse lintho tse kholo, e bile re li thabetse. Kea leboha batsoali baka! Linda, you are a brilliant academic, your opinion has always mattered to me, and thank you for always helping me. To my younger sister, thank you for always asking me when I am submitting my dissertation that somehow reminded me of what is important. I love you all.

To my closest friends, from taking me out for ice-cream when I was frustrated, or listening to me going on and on about this, I understand that it has been a long year for you guys 😊 and thank you for your patience. I appreciate that you even questioned sections of my research and your contribution. That helped me channel my thoughts clearly because for one to truly understand something, one needs to explain it in the simplest way possible, that is effective communication.

I would also like to thank the South African Water Research Commission (www.wrc.org.za) for fully funding this research through project number K5/2826.

~MOLIMO OA TSHEPAHALA!

GLOSSARY

Adhesion	The interface between two different materials, such as liquid and solid (Doe, 2001).
Aperture	The perpendicular distance separating the discontinuity walls when there is no fill (Gonzalez de Vallejo and Ferrer, 2011).
Cohesion	Water's attraction to itself (Berg, 1993; Doe, 2001).
Film flow	Used in a macroscopic sense, to include both true films on topographic maxima of fracture surfaces, and pendular, capillary water occupying topographic minima (Tokunaga and Wan, 2000).
Finger-tip	The leading edge of a finger that consists of a coherent body of fluid, fully spanning the fracture aperture (Nicholl et al., 1993).
Flow Mechanism	Fingers or films (Nicholl 1993; Dippenaar and Van Rooy, 2016).
Flow Pattern	Flow path sequences and wetting front along fracture.
Flow Regime	Laminar or turbulent flow (Dippenaar and Van Rooy, 2016).
Fracture	Refers to any separation in a large body of solid earth materials, irrespective of the geological origin of the separation (i.e. joint, fault, bedding planes or shear zones), occurring within and interacting with intact rock material (Dippenaar and Van Rooy, 2016).
Gravity-Driven Fingers	Preferential flow of fluids along a fracture in the direction of gravitational gradient (Nicholl et al., 1993).
Lateral flow	Perpendicular to flow direction.
Longitudinal flow	Parallel to flow direction.
Parallel plate	Two glass plates separated by a uniform aperture to idealise a fracture aperture.
Preferential flow	Focusing of flow into narrow channels (Su, 1999).
Tortuosity	Characterizes [sic] the ratio of the effective path length connecting two locations in porous media to the geometric distance (Cherubini et al., 2012).
Transparent natural replica	Scans that produce a surface and contour profile or epoxy casts made from a silicone mold to idealise natural rock fractures with the roughness characteristics (Su, 1999).
Wettability	The response evinced when a liquid is brought into contact with a solid surface initially in contact with a gas or another liquid (Doe, 2001).

Contents

List of Figures

List of Tables

List of symbols

Symbols	Description	Units
a	Average maximum amplitude	[L]
A	Cross-sectional area	[L^2]
B	Breadth	[L]
C	Constant value	[-/-]
D	Average spacing between parallel fractures	[L]
D_h	Hydraulic diameter	[L]
e	Average effective width of fractures	[L]
e_h	Hydraulic aperture	[L]
g	Gravitational acceleration	[L/T^2]
h	Height	[L]
JRC_0	Laboratory scale roughness	[-/-]
K	Hydraulic conductivity	[L/T]
k	Maximum roughness amplitude	[L]
K_{sat}	Saturated hydraulic conductivity	[L/T]
l	In-situ scale length	[L]
L	Length	[L]
l_f	Length of fracture	[L]
l_0	Laboratory scale length	[L]
M_c	Mass of container	[M]
M_{cds}	Mass of container and oven dry specimen	[M]
M_{cms}	Mass of container and moist specimen	[M]
m_h	Mechanical aperture	[L]
M_s	Mass of over dry specimen	[M]
M_w	Mass of water	[M]
n	Porosity	[%]
P	Wetted fracture region	[L]

Q	Discharge/ volumetric flow rate	[L^3/T]
r	Radius	[L]
R_e	Reynolds number	[-/-]
S_w	Degree of saturation	[%]
t	Time	[T]
V_b	Bulk Volume	[L^3]
V_p	Volume of pores (other than fractures)	[L^3]
V_T	Total volume	[L^3]
V_V	Volume of voids	[L^3]
V_w	Volume of water	[L^3]
W	Aperture width	[L]
w	Fracture width	[L]
Δh	Change in hydraulic head	[L]
θ	Moisture/ water content	[%]
μ	Dynamic viscosity	[M/LT]
ρ	Density	[M/L^3]
ρ_B	Bulk dry density	[M/L^3]
φ	Matrix porosity	[-/-]
φ_f	Fracture porosity	[%]

L-Length; M- Mass; T- Time.

Chapter 1 Introduction

1.1. Background

The unsaturated zone is defined as the zone between the ground level and the water table, where fractured rock may be directly exposed to the land surface (e.g. outcrops), or underlie low to high permeability soils. Unsaturated zone conditions correlate with partially saturated conditions, ranging between dry and wet cycles in the ground (Dippenaar and Van Rooy, 2018). Under wet ground conditions, water is an eroding agent that may affect the integrity of built structures, induce rock falls or slope failures, which deteriorate working environments, posing a threat to workers' safety (Xu et al., 2015). This is due to the partial saturation in the vadose zone, which may lead to the easy transmission of water through connected fractures and storage of water in the pore spaces within the matrix.

The applications of fracture flow are vast, and a few examples are provided to put the research question at hand in context:

- The Haizhou open-pit coal mine, located in the Liaoning Province in north-eastern China, is a typical example of recurring slope failures. More than 90 landslides have occurred since the mine was still in production and a few years thereafter (1953-2009). Recent work by Bo et al. (2019) has identified possible landslides posing a great risk to the safe operation of the national mine park to date. The possible landslides are mainly linked to the rainfall intensity and the fault fracture zone affecting the slope stability. As the rainfall intensity increases, infiltration rates into the rock mass increase, with the fractures providing the easiest flow paths, therefore, weakening the stability of the rock slopes.
- Storage of hazardous liquids or waste underground poses a risk of deteriorating the quality of water. A hydrogeological model was developed for the Singapore rock cavern project (underground liquid hydrocarbon storage facility), by means of which to reduce the risks associated with water leakage on the site. The semi-analytical method for anisotropic permeability model idealised fractures as parallel plates, where it also assumed that the solid matrix is impermeable, where seepage through the fracture is laminar, and the fracture aperture is uniform (Xu et al., 2015). Waste is normally stored in rocks that have low

permeabilities. However, fractures present in the rock mass may alter the permeability of the rock mass and provide pathways for contaminant migration in these repositories.

- Underground excavations, such as tunnelling, are susceptible to large water inflows from extremely fractured saturated rocks (Freeze and Cherry, 1979). The Simplon Tunnel is a railway link that runs through the Swiss-Italian Alps. During the construction of this tunnel, water inflow rates of 18 000 *l*/m and 6300 *l*/m at different sites in the tunnel were encountered in fractured marble. As a result, the site had to be dewatered, which has had economic implications, by also delaying the project time (National Research Council, 1996).
- Municipal water supply in Hermanus South Africa is increased through the abstraction of groundwater from the Gateway well field. The water is abstracted from four boreholes, located in the Peninsula aquifers, composed of a complex fault system and fractured rocks. Due to the location of the aquifer from the coastline, the impact of saline intrusion into the well is assessed using the *dependent flow model*. The results indicate that fracture apertures of less than 1 mm have no major impact on the groundwater flow quality. However, fractures with greater apertures may give rise of salinity in the well. The accuracy of this model is still questionable, because the fracture planes along the fault incorporated into the model are hypothesised and simplified. Further investigation of this work is also recommended by the authors (Von Scherenberg and Seyler, 2012), as the complex fracture networks and maximum apertures are still unknown. Moreover, Pearce et al. (2014) have noted that over abstraction may lead to saline intrusion, which will have long-term effects on the water quality in the area.

Generally, these engineering applications are related to highly consolidated sedimentary rocks, or hard crystalline rocks, with low permeabilities, with fluid flow primarily occurring through fractures (Singh et al., 2016). These examples reiterate the complexity of the vadose zone. This includes variable moisture contents, depending on the infiltration rates, and the hydraulic behaviour of the rock mass; the rapid inflow of water into rock mass lowering effective stresses, and increasing the pore water pressures (Gattinoni et al., 2009).

The parallel plate model is often used to idealise natural rock fractures, assuming that rocks are impermeable, and fractures present in the medium are smooth. Transparent replicas of natural fractures have been used to investigate the effects of roughness on fracture flow. The material properties of transparent replicas are impermeable, influencing the surface wettability of the fracture surfaces. In addition to this, small-scale surface roughness effects cannot be reproduced on the replica models (Su, 1999). Even so, these studies, including numerical models, have provided a useful starting point into understanding flow behaviour in fractures. The intricacy of natural fractured rocks arises from the geological history of rocks; which includes the mineralogical composition, porosity, anisotropy, heterogeneity, stress regimes and degree of weathering (Gonzalez de Vallejo and Ferrer, 2011).

Advancing in this research field helps with the design quantification of developments in disciplines such as construction, engineering geology, hydrogeology and geotechnical engineering.

1.2. Aims

The problems associated with unsaturated fracture flow are well-noted, however, the fundamental principles are still poorly understood. Furthermore, literature is sparse on the topic of flow in natural rock fractures under unsaturated conditions, and also lacking in evaluating the basic inter-relationships between the parallel plate model, natural rock fractures, and their transparent replicas in unsaturated conditions. The aim of this study is to investigate the flow behaviour of a single natural fracture and its geometric controls under controlled laboratory conditions.

1.3. Objectives

The objectives of this study are to:

- Observe flow through natural rock fractures in a controlled physical experiment
- Relate joint geometry (aperture; roughness; inclination/dip) to observed flow and quantified flow rates
- Contribute to knowledge gaps on the influence of joint geometry on partially saturated flow through natural rock fractures.

1.4. Dissertation Structure

Chapter 1- Introduction

This chapter presents the background, aims and objectives of this study.

Chapter 2- Literature Review

Theoretical aspects of the work undertaken are presented, as well as previous work which has been used to inform this study. This section is provided for the reader to gain an understanding of partially saturated flow, flow regimes and mechanisms and controls on flow conditions.

Chapter 3- Materials and Methods

The model preparation, experimental set-up, experimental procedure and the data acquisition for this study is described and discussed.

Chapter 4- Results: Visual Observations

This chapter presents the experimental flow observations from the falling head permeability test for each sample. The observed fluid behaviour in each single natural rock fracture are examined using appropriate snapshots from live footage of experiments.

Chapter 5- Results: Quantitative Data

This chapter presents the quantitative data, tabulated and in a graphical manner from the falling head permeability test. This includes the hydraulic head, volume, average linear velocities, discharge rates, calculated hydraulic conductivities, and moisture content data for each sample.

Chapter 6- Results: Composition and Geometry

This chapter presents the bulk composition of the samples, calculated porosity, determination of flow regimes and the joint roughness coefficients. In addition to this, the last section of this chapter gives an overall summary of the obtained results for each rock sample.

Chapter 7- Discussion

This chapter analyses and discusses the significance of the results. The results are also explained within the context of the relevant literature.

Chapter 8- Conclusion

This chapter presents the assumptions, limitations, summary, main findings, and concluding remarks of the study.

Chapter 2 Literature Review

2.1. Partially Saturated Fracture Flow

The flow behaviour within the rock mass (i.e. intact rock and fractures) in the unsaturated zone is affected by many parameters, namely fluid retention, wetting front instability, capillarity, gravity and viscous forces (Glass et al., 1995). Fitts (2002) has asserted that water in the unsaturated zone flows under the same physical principles that have been outlined for saturated flow. Kovács (1981) meanwhile noted that unsaturated flow occurs above the water table, where the atmospheric pressure is higher than the water pressure due to adhesion. As the moisture content decreases, the pore water pressures decrease and adhesion dominates. However, in unsaturated fractures, adhesion is not a major factor, because there is a smaller surface area as compared to a complete matrix, therefore infiltration is more rapid due to channel flow. This theory is explained by Dippenaar et al. (2014), namely that flow in fractures is faster, because water moves easier at higher velocities in comparison to porous flow.

Dippenaar and Van Rooy (2018) inferred different flow scenarios at partially saturated conditions in the vadose zone. These scenarios include: (a) normal perching; (b) capillary-barrier perching; (c) imbibition; (d) shallow interflow; (e) percolation; and (f) unsaturated fracture flow (Figure 2-1a). Dippenaar and Van Rooy (2018) expanded upon an hypothesis from the National Research Council (2001) illustrated in Figure 2-1b, namely that a major issue in examining the unsaturated zone is estimating fluid flux from the land surface to the water table. The issues surrounding this are still unclear, as preferential flow is a result of heterogeneities, flow instability, or imbibition into the rock matrix.

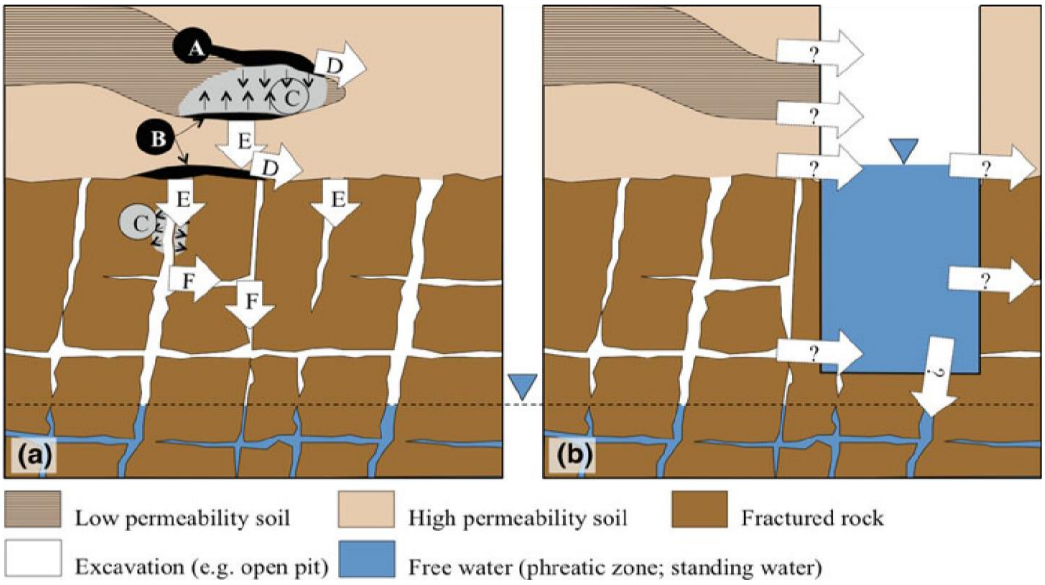

Figure 2-1: (a) Proposed occurrence of water at partially saturated state in the vadose zone, and (b) the uncertainty in apportioning the source of water flooding a hypothetical excavation with potential new flow paths indicated (Dippenaar and Van Rooy, 2018).

According to Glass and Nicholl (1996), fracture flow in rock mass occurs when the flux exceeds the hydraulic conductivity of the unsaturated matrix, resulting in either local heterogeneities diverting water into the fracture or ponded infiltration. Pruess (1999) stated that matrix imbibition is reduced by preferential flow paths, as opposed to water flowing in a spatially uniform sheet down the fracture plane. Cheng et al. (2015) have asserted that fractures can increase imbibition in sedimentary rocks by surface spreading and capillary action in unsaturated conditions. Torsaeter and Silseth (1985) meanwhile define imbibition as a spontaneous influx of a preferentially wetting fluid into a porous medium by capillary forces. Montazer and Wilson (1984) showed that hysteresis is primarily dependent on the rate of inflow into the rock and it is more effective when there is rapid influx into the matrix, because this increases the entrapped air.

The capillary model (Richard, 1931) proposed that water infiltrates the smaller pores first. When the fractured rock approached saturation, the water is then transmitted through the fracture and large pores. Wang and Narasimhan (1985) extended the capillary model for fractured rock. The authors support the aforementioned conditions for the capillary model and added that capillary bridges in the fracture zone will retain the water. This implies that flow will only occur between the matrix and that fractures will act as flow barriers within the rock mass (Wang and Narasimhan, 1993). Montazer

and Wilson (1984) explained that capillary barriers in the vadose zone occur when fine pores overlie coarser pores or fractures.

As stated by Montazer and Wilson (1984), when water infiltrates fractured porous media, the natural moisture content will regulate the easiest pathways for water flow. Furthermore, the change in moisture content with respect to the change in pressure head defines the moisture capacity of a medium. If the moisture capacity of the fracture is lower than that of the matrix, then large transient fluxes are needed at the boundary to initiate fracture flow. Moisture content can be related to the saturation, porosity and the hydraulic conductivity (Equations 2.2-2.6 e.g., Dippenaar et al. 2014). This revolves around the concept that, as more water occupies the pores spaces, there is a change in the moisture content and degree of saturation in the medium. Consequently, the hydraulic conductivity increases until its maximum is encountered at saturation (Fitts, 2002; Dippenaar et al., 2014).

$$\theta = \frac{V_w}{V_T} \tag{2.2}$$

$$S_w = \frac{V_w}{V_v} \tag{2.3}$$

$$K \rightarrow K_{sat} \tag{2.4}$$

$$S_w = 1 \tag{2.5}$$

$$\rightarrow \theta = n \tag{2.6}$$

2.2. Surface Wettability

Wettability refers to a fluid that spreads on the solid surface in the presence of another fluid or gas. When this occurs, three scenarios may arise as follows (Berg, 1993):

(1) The liquid may spread along the solid surface, where the mass of the liquid will determine the flow mechanism (e.g. films); or
(2) As equilibrium is achieved between the liquid, gas and solid, a three-phase interface with a contact angle is formed; or
(3) There is no interaction between the liquid and surface.

Doe (2001) has stated that the contact angle between the liquid and solid surface has an influence on the wetting properties of the fracture surface (Figure 2-2). At a contact angle of 180˚, there is cohesion between the water molecules and the flow mechanism is described as drops or rivulets. The critical contact angle occurs at 90˚, which distinguishes between the capillary depression and the capillary rise, where cohesion is greater than adhesion. At zero degrees (0˚), the liquid spreads on the solid surface as a film and adhesion is greater than cohesion. Subsequently, the liquid may imbibe into the smaller pore spaces (Doe, 2001). Carillo et al. (2000) suggested that the contact angle may also be altered by the contact time between solid surface and the fluid. Gates (2018) has elaborated that the stronger the attraction of the fluid to the solid surface, the greater the spreading of the fluid will be across the solid surface and the lower the contact angle.

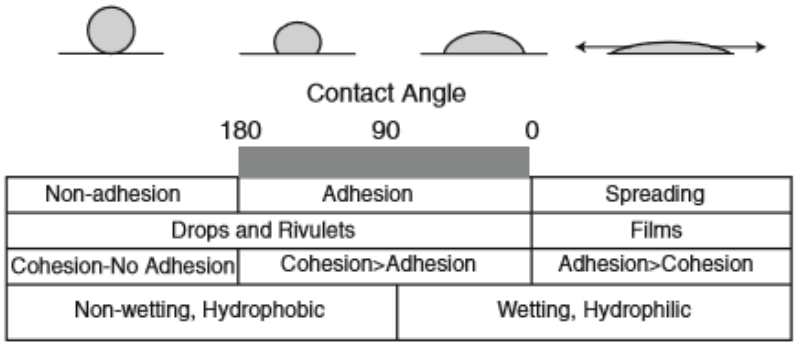

Figure 2-2: Relationship between adhesion, cohesion, wetting, spreading and contact angle (Doe, 2001).

2.3. Flow Mechanisms

Brouwers and Dippenaar (2018) affirmed that wetting and drying cycles of the ground due to infiltration induces a change in natural systems. As water enters the fractures in unsaturated conditions, it will either supersede the air phase or air will reinvade as the water drains (Nicholl and Glass, 2005). Indraratna and Ranjith (2001) classified the relationship between water and air through single fractures or macropores as single-phase flow, two-phase flow, and fully saturated water flow. Jones et al. (2018a) expanded this in an experiment aimed at assessing flow mechanisms for the unsaturated state for vertical and horizontal fractures. The authors inferred the different flow scenarios and flow phases (Figure 2-3). They concluded that full

saturation is not reached in the vertical fracture despite influx. On the other hand, full saturation was reached in the horizontal fracture.

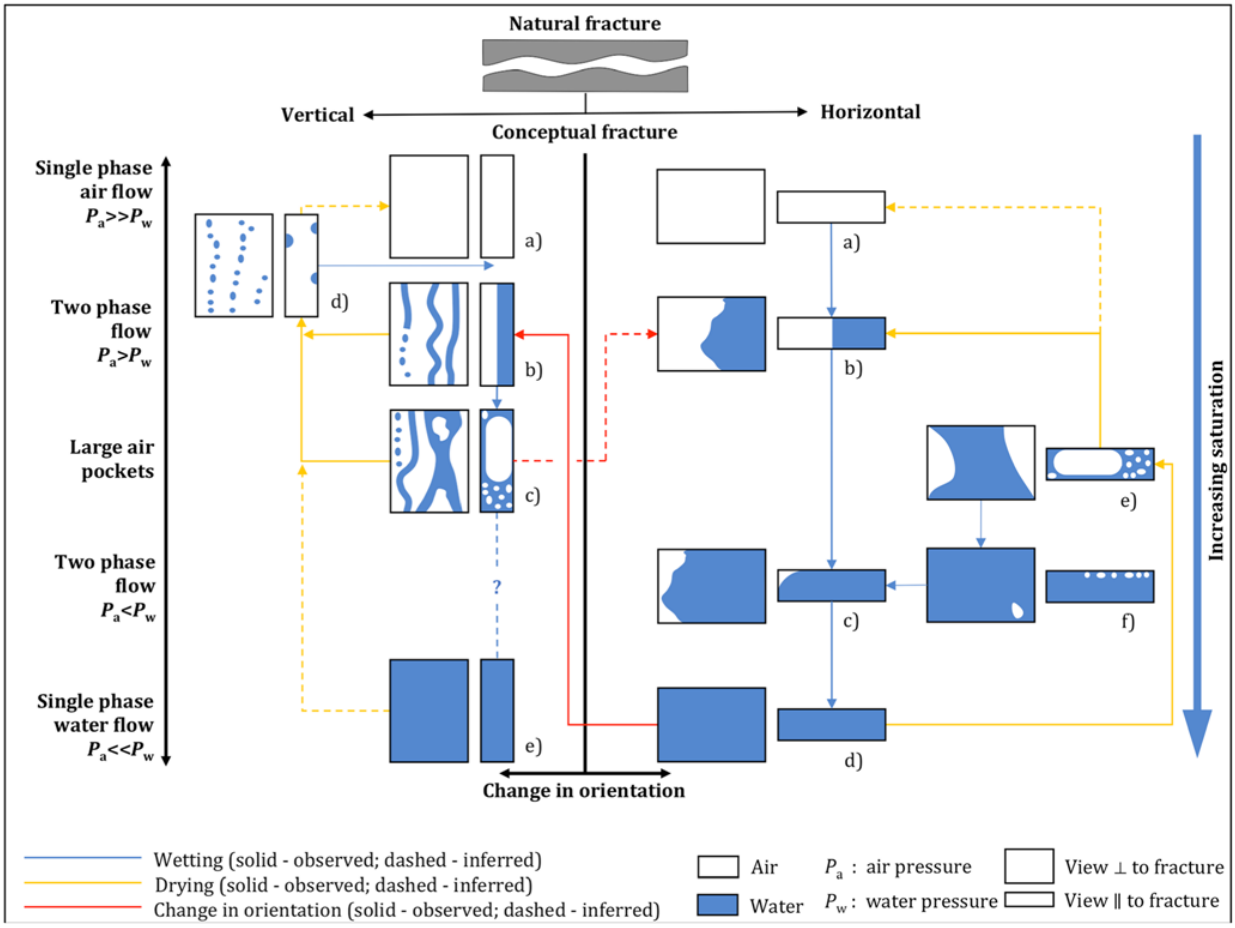

Figure 2-3:Flow relations observed during the smooth parallel plate tests (a) initially dry, (b) upon wetting, (c) higher influxes, (d) drying interval, (e) full saturation (Jones et al., 2018a).

Preferential flow paths spread on fracture surfaces as fluid fingers or free-surface fluid films (Dragila and Weisbrod, 2003). Nicholl et al. (1993) addressed gravity-driven flow instabilities in an initially wet, unsaturated, rough-walled fracture. The results indicated that in infiltration events, fluid instabilities occurred as the coherent initial front of fluid broke up into individual fingers as it moved down a gradient. Moreover, the observed fingers were faster, longer, narrower, and more structurally complicated than in the initially dry fracture studies by Nicholl et al. (1992). Nicholl and Glass (2005) stated that gravity-driven fingers would form instantly during infiltration events into rock fractures, with variable apertures and rough surfaces. In addition to this, gravity driven fingers will depend on the initial moisture condition, that is, whether the fracture is initially dry or pre-wetted and the rate of influx. Another flow mechanism proposed by

Tokunaga & Wan (1997) occurs when a sufficient mass of water exits the fracture as films, and this flow mechanism contributes to rapid flow in fractures and in macropores under conditions of variable saturation. Furthermore, Tokunaga et al. (2000) stated that films are "a complex network of thick pendular regions that form within topographic depressions and thin films on topographic ridges". The authors regarded a film velocity of 3×10^{-7} m/s as a benchmark for fast flow on rough fracture surfaces. At this rate, water infiltrates the vadose zone up to 100 m in a decade, which is considered a short timeframe in arid and semi-arid regions. The authors also noted that the connectivity and thickness of the pendular film region plays a significant role in controlling the flow in single fractures.

2.4. Flow Regimes

According to Witkke (2014), flow is described as laminar when there is no perceptible interaction between water particles. Conversely, turbulent flow occurs when there is irregular secondary fluid movement, as a result, the water particles interact. The Reynolds equation is derived from the Navier-Stokes equations, which are the governing equations for fluid flow (Zimmerman and Bodvarrson, 1996). The Reynolds number is a dimensionless measure that relates inertial to viscous forces, aiming to infer whether flow is Darcian and laminar. Flow regimes are quantified and classified through the Reynolds equation (Equation 2.7), and values of roughly 2300 distinguish between laminar and turbulent water flow in fractures compared to a cut-off value of 10 in granular materials (Fitts 2002; Zimmerman, et al., 2004; Ranjith and Darlington, 2007). Zhang et al. (2013) explained that the flow regime changes due to increasing or high flow velocities. As a result, eddies form in the dead flow zones and there is a change in flow streamlines in the connected pores and fractures.

$$R_e = \frac{\rho Q}{\mu W} \tag{2.7}$$

The hydraulic relative roughness may also be used to determine the flow regime of seepage through a medium, as proposed by Lomize (1951) and Witkke (2014). This is achieved by calculating the quotient of the maximum roughness amplitude (k) of the fracture and the hydraulic diameter (D_h); where D_h is proportional to the ratio of the cross-sectional area (A), and the width (w) determining the wetted region of the fracture (P) (Witkke, 2014). When the flow regime is laminar and $k/D_h \leq 0.032$, the

streamlines are described as irrotational, and the fracture walls are hydraulically smooth (Figure 2-4). However, if $k/D_h > 0.032$, the streamlines diverge and at times rotate due to local rotation of water particles, and flow is known as rotational flow.

As aforementioned, transitioning from laminar to turbulent flow requires a critical Reynolds number, which in this case is $Re_c \geq 2300$ provided that ≤ 0.0168 $k/D_h \leq$ or $>$ 0.032 (Figure 2-5). Witkke (1990) has argued that the transition from laminar to turbulent flow will occur at high hydraulic gradients, or at small hydraulic gradients, with mean apertures of approximately 1 mm. Cornwell and Murphy (1985 cited in Aydin 2001) have suggested that the increase in the relative roughness of the fracture or well-mated fracture walls will have a transitional flow regime over a wider range and at lower Reynolds numbers.

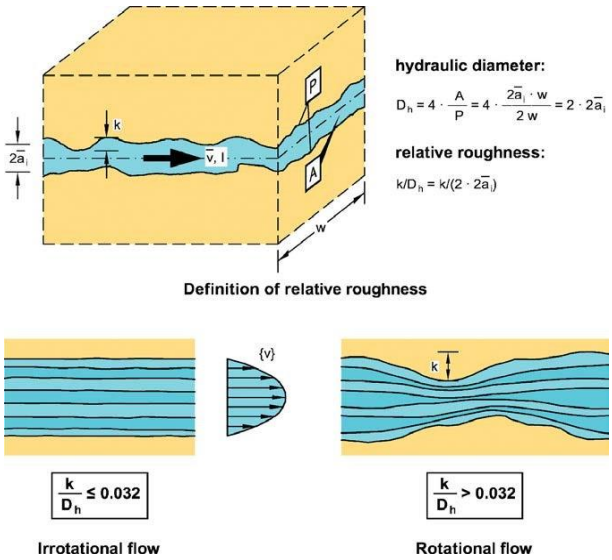

Figure 2-4: Types of laminar flow depending on the relative roughness (Witkke, 1990).

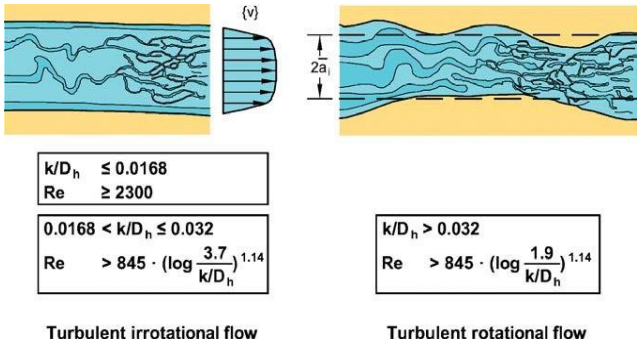

Figure 2-5: Types of turbulent flow depending on the relative roughness (Witkke, 1990).

2.5. Porosity

Fractured porous rocks often exhibit a double porosity system, where the water is either stored in the matrix (primary porosity) or transmitted through the fracture (secondary porosity) (Warren and Root, 1963). Primary porosity is inter-granular and develops with the formation of the rock, whereas secondary porosity occurs after the rock has formed, e.g. joints or faults. Nelson et al. (2001) highlight that primary porosity is not scale dependent, as compared to secondary porosity, which is (Equation 2.9-2.10).

$$\varphi = \left(\frac{V_p}{V_b}\right) \times 100 \tag{2.9}$$

$$\varphi_f = \left(\frac{e}{D+e}\right) \times 100 \tag{2.10}$$

Conceptual and numerical models are widely used to explain and predict fluid flow in double porosity systems. Barenblatt et al. (1960) have demonstrated that in a double porosity model, flow taking place in the rock matrix has a low permeability, and flow in fractures has a high permeability. Warren and Root (1963) expanded the Barenblatt et al. (1960) model and theory for fractured reservoirs. This model is based on the sugar cube configuration where the cubes store water and the fractures transmit water in the pseudo-state. Furthermore, the reservoir can either be matrix- or fracture-dominated. Bear (1988) also elaborated on the Representative Elementary Volume (REV) concept proposed by Barenblatt et al. (1960), namely that any small REV has several fractures and porous blocks, which interact as a double porosity medium (Figure 2-6). Furthermore, determining the REV including the microscopic and macroscopic heterogeneities will specify the materials hydraulic behaviour. Emphasising the heterogeneities of natural systems, the porosity may change depending on the chosen scale and volume of investigation. Bear (2007) has accentuated that in small-scale fracture studies, the porosity will either be one in the voids or zero in the matrix. As the volume under investigation increases, and both the voids and matrix are included, the porosity will change, and at some representative elementary length the porosity will be constant.

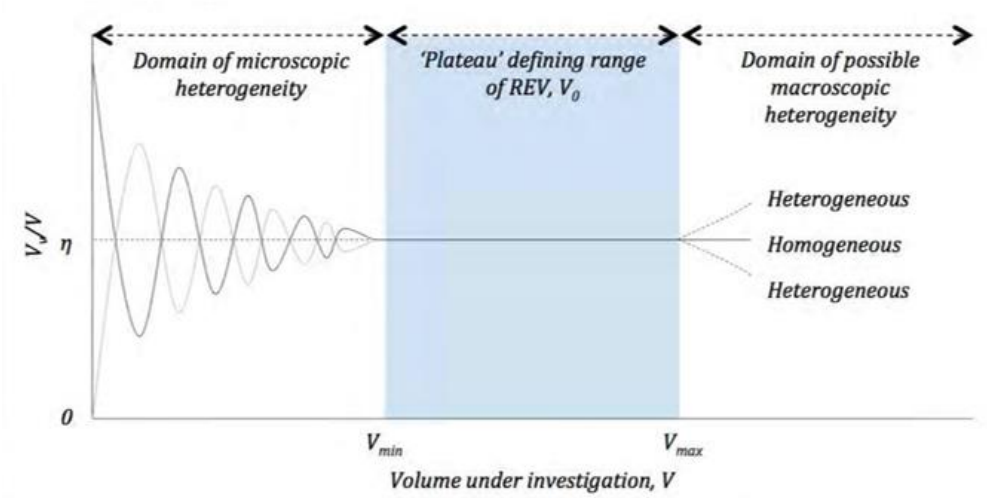

Figure 2-6: Representative elementary volume (REV) for fractures and porous block domains (Bear, 2007; Dippenaar et al., 2014).

The triple porosity model was proposed by Abdassah and Ershaghi (1986). This model is still used to predict flow when double porosity models fail to do so. This model is divided into three components, viz. matrix with low permeability, less permeable natural fractures, and highly permeable hydraulic fractures. The major limitation with double porosity models is that they assume that the matrix has uniform properties throughout the entire system. Lewis and Ghafouri (1997) and Bai et al. (1998) have modified double porosity models to include multiphase flow.

2.6. Geometric Characteristics

There are several geometric descriptors, namely, the type of structure, aperture, infill and surface roughness (ISRM, 1981; Bieniawski, 1989). Dippenaar and Van Rooy (2016) affirmed that fracture descriptors will likely influence the flow anisotropy in natural fractures. Mèheust and Schmittbuhl (2001) have suggested that the orientation of the hydraulic gradient can either inhibit or enhance flow in natural fractures, as opposed to the parallel plate model that has an identical hydraulic aperture. Contact obstacles or rough fracture walls may increase the tortuosity of flow paths or eddy effects thus governing the hydromechanical behaviour of fractures (Wang and Hudson, 2015; Slokkte, 2010).

2.6.1. Aperture

Many authors (e.g. Su et al., 1999; Qian et al., 2005; Wu et al., 2018) conceptualise natural rock fractures through the parallel plate model or transparent replicas of natural fractures. The purpose of these conceptual models is to understand and define elementary methods that govern fluid flow in fractured systems. The parallel plate model is an over-simplification of natural fractures, where smooth parallel plates are separated by a constant aperture e_h, referred to as the hydraulic aperture (Renshaw, 1995) (Figure 2-7a). Berkowitz (2002) noted that the Local Cubic Law is crucial in the parallel plate model because the flow rate is proportional to the aperture cubed (Equation 2.11). This author also noted that the hydraulic aperture may depend on variable aperture widths along different sections or from obstructed regions in the fracture (Figure 2-7b). Tzelepis et al. (2015) have suggested that the Local Cubic Law sometimes overestimates flow. It has been reported that, when determining the aperture, it should be measured as an average over a known length, as opposed to a point-by-point method (Oron and Berkowitz, 1998).

$$\frac{Q}{\Delta h} = C \cdot e^3 \qquad where \qquad C = \frac{w}{l_f} \cdot \frac{\rho g}{12\mu} \tag{2.11}$$

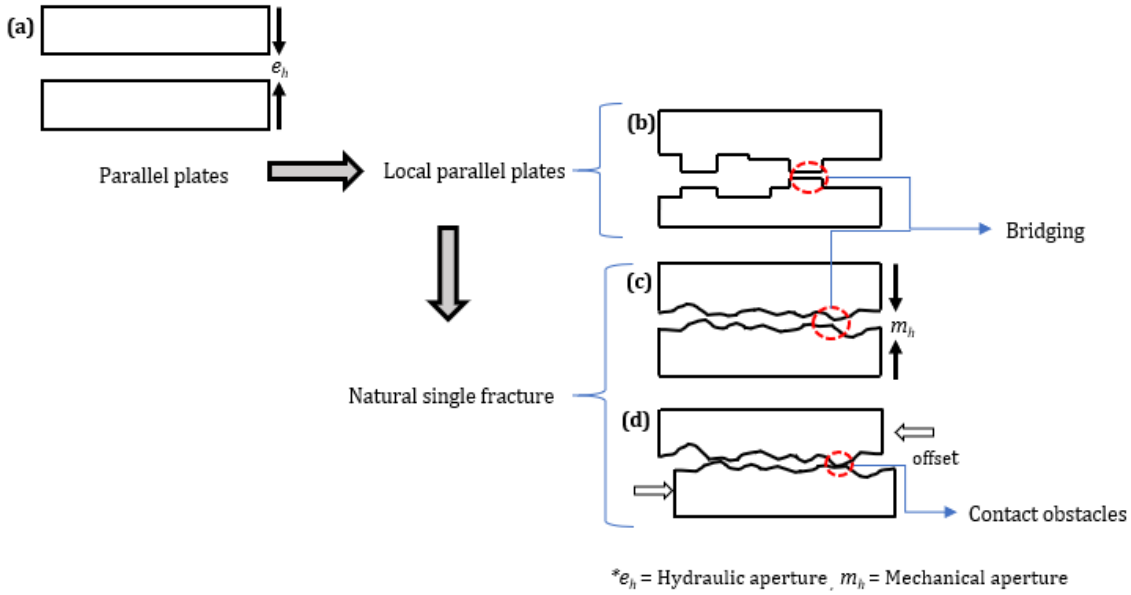

Figure 2-7: (a) Parallel plates separated by the hydraulic aperture, (b) local parallel plates with obstructing regions, (c) natural single fracture with a mechanical aperture, (d) Natural single mismatched fracture surfaces.

Barton et al. (1985) have noted that for a variety of rock types with smooth joints with large apertures, the mechanical aperture may be equal to the hydraulic aperture. Conversely, if the fracture surfaces are rough, then the mechanical aperture is seven times higher than the hydraulic aperture. Liu and Fan (2012) have demonstrated that the hydraulic aperture will also deviate from the mechanical aperture when fracture walls are mismatched. Segole et al. (2017) investigated the influence of variable aperture sizes using smooth parallel plates. The authors found that narrow apertures provide more contact between fluid and fracture walls, whereas in the wider apertures, there is less contact between the fluid and fracture walls. Jones et al. (2018b) conducted flow visualisation experiments to investigate the effects of contact obstacles on a rough-walled quartzite fracture, mismatched with a transparent replica wall. The results showed that contact obstacles obstruct flow in horizontal fractures and increase flow paths in vertical fractures. Despite the low flow rates, the flow paths were 4% and 14% longer than straight-line paths. Yeo (2001) asserted that bridging on fracture walls (Figure 2-7b-c) or fracture surfaces that are completely connected will act as contact obstacles and decrease the overall flow rate.

Hofmann et al. (2016) stated that natural rocks have variable aperture and mismatch of rough surfaces increases the aperture (Figure 2-7d). Xia et al. (2017) emphasise that the contact obstacles will change when the fracture walls are displaced in a certain direction, while Witherspoon et al. (1980) confirm that the contact areas in natural rock fractures can withstand stresses while maintaining space for seepage as the aperture decreases. Hoek and Bray (1977) relate Witherspoon et al.'s (1980) finding to the hydraulic conductivity of the aperture, that is , as the fracture aperture decreases, so does the hydraulic conductivity (Figure 2-8). Furthermore, minor displacements as small as 0.5mm of one fracture wall can change the hydraulic conductivity by five orders of magnitude (Durham and Bonner, 1994; Berkowitz, 2002).

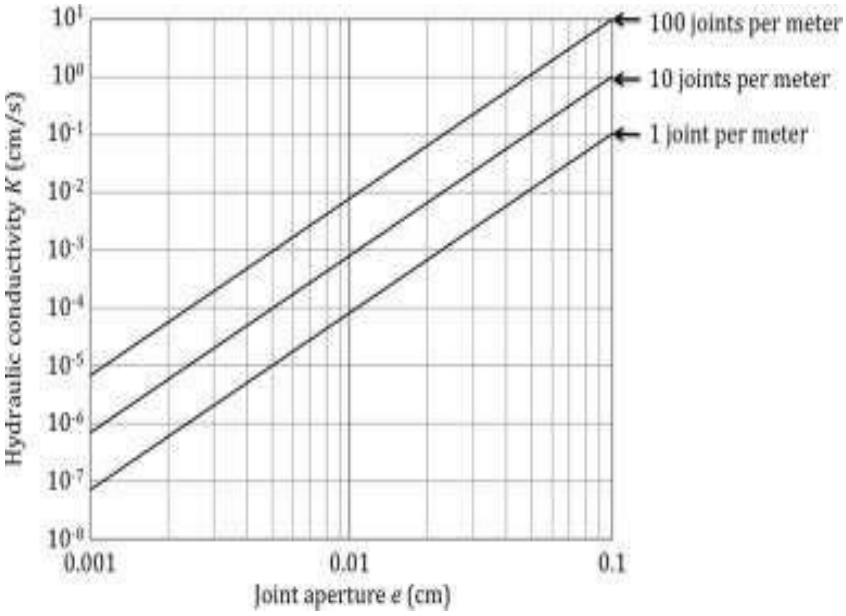

Figure 2-8: Influence of joint aperture e and spacing on hydraulic conductivity K parallel to a set of smooth parallel joints (Hoek and Bray, 1977).

2.6.2. Roughness

Roughness is defined as the surface distribution of small-scale asperities and large-scale waviness on the fracture walls (Dippenaar and Van Rooy, 2016). The joint roughness coefficient (hereafter JRC) values were first introduced by Barton (1973) to determine the mechanical properties of rock joints. Barton and Choubey (1977) then added ten standard roughness profiles that correspond with the JRC values, ranging from zero to 20, for planar and very rough surfaces (Figure 2-9). Luo et al. (2016) stated that surfaces of rock fractures may vary due to gouge materials filling the fracture voids or geomechanical processes.

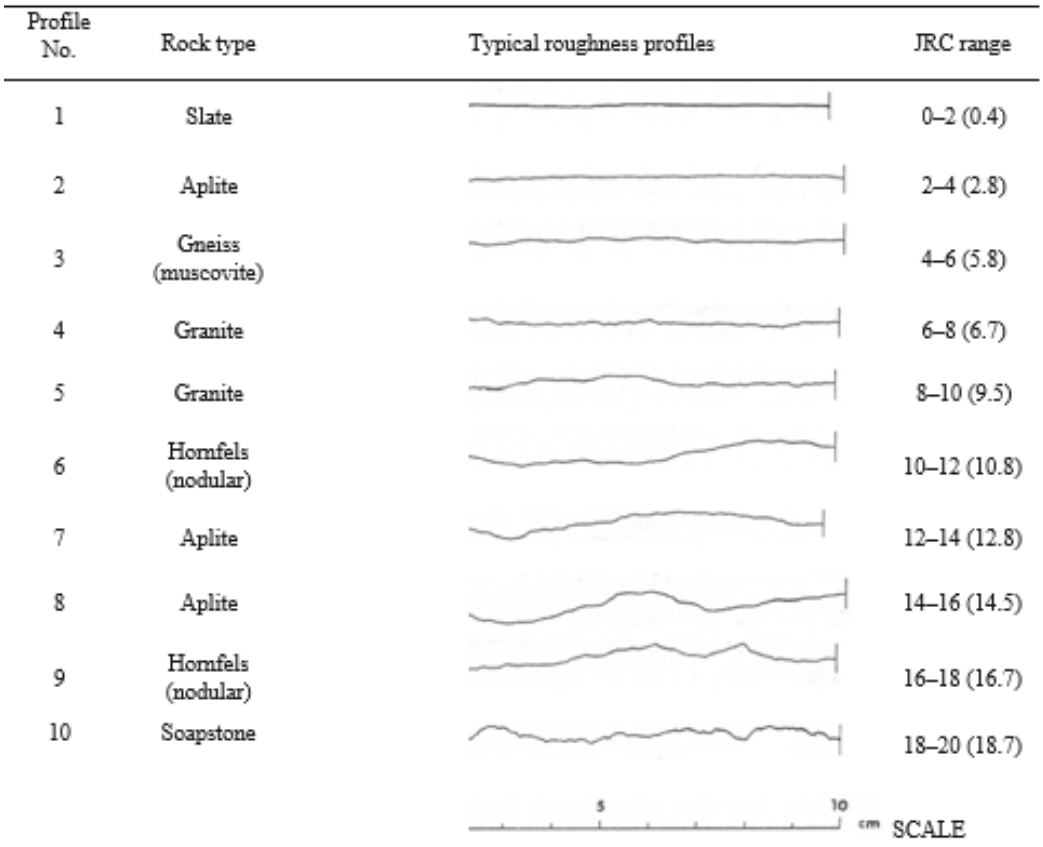

Figure 2-9: Standard roughness profiles for estimating joint roughness coefficient (Barton and Choubey, 1977; Jang et al., 2014).

Yong et al. (2017) have identified that visually comparing the roughness of samples using a profile gauge tool over 10 cm measuring lengths does not yield accurate results. Bandis et al. (1981) quantified laboratory micro-roughness using an empirical equation (Equation 2.12) that includes JRC values obtained from the standard roughness profiles by Barton and Choubey (1977). Barton (1982 cited in Barton and De Quadros 1997) proposed another technique to determine the JRC, which includes the average maximum amplitude (a) along several representative profiles over a measured length (L) (Equation 2.13).

$$JRC = JRC_0 \left(\frac{l}{l_0}\right)^{-0.02JRC_0} \tag{2.12}$$

At 100 mm scale:

$$JRC = 400\frac{a}{L} \tag{2.13}$$

2.7. Natural Rock Fracture Flow: Laboratory Experiments

Ranjith and Darlington (2007) conducted laboratory experiments to analyse nonlinear single-phase flow in real rock joints. In this experiment, water flows through a single granite fracture. The applicability of the Forchheimer and Reynolds numbers were evaluated under increasing confining pressures. A positive quadratic relationship exists between pressure change against Reynolds number and a negative quadratic relation between the apparent transmissivity against the Reynolds number. In the latter relationship, there was a divergence from linearity at Reynolds numbers of 10 and transmissivity (T/T_0) of 0.9. Furthermore, as the water inflow increased, it washed out some of the infill material, and a weak to strong inertia existed when the Reynolds number reached 10; this was also identified by other authors, including Durham and Bonner (1994), and Sketjne et al. (1999). At low confining pressures, the Forchheimer equation (Equation 2.14) was applicable and at higher confining pressures of >3Mpa, the validity decreased. As the confining pressures increase, there is an increased closure of the aperture because of compressible air, and consequently flow becomes more torturous in the fracture.

$$-\nabla P = AQ + BQ^2 \tag{2.14}$$

Where A is the linear coefficient relating to the properties of the fluid and B non-linear coefficient relating to the geometries of the medium (Dippenaar and Van Rooy, 2016).

Singh et al. (2015) conducted fluid flow experiments on cylindrical samples of granite, similar to Ranjith and Darlington (2007). The authors investigated the response of confining pressures, fracture roughness, and extreme base pressures. The variation of the fracture surfaces was evaluated statistically. This includes the roughness average, which is the mean asperities height calculated over the fracture surface, and the root mean square roughness, which represents the depth of the fracture surface and asperities height. The coarse-grained granite sample reached high roughness average (R_a) values, and root mean square roughness (R_{rms}) values, showing a rough fracture surface with large asperities and a large aperture. In addition to this, the coarse sample had high discharge rates, which resulted in high Reynolds numbers. However, the fine-grained granite sample had less roughness average (R_a) values and root mean square roughness (R_{rms}) values, showing a smooth fracture and a less tortuous path. The Reynolds numbers for the fine-grained sample reflected the transition from laminar to

turbulent flow. This study showed that flow behaviour is affected by geometrical characteristics of samples, elevated base pressure, and confining pressure.

Cherubini et al. (2012) conducted several hydraulic tests of water passing various paths through fractured limestone block, with artificial fractures made with 5 kg mallet blows. This study aimed to determine the relationship between the flow rate and the hydraulic gradient for each fracture-controlled flow path. A linear relationship exists between the Forchheimer and Reynolds number i.e., as the Forchheimer number increases, so does the Reynolds number; and inertial effects are greater than viscous forces at higher Reynolds numbers. A polynomial relationship also exists between the change in hydraulic head and the discharge under steady-state conditions; given that discharge increases as the hydraulic head increases.

Yin et al. (2018) conducted a series of hydromechanical experiments for deformable rough-walled fractures from various lithologies. The aperture decreased as the confining pressure increased, and the Reynolds numbers indicated an increasing trend with confining pressures. In addition to this, when the joint roughness coefficients (JRC) values increased, the aperture and Reynolds numbers decreased. In addition to this, flow was channelled and became more tortuous because of rougher fracture surfaces.

Laboratory-scale investigations of unsaturated natural rock fracture flow are limited or mainly focus on the deformability of fractured surfaces and sample sizes while evaluating other parameters such as linearity.

Chapter 3 Materials and Methods

3.1. Physical Experiments

3.1.1. Sample and Model preparation

Rock samples were obtained from the Pretoria Group of the Transvaal Supergroup, and the Nylstroom Subgroup of the Waterberg Group, South Africa. The latter lithostratigraphy is related to the quartzite sample of the Swaershoek Formation, and the preceding lithostratigraphy is related to the shale sample of the Timeball Hill Formation (Johnson et al., 2009; 1: 250 000 2428 Nylstroom; 1: 250 000 2528 Pretoria). A 6 mm diameter hole is drilled to a 1 mm depth into the fracture, creating a point source (mimicking the method by Nicholl and Glass, 2005) for the water inlet pipe. Both rocks fulfil the specifications of a dominant, persistent single fracture on all sides of the samples (Figure 3-1):

(a) Shale is sawed to dimensions of 200×155×55 mm.

(b) Quartzite is sawed to dimensions 225×200×110 mm.

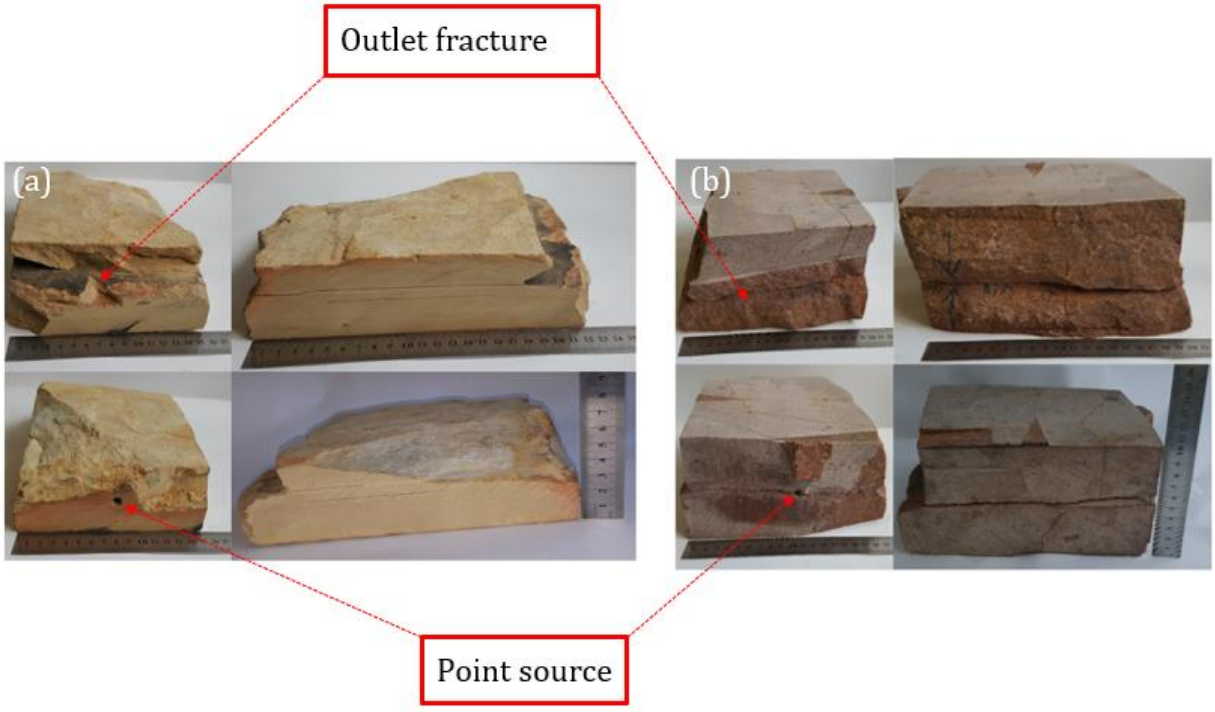

Figure 3-1: Sample preparation of (a) shale and (b) quartzite showing the point source and outlet fracture surface.

Two L-stands are designed and built with the following specifications (per stand):

- Acrylic Perspex ® sheet-1 (397×291×100 mm)
- Hardboard plywood sheet (385×250×150 mm)
- Acrylic Perspex ® sheet-2 covered with a non-absorbent rubber mat (291×198×120 mm)
- Engineering butt hinge loose pin (225 mm)
- 8 Head flat screws (0.5×20 mm)
- 4 Steel rods (100 × 250 mm).

Acrylic sheet-1 is joined to a hardboard plywood via an engineering butt hinge, and head flat screws, forming an L-shaped stand. Acrylic sheet-2 using Angle meter™ is orientated at 23 ˚and 60˚ respectively, and both angles are marked off on acrylic sheet-1. Thereafter, two equally spaced holes are drilled for each inclination (i.e. 23˚and 60˚) on acrylic sheet-1. Four steel rods are then inserted into the drilled holes. As a result, acrylic sheet-2 is able to form 23 ˚and 60˚ fixed inclinations when resting on the L-stand (Figure 3-2a, b). Acrylic sheet-2 is then placed on top of acrylic sheet-1 for the horizontal (0˚) inclination (Figure 3-2c). For vertical (90˚) inclination, acrylic sheet-2 is then moved and placed against the hardboard plywood with the addition of a G-clamp during experiments to prevent movement of the rock sample in this orientation (Figure 3-2d).

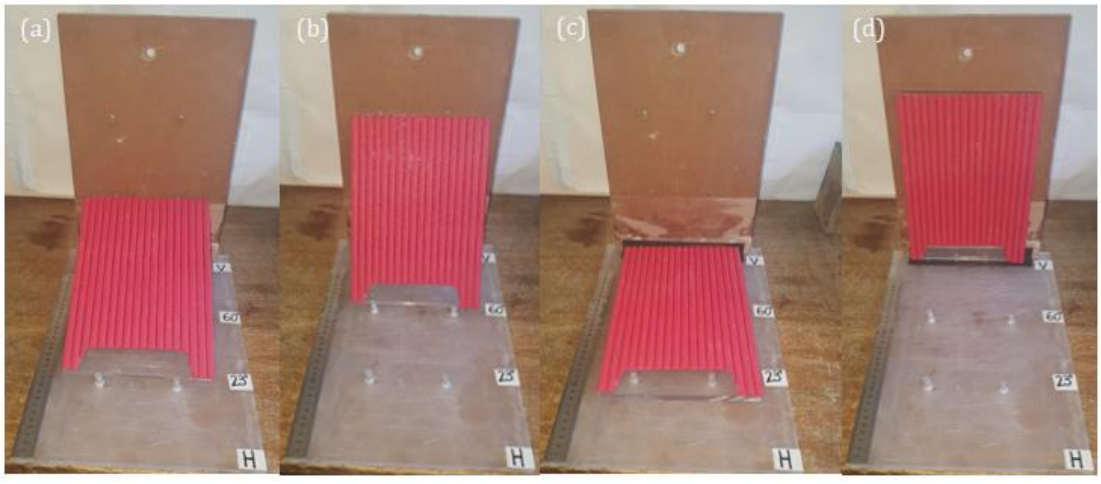

Figure 3-2: L-stand with acrylic sheet-1 inclined at (a) 23˚ (b) 60˚ (c) 0˚ (d) 90˚.

The design of the L-stands follows the specifications of a strong supporting structure for the samples and prevents unwanted detachment of the inlet pipes during testing. The acrylic sheets are used as the base and supporting structure of the rocks, because

acrylic sheets do not absorb water, and thus, will not affect the discharge readings. In addition to this, the non-absorbent rubber mat prevents the rock samples from sliding on acrylic sheet-2 during testing.

3.1.2. Flow experiments

L-stands are placed on top of a table with 454×320 mm lids placed beneath each stand. The lid captures water that drains freely from the fracture. A third of the lid with a 20 mm hole overlaps the table edge and allows water to directly flow into the outflow catchment placed beneath it. The rock samples are then inclined depending on the angle of investigation (Figure 3-3).

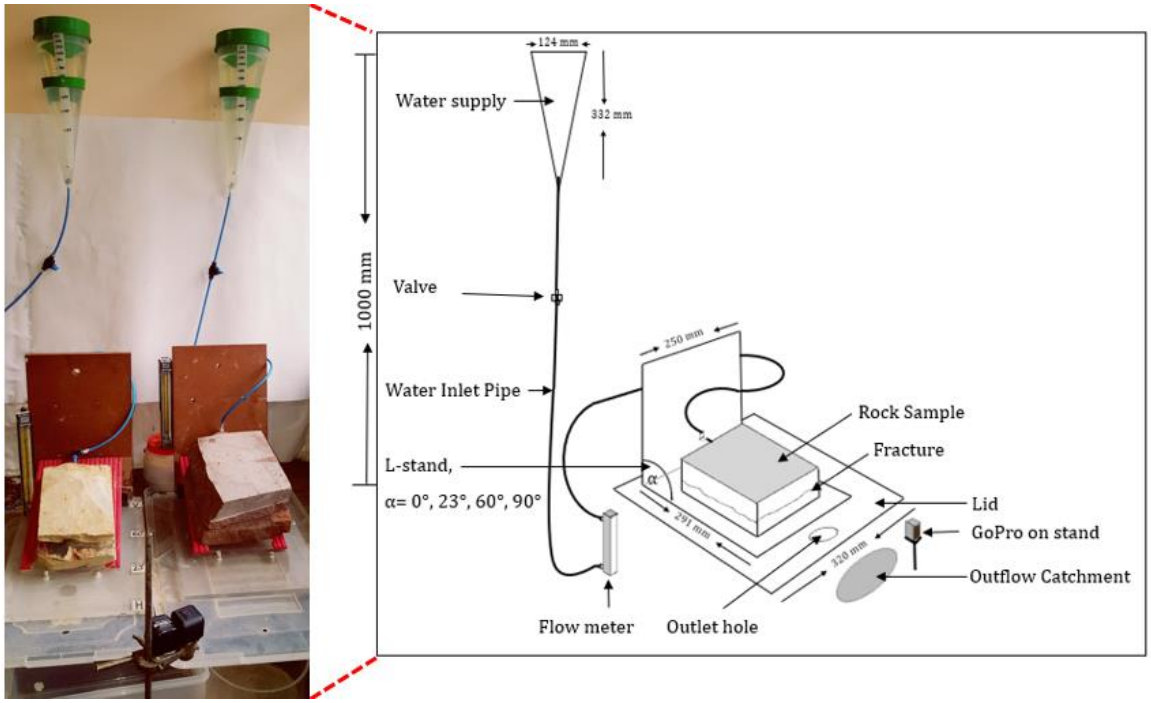

Figure 3-3: Experimental set-up

Water supplies are then installed at an elevation head of 1 meter above the base of the L-stand. An inlet pipe (6 mm) with an open/close valve is connected to the water supply and feeds water via flow meters to the point source. The inlet pipe is then covered with plumbers' tape. To prevent leakage, the inlet pipe is also sealed off with pan seal ring after insertion into the point source and the flow meter tubes. The volume of water moving through the pipe is constant along the entire length. Therefore, the placement of the flow meters on top of the table and the position of the valve will produce the same discharge readings (Mathews, 2010).

Two cameras (GoPro™) record a live video of each test for visual observations.

3.1.3. Experimental Procedure

The conceptual model is tested under continuous influx conditions with four tests conducted per inclination (Figure 3-4). The falling head test was conducted from initially dry conditions for all tests. In each test, there were three distinct phases, namely, the initially dry, wet, and rewetting phase (building on the experimental work of Nicholl et al. (1993) and Nicholl and Glass (2007). Water supply is topped up after drainage in the initially dry phase to commence to the wet, followed by the rewetting phase. A total of 16 tests with flow meters of low discharge rates of 20 ml/min were conducted for each sample. Another 16 tests were conducted for each sample with flow meters of high discharge rates, that is, 200 ml/min for shale and 500 ml/min for quartzite.

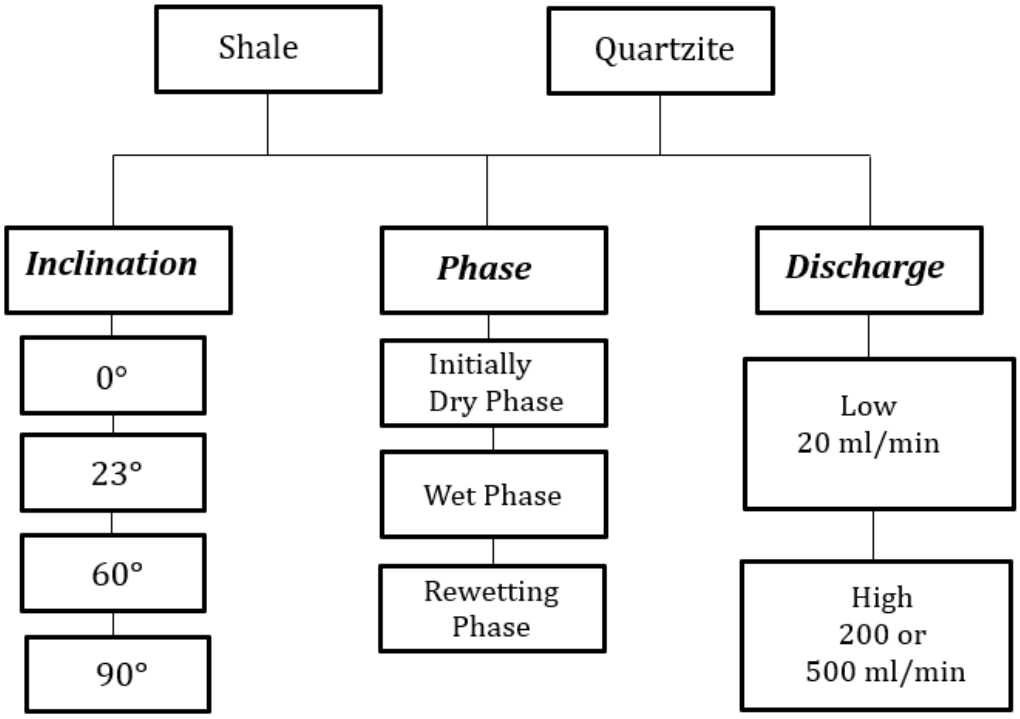

Figure 3-4: Variables in the experimental procedure

At the beginning of each test, the water supply is filled up to a maximum of 1300 ml volume of water and the valve is opened for water inflow into each sample. The falling head test measures the amount of water that flows through the fracture length over a constant increment head difference from the initial elevation h_1, which is measured at time t = zero and the final head difference measured at h_2 at time $t = t$ (Figure 3-5). Every 10 mm head decrease is recorded with the respective time and the flow meter

reading. The flow meter readings aid in calculating the volume of water in the fracture at a certain hydraulic head, the average linear velocities thereof, and eventually the Reynolds numbers.

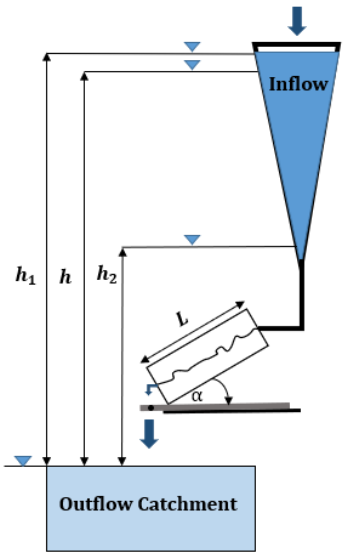

Figure 3-5: Falling head permeability test for natural rock fractures adapted from Knappett and Craig (2012).

After draining the total volume of water in the water supply, the valve is closed. The water in the outflow bucket is then measured and recorded with the total running time of the test. At the end of the test (i.e. initially dry, wet and rewetting phase), the samples are disconnected from the inlet pipe and are oven-dried over a period of 18 hours at 105 °C. Samples are then cooled and cycles of testing repeat.

3.2. Data Acquisition

3.2.1. X-ray diffraction (XRD)

Rock samples were submitted for X-Ray diffraction to determine mineralogical content of the different rock specimens used in the experiments. Results are incorporated to estimate porosity and to better interpret possible rock mineralogy on interstitial porosity.

The samples are prepared according to the standardised panalytical backloading system, which provides nearly random distribution of the particles. Samples are analysed using a Panalytical Aeris powder diffractometer in θ–θ configuration with a PIXCel detector, fixed divergence, and fixed receiving slits, with Fe filtered Co-Kα radiation (λ=1.789Å). The relative phase amounts (weight %) are identified using X'Pert

Highscore Plus software and estimated using the Rietveld method X'Pert high score plus software.

3.2.2. Porosity

The quantitative mineralogical composition through X-ray diffraction is used to determine the porosity *n* of each sample (e.g. Dippenaar et al. 2014; Equation 3.1). This technique includes the distribution of minerals with varying density. The dry bulk density (ρ_B) of the sample is equal to the dry mass of the sample (M_{dry}) divided by the volume change (Equation 3.2). The volume change is the difference between the volume of water present in the bucket (V_{bucket}) and the volume of water when the sample is submerged (V_{sub}). The average solid density ρ_s is equal to the sum of the fractions of minerals (f_M) present that add up to one (1), multiplied by the densities of the individual minerals (ρ_M) (Equation 3.3) (Deer et al.,1996).

$$n = 1 - \frac{\rho_B}{\rho_s} \tag{3.1}$$

Where

$$\rho_B = \frac{M_{dry}}{V_{sub} - V_{bucket}} \tag{3.2}$$

$$\rho_s = \sum f_M \times \rho_M \tag{3.3}$$

3.2.3. Hydraulic conductivity

The hydraulic conductivity (K) is determined through laboratory-scale methods. In the falling head test, the hydraulic conductivity is a function of the cross-sectional area of the water supply inlet (a) and rock sample (A), length of the specimen (L), and the head difference between h_1 and h_2 at time = t. The hydraulic conductivity is determined through equation 3.4 (Fitts 2002; Das, 2008).

$$Q = K \cdot \frac{h}{L} \cdot A = -a \cdot \frac{dh}{dt} \tag{3.4}$$

$$\int_0^t dt = \int_{h1}^{h2} \frac{a \cdot L}{A \cdot K}$$

$$K = \frac{a}{A} \cdot \frac{L}{(t_1 - t_0)} \ln\left(\frac{h_1}{h_2}\right) = 2.303 \cdot \frac{a \cdot L}{A \cdot dt} \log\left(\frac{h_1}{h_2}\right)$$

Where

$$a = \pi r\ (r + \sqrt{h^2 + r^2});\ A = L \times B$$

3.2.4. Moisture content

Rock samples are weighed on an OHAUS Valor™ 1000 compact precision scale (max. 30 kg) before and after the falling head tests. The laboratory determination of moisture content is determined from standard test methods as expressed in equation 3.5 (ISRM, 1981).

$$\theta = \left[\frac{(M_{cms} - M_{cds})}{(M_{cds} - M_c)}\right] \times 100 = \frac{M_w}{M_s} \times 100 \qquad (3.5)$$

3.2.5. Aperture and roughness

Following testing, the shale and quartzite are sawn to identical smaller dimensions of 100×100 mm (Figure 3-6). The aperture of each sample is determined using a Zeiss Stereo Discovery V20 Microscope. The Zeiss Axiocam colour camera projects the sample onto the screen and captures images thereof (Figure 3-7). The magnitude of the aperture is determined by extending the focus to ×4.7 magnification, and measuring the distance between the two fracture walls on each side using the Zeiss Zen Software. The relative roughness is determined using the ratio of the quotient of maximum roughness amplitude area and average aperture of fracture to describe the flow regimes (refer to section 2.4).

Figure 3-6: Shale and quartzite samples sawn to dimensions of 100mm × 100mm.

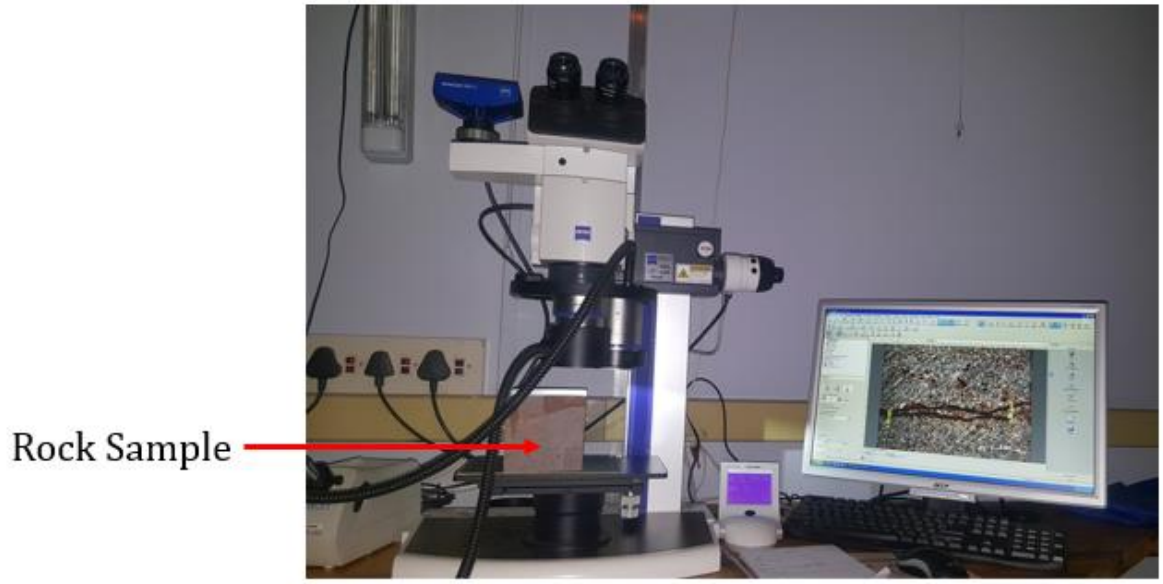

Figure 3-7: Zeiss Stereo Discovery V20 Microscope housed in the Microscopy and Microanalysis Laboratory, University of Pretoria.

Joint roughness was quantified using the methods of Bandis et al. (1981) and Barton (1982), as described in section 2.6.2. The surface roughness of the fracture is measured with a joint roughness comb. The various profiles obtained from the roughness comb are compared and classified with the Barton and Choubey (1977) chart.

Chapter 4 Results: Visual Observations

The visual observations of flow behaviour in a single persistent fracture from the falling head test are presented here. Results are discussed separately for each rock type, at the hand of the appropriate figures. All rock specimens are orientated at 0˚, 23˚, 60˚ and 90˚. In all figures, the inlet pipe (i.e. point source) is on the left-hand side of each snapshot, unless stated otherwise. Bulleted lists (e.g. a-h) correspond to those used in the relevant figures and numbering of mechanism (e.g. Fluid finger 1, 2, 3) is from left to right for all samples.

4.1. Shale

4.1.1. Horizontal (0 °) inclination

Initially Dry Phase (Figure 4-1a-h):

a-b) Water is introduced into the inlet fracture through the point source. Upon wetting, water advances longitudinally along the fracture, parallel to the flow direction. Thereafter, a fluid finger (1) exits the fracture laterally and migrates vertically downwards.

c) Longitudinal progression of water along the fracture results in another fluid finger (2) laterally exiting the fracture at a different channel point. This finger forms a flow path adjacent to the previous flow path (finger 1).

d) A fluid finger-tip (3) exits the fracture after two seconds (time-interval) at a separate channel point, forming a full finger flow path.

e-f) The formation of the finger flow paths discontinue, and water gradually flows along the fracture advancing towards the right side.

g-h) The wetting front along the fracture widens, indicated by the double-sided arrow. In addition to this, water gradually wets the outlet surface on the left-side while the right-side remains dry. The observed flow pattern remains the same until the end of the test at 528 seconds.

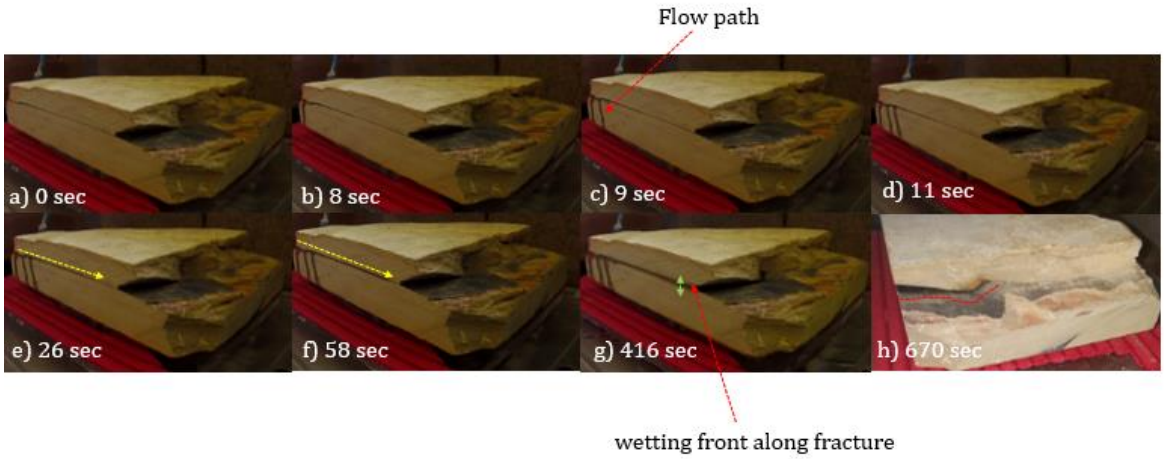

Figure 4-1: (a-h) Flow pattern in shale for the initially dry phase at the horizontal (0°).

Wet and Rewetting Phase (Figure 4-2A-H):

A-B) Water is reintroduced into the inlet fracture through the point source. Upon wetting, three fluid fingers exit the fracture at individual channel points. The sequence (i.e. 2 and 3, 1) is different as compared to the initially dry phase (Figure 4-1d).

C) A finger-tip (4) laterally exits the channel point, migrates vertically downwards and remains static halfway through its flow path for 81 seconds.

D) More water rewets the flow path and the finger-tip (4) gains enough fluid mass to move farther downwards; longitudinal flow along the fracture advances. The observed flow pattern remains the same until the end of the test at 467 seconds.

E-F) Water is reintroduced into the inlet fracture through the point source. Three fluid fingers exit the fracture sequentially (i.e. 2, 1, and 3) at separate channel points. In addition to this, longitudinal flow along the fracture progresses.

G) Another fluid finger-tip (4) migrates vertically downwards and ceases movement halfway through its flow path.

H) The finger-tip (4) overcomes static behaviour as it reaches a critical water mass size and resumes movement in the vertical direction. The observed flow pattern remains the same until the end of the test at 513 seconds.

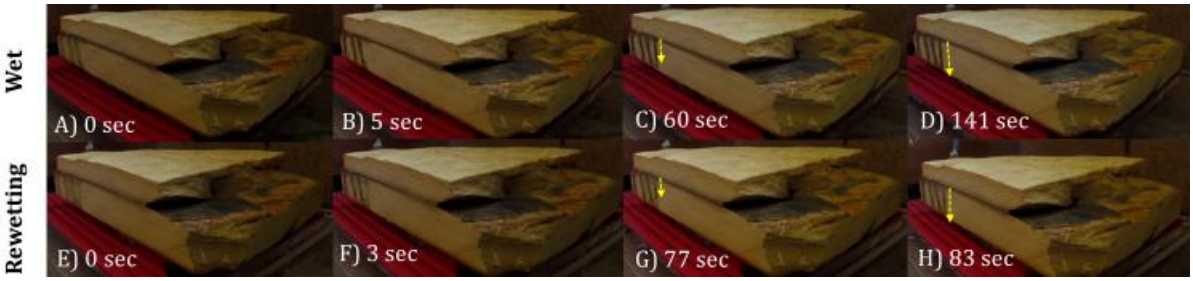

Figure 4-2: (A-H) Flow pattern in shale for the wet and rewetting phase at the horizontal (0°).

4.1.2. 23 °inclination

Initially Dry Phase (Figure 4-3a-f):

a-b) Water is introduced into the inlet fracture through the point source. Upon wetting, two fluid fingers (1,2) simultaneously exit the fracture at different channel points and gravitate vertically downwards.

c) Preferential flow prevails along the fracture as a thin and a wide longitudinal wetting front advance in the same direction.

d-e) The wide wetting front progresses gradually along the fracture. This wetting front then migrates vertically downwards on the fracture wall as a fluid finger-tip (3) and remains static halfway through its flow path.

f) Finger-tip (3) migration resumes after 16 seconds and forms a flow path. This flow pattern remains the same until the end of the test at 5605 seconds.

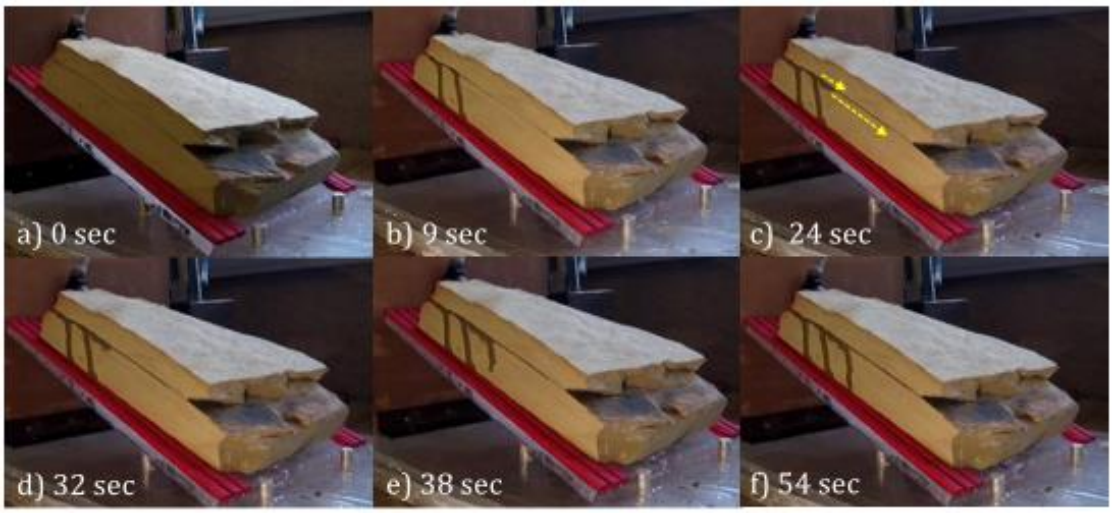

Figure 4-3: (a-f) Flow pattern in shale for the initially dry phase inclined at 23°.

Wet and Rewetting Phase (Figure 4-4A-H):

A-B) Water is reintroduced into the inlet fracture through the point source. Upon wetting, two fluid fingers (1,2) simultaneously exit the fracture and rewet the initial flow paths from the initially dry phase. In addition to this, a fluid finger-tip (3) exits the fracture at the same channel point as the second fluid finger. This finger-tip (3) then progresses longitudinally along the fracture.

C) The finger-tip (3) discontinues longitudinal movement along the fracture and gravitates vertically downwards. Due to insufficient water mass, the finger-tip (3) migrates slowly in this direction.

D) Water continues to rewet the longitudinal wetting front along the fracture and the current finger flow paths. The observed flow pattern remains the same until the end of the test at 81780 seconds.

E-F) In the rewetting phase, water is reintroduced into the inlet fracture through the point source. Two fluid fingers (1,2) instantaneously exit the fracture and gravitate vertically downwards. A third fluid finger-tip (3) progresses 22 seconds later and creates a full finger flow path. The longitudinal wetting front along the fracture increasingly widens.

G) Continuous finger-tips exit the outlet fracture, and move as a compact body wetting the surface. The wetting only occurs on the left side of the outlet surface while the right side remains dry.

H) Infiltration of water into the shale fracture is slow. Consequently, water imbibes into the matrix and the sample is completely wet. The rock remains wet, with no visible wetting front or flow paths until the end of the test at 88200 seconds.

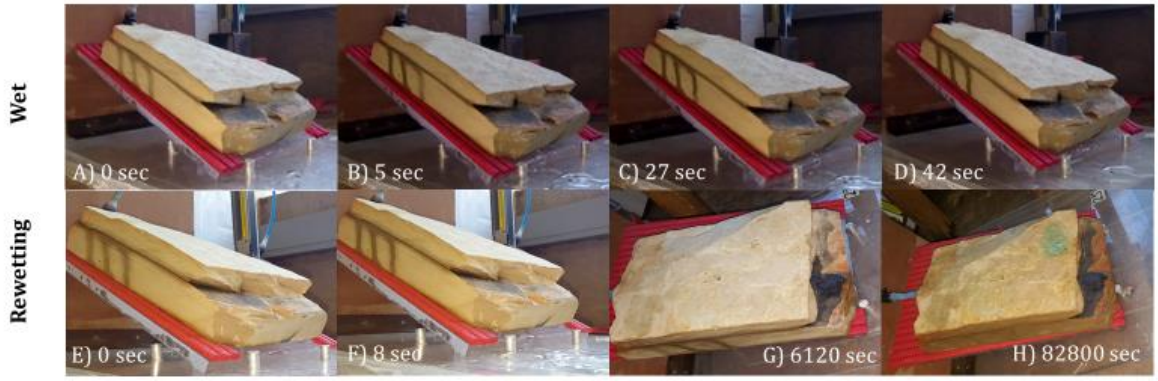

Figure 4-4: (A-H) Flow pattern in shale for the wet and rewetting phase inclined at 23°.

Due to the duration of the previous test and matrix imbibition, the experiment is repeated for all phases.

Initially Dry, Wet and Rewetting Phase (Figure 4-5a-h):

a-b) Water is introduced into the inlet fracture through the point source. Upon wetting, two fluid fingers (1, 2) exit the fracture concurrently at separate channel points and gravitate vertically downwards. Another fluid finger (3) exits the fracture 12 seconds later (time-interval) adjacent to the previous finger flow paths (1, 2). Longitudinal flow along the fracture continues, and a coherent body of fluid remains static at the third channel point.

c) The coherent body of fluid advances as a fluid finger-tip (4) migrating downwards at an angle, forming a flow path that is dissimilar to prior flow paths.

d) Water rewets the previous flow path that has slightly dried out, subsequently, the finger-tip (4) travels farther. The wetting front at the outlet fracture slowly progresses from the left to the right side. The observed flow pattern remains the same until the end of the test at 1187 seconds.

e-f) Water is reintroduced into the inlet fracture through the point source for the wet phase. Upon wetting, three fluid fingers exit the fracture at a different sequence (i.e. 2 and 3, 1) as compared to the initially dry phase. Moreover, a fluid finger-tip (4) exits the fracture and stalls halfway through its flow path.

g) The finger-tip (4) resumes movement after 176 seconds (time-interval) and gravitates vertically downwards. Water spreads from the left towards the right side at the outlet surface and a single fluid finger (5) progresses forward.

h) The fluid finger (5) progresses farther downwards at the outlet fracture. This flow pattern remains the same until the end of the test at 948 seconds.

In the rewetting phase, only three fingers exit the fracture in the sequence 1 and 2, and 4; sequence based on the parent flow paths of the initially dry phase. The test for this phase runs for 872 seconds, and the observed flow paths are similar to those of the wet phase.

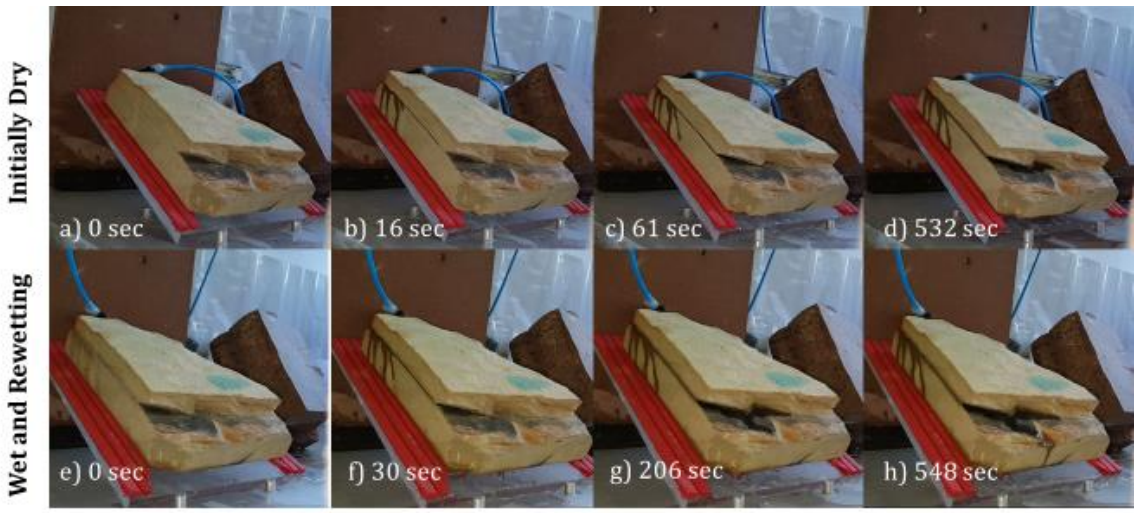

Figure 4-5: Flow pattern in shale for the (a-d) initially dry phase, (e-f) wet and rewetting phase inclined at 23°.

4.1.3. 60° inclination

Note: the inlet pipe (i.e. point source) is at the top of each snapshot.

Initially Dry Phase (Figure 4-6a-f):

a-b) Water is introduced into the inlet fracture through the point source. Upon wetting, water migrates from a channel point at the left edge of the inlet fracture and migrates downwards as a fluid finger (1). However, halfway through its flow path the finger (1) deviates and flows below the fracture.

c) Another fluid finger (2) exits the inlet fracture the same way as previously described for the first finger (1). This flow path crosses the first finger flow path

and flows along the edge of the sample. The incessant flow of water on the current flow paths results in a wider wetting front.

d-e) A single fluid finger (3) exits the middle of the outlet fracture and gravitates downwards. Multiple finger-tips at the outlet surface rewet the initial flow path created by the fluid finger (3). Thereafter, the finger-tips stall at the local depression region at the edge of the outlet surface.

f) The continuous flow of water increases fluid mass. Consequently, the finger-tips move as a compact body and advance farther. The wetting front at the outlet surface advances to the right side and the wetting front along the fracture widens. This flow pattern remains the same until the end of the test at 829 seconds.

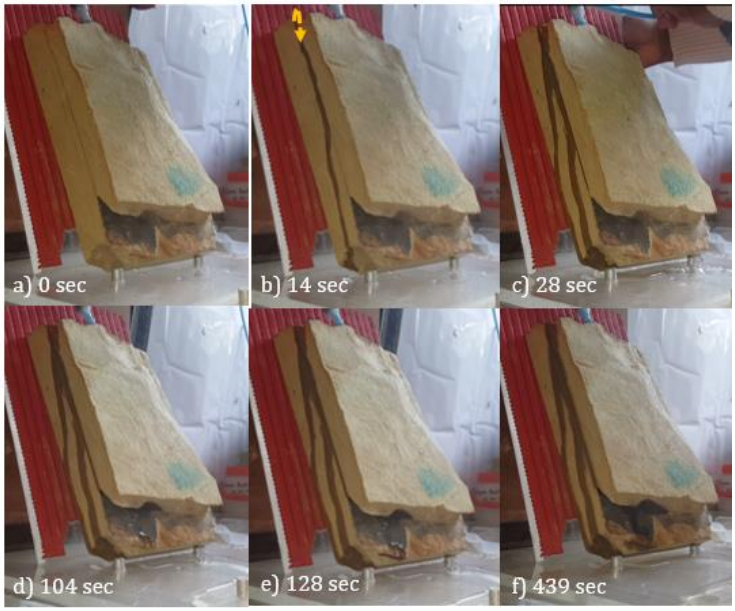

Figure 4-6: (a-f) Flow pattern in shale for the initially dry phase inclined at 60°.

Wet and Rewetting Phase (Figure 4-7A-I):

A-B) Water is reintroduced into the inlet fracture through the point source. As water exits a channel point at the left edge of the inlet fracture; the fluid gravitates vertically downwards and two fluid fingers sequentially (i.e. 1, 2) form flow paths as the initially dry phase.

C-D) The first flow path (fluid finger 1) slightly dries out and another finger-tip from the inlet fracture migrates vertically downwards and rewets it.

E) The fluid finger (1) flow path slightly dries out again, and another finger-tip rewets it. In addition to this, a fluid finger (3) fully spans the outlet surface.

F) Alternating cycles of wet and dry flow paths are clear as the finger-tip advances and rewets the first flow path (fluid finger 1) again. The continuous flow of water from the middle of the outlet surface results in finger-tip clusters at the local depression region. This flow pattern remains the same until the end of the test at 809 seconds.

G-H) In the rewetting phase, water is reintroduced into the inlet fracture through the point source. Upon wetting, fluid fingers rapidly exit the middle of the outlet fracture and spread towards the left side. A fluid finger (1) flows along the fracture and the continuous flow of water results in a wider flow path.

I) Infiltration of water into the inlet fracture is slow, and water no longer exits the sample. The observed flow pattern remains the same until the end of the test at 837 seconds.

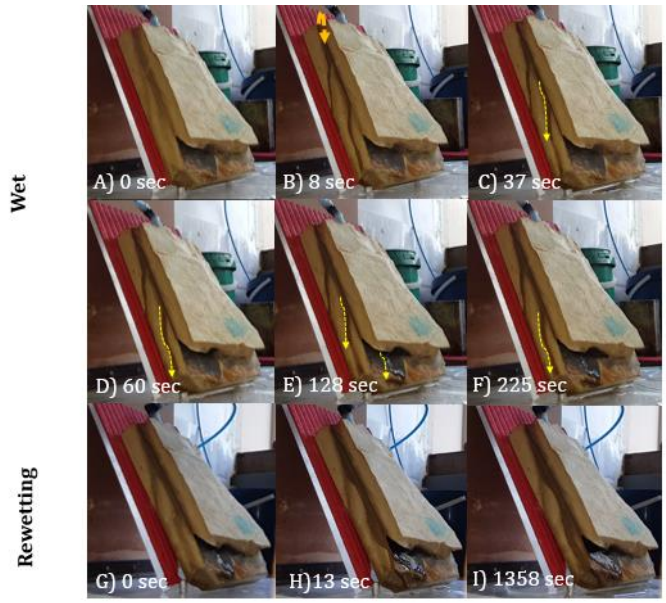

Figure 4-7: (A-I) Flow pattern in shale for the wet and rewetting phase inclined at 60°.

4.1.4. Vertical (90°) inclination

Note: the inlet pipe (i.e. point source) is at the top of each snapshot.

Initially Dry Phase (Figure 4-8a-d):

a-b) Water is introduced into the inlet fracture through the point source. Upon wetting, water migrates from the left edge of the inlet fracture and progresses vertically downwards as a fluid finger (1) along the fracture.

c) The second fluid finger (2) exits the inlet fracture at a different channel point and this flow path merges with the first flow path. When the fluid finger (2) reaches the end point of the fracture, it deviates from its merged flow path and a thin fluid film spatters onto the acrylic sheet-1 (see arrow), and the rest of the water wets the outlet surface.

d) Spattering of the thin fluid film onto the acrylic sheet-1 halts and fingering prevails at the outlet surface. This flow pattern remains the same until the end of the test at 814 seconds.

Figure 4-8: (a-d) Flow pattern in shale for the initially dry phase inclined at 90°.

Wet and Rewetting Phase (Figure 4-9A-D):

A-B) Water is reintroduced into the inlet fracture through the point source. Upon wetting, two fluid fingers (1,2) exit the fracture as previously described for the initially dry phase, but no thin fluid film splats onto the acrylic sheet-1. The wetting front at the outlet surface spreads towards the right side.

C-D) The wetting front at the outlet surface spreads even farther towards the right side. The flow pattern described remains the same until the end of the test at 715 seconds.

In the rewetting phase, water rewets the previous flow pattern (i.e. flow paths and wetting front, Figure 4-9D) and this flow pattern does not change over time. This test runs for 745 seconds.

Figure 4-9: (A-D) Flow pattern in shale for the wet and rewetting phase inclined at 90°.

4.2. Quartzite

4.2.1. Horizontal (0 °) inclination

Initially Dry Phase (Figure 4-10a-h):

a-b) Water enters the inlet fracture through the point source. Upon wetting, a thin fluid film (1) exits laterally on the far left of the fracture migrating vertically downwards. Longitudinal flow of water along the fracture progresses and a coherent body of fluid stalls at a different channel point.

c) The fluid stalls until there is enough water mass and migrates vertically downwards as a fluid film (2).

d-e) Water preferentially flows along the two initial flow paths, and their width thickens. A coherent body of fluid stalls at another channel point with a visible wetting front.

f) 10 seconds later, the thin fluid film (3) gains enough water mass and exits the channel point migrating vertically downwards.

g) A fluid film (4) exits the channel point and forms a flow path prior to the previous fluid path (3). Water preferentially flows along the fracture, as a result, the wetting front widens. Water partially spreads from the left to the right side of the outlet fracture and a thin fluid film (5) forms a flow path.

h) More water rewets the current flow paths and the wetting front along the fracture widens and advances to the right side of the outlet fracture surface. The observed flow pattern remains the same until the end of the test at 360 seconds.

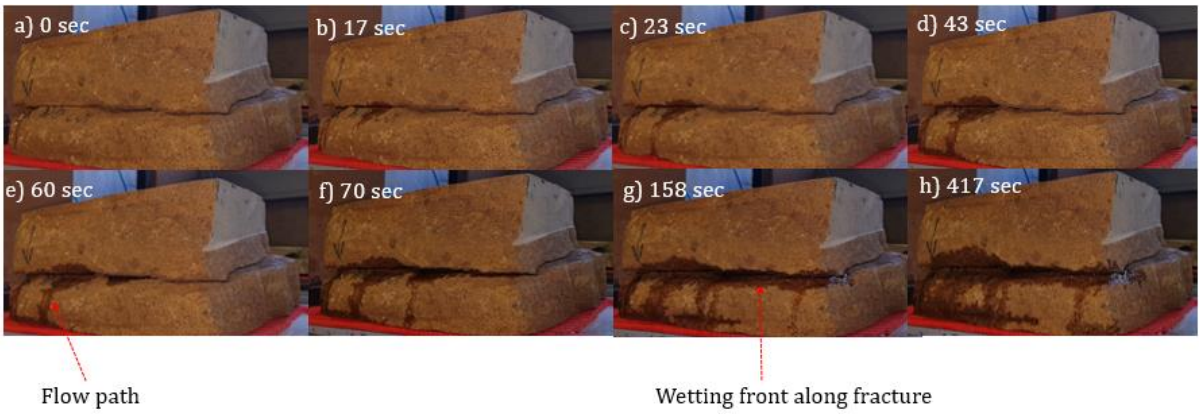

Figure 4-10: (a-h) Flow pattern in quartzite for the initially dry phase at the horizontal (0°).

Wet and Rewetting Phase (Figure 4-11A-F):

A-B) Water re-enters the inlet fracture through the point source. Water rewets the initial flow paths for the initially dry phase (Figure 4-10h). Sixty seconds later, a fluid film (6) exits the outlet fracture at a channel point and downward migration of this fluid film is slow.

C) As more water exits the fracture, the flow path of the previous fluid films (i.e. 5, 6) widen, and the wetting front at the outlet fracture advances. The flow of observed pattern remains the same until the end of the test at 364 seconds.

D-E) In the rewetting phase, water re-enters the inlet fracture through the point source, and rewets the initial flow paths of the previous phases. A fluid film (7) exits the channel point and forms a flow path prior to the fourth fluid film (4). The flow paths continue to widen as indicated by the double-sided arrow.

F) As more water rewets the fracture, the initial flow paths merge. The observed flow pattern remains the same until the end of the test 396 seconds.

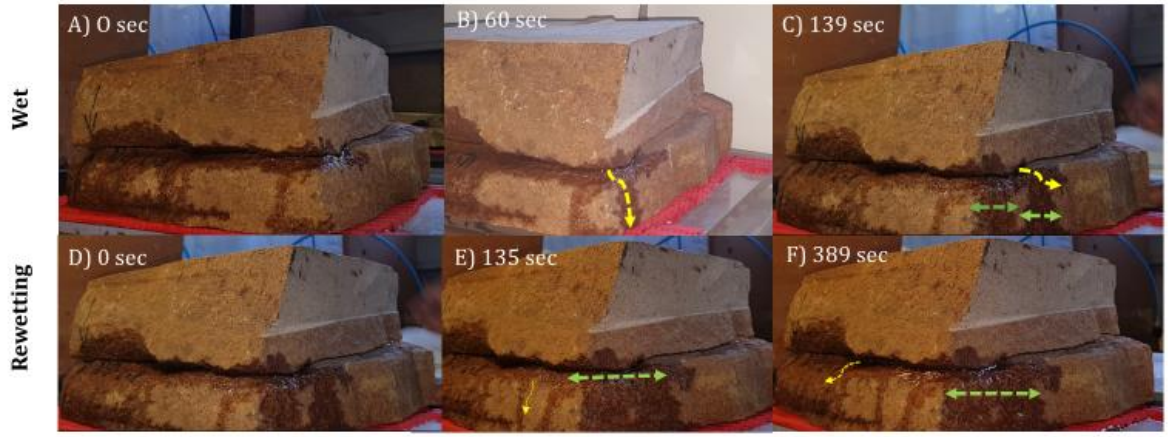

Figure 4-11: (A-F) Flow pattern in quartzite for the wet and rewetting phase at the horizontal (0°).

4.2.2. 23° inclination

Initially Dry Phase (Figure 4-12a-h):

a-b) Water enters the inlet fracture through the point source. Upon wetting, a fluid film (1) exits from the middle of the outlet fracture and migrates downwards.

c) As more water wets the middle of the outlet surface, the wetting front advances towards the left side. Subsequently, a pool of fluid stalls at the local depression region.

d) A second later, a fluid film (2) longitudinally exits from this local depression, and the fluid immediately gravitates vertically downwards. The wetting front on the outlet fracture surface progresses laterally to the left side.

e) A thin fluid film (3) migrates vertically downwards adjacent to the previous flow path (fluid film 2).

f) Air bubbles are observed as more water flows out of the local depression region.

g) A thick film of water exits the local depression region and splits into thin fluid films, rewetting the current flow paths. Additionally, the wetting front on the outlet surface advances farther towards the left side and progresses longitudinally along the fracture.

h) The flow paths and wetting front along the fracture continue to widen. The observed flow pattern remains the same until the end of the test at 421 seconds.

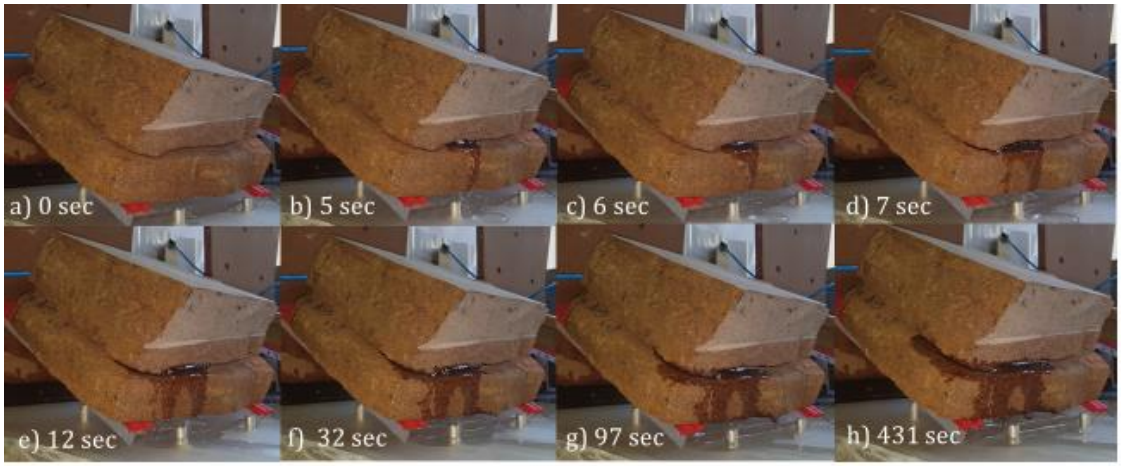

Figure 4-12: (a-h) Flow pattern in quartzite for the initially dry phase inclined at 23°.

Wet and Rewetting Phase (Figure 4-13A-H):

A-B) Water re-enters the inlet fracture through the point source. Upon wetting, water exits from the middle of the outlet fracture and rewets the initial flow paths (Figure 4-12h). The wetting front progresses to the right side of the outlet surface, and a fluid film (4) longitudinally exits the channel point and migrates vertically downwards.

C-D) As more water rewets the current flow paths, a fluid film (5) forms a new flow path adjacent to the previous film (4). The observed flow pattern remains the same until the end of the test at 432 seconds.

E-F) In the rewetting phase, water re-enters the inlet fracture through the point source. A thick fluid film longitudinally exits the outlet fracture. Subsequently, the thick film splits into thin films that vertically flow downwards and rewet the flow paths for the initially dry and wet phase.

G) More water rewets the current flow paths and air bubbles are observed at the outlet fracture surface.

H) Thick fluid films continue to exit from the outlet surface and split into thinner films. The observed flow pattern remains the same until the end of the test at 386 seconds.

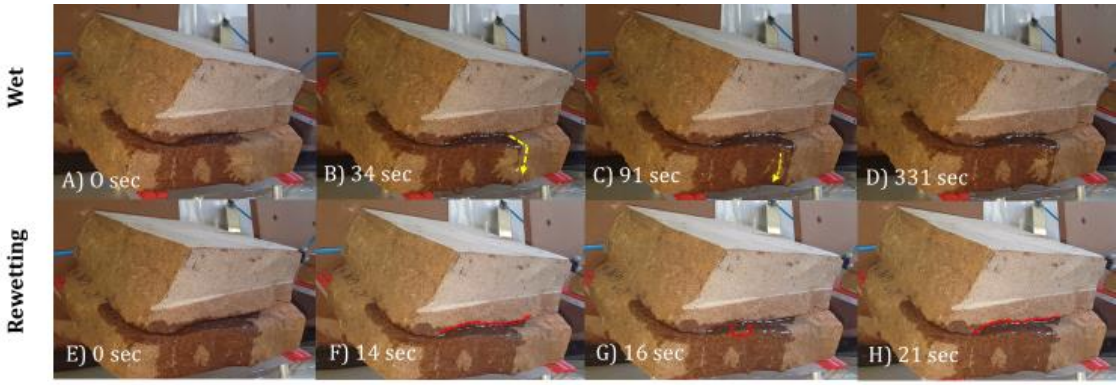

Figure 4-13: Flow pattern in quartzite for the (A-D) wet and (E-H) rewetting phase inclined at 23°.

4.2.3. 60 ° inclination

Note: the inlet pipe (i.e. point source) is at the top of each snapshot.

Initially Dry Phase (Figure 4-14a-h):

a-b) Water enters the inlet fracture through the point source. Upon wetting, a fluid film (1) exits the channel point from the middle of the outlet fracture and gravitates vertically downwards.

c-d) A second fluid film (2) exits the channel point adjacent to the previous flow path. Three seconds later, another fluid film (3) forms a flow path between the first and second flow path.

e) Another fluid film (4) longitudinally exits the outlet fracture at a different channel point.

f) Water continues to rewet the current flow paths, consequently, another fluid film (5) exits the fracture adjacent to the previous flow path (4).

g-h) As more water rewets the preferential flow paths, the wetting front on the outlet surface progresses from the middle to the left side while the right side remains dry. The observed flow pattern remains the same until the end of the test at 483 seconds.

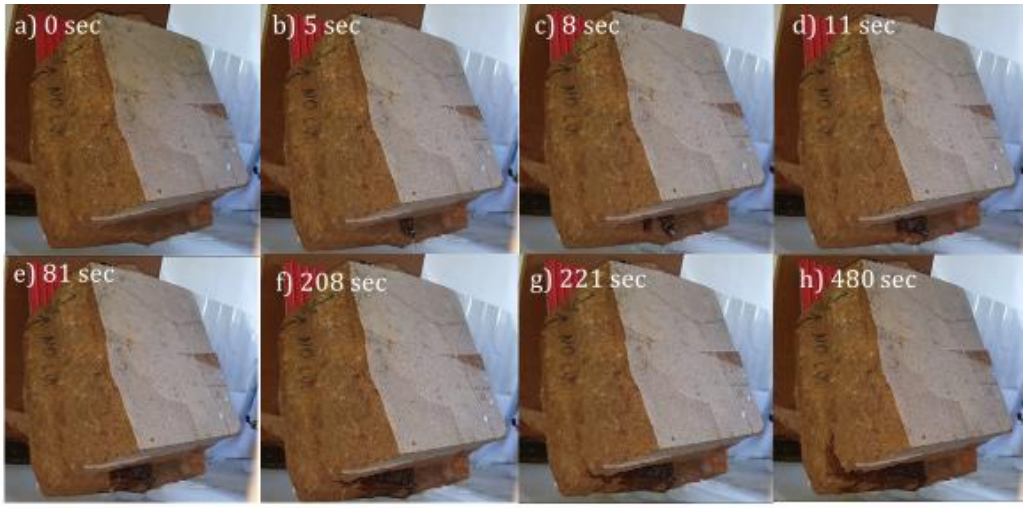

Figure 4-14: (a-h) Flow pattern in quartzite for the initially dry phase inclined at 60°.

Wet and Rewetting Phase (Figure 4-15A-D):

A-B) Water re-enters the inlet fracture through the point source. Upon wetting, thin films of water exit the outlet surface simultaneously, merging into a thick film, and rewetting the flow paths of the initially dry phase. There is continuous flow of water at the outlet fracture, even so, the flow pattern remains the same until the end of the test at 448 seconds.

C-D) In the rewetting phase, water re-enters the point source. Two fluid films (1,2) exit their respective channel points, that is, in the middle and at the left corner of the outlet fracture. The wetting front along the outlet fracture advances towards the right side. The observed flow pattern remains the same until the end of the test at 480 seconds.

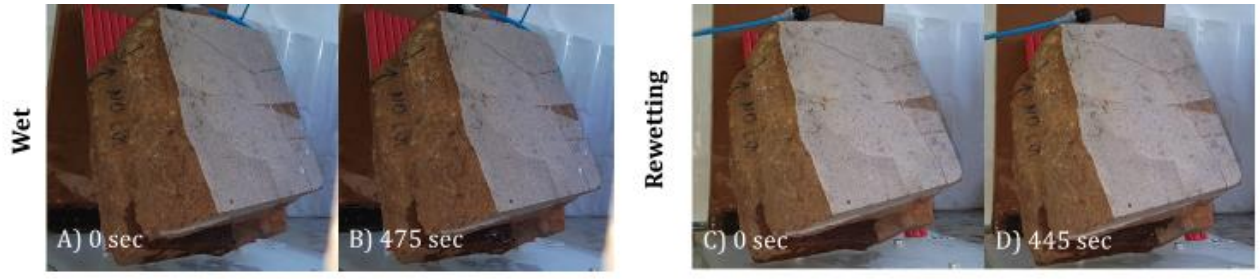

Figure 4-15: Flow pattern in quartzite for the (A-B) wet and (C-D) rewetting phase inclined at 60°.

4.2.4. Vertical (90°) inclination

Note: the inlet pipe (i.e. point source) is at the top of each snapshot.

Initially Dry Phase (Figure 4-16a-d):

a-b) Water enters the inlet fracture through a point source. Upon wetting, a single fluid film (1) exits the middle of the fracture outlet and migrates vertically downwards.

c) More water spreads on the outlet surface, as a result, the flow path of the previous fluid finger (1) widens.

d) Another fluid film (2) exits the outlet fracture at a separate channel point. This flow pattern remains the same until the end of the test at 437 seconds.

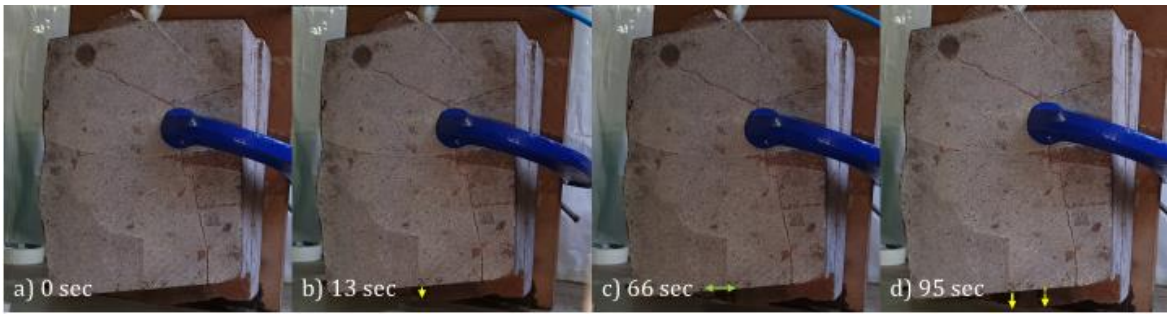

Figure 4-16: (a-d) Flow patterns in quartzite for the initially dry phase inclined at 90°.

Wet and Rewetting Phase:

In both phases, the observed flow paths are similar to the initially dry phase. Water continues to spread only on the left side of the outlet surface, while the right side remains dry. Each test runs for 435 seconds for the wet and 443 seconds for the rewetting phase.

4.3. Summary

Falling head permeability tests are performed with flow meters of low and high discharge rates. The observed flow patterns have similar results for both samples at all orientations. Therefore, the presented data is scaled down by providing snapshots from tests with low flow meter discharge rates for each rock specimen at various angles of inclination. Different flow mechanisms occur as the water exits the fracture, that is, finger flow in the shale and film flow in quartzite. At 23° inclination, infiltration into the

shale sample is slow, as water is being stored in the interstitial porosity; as all the water in the water supply imbibes into the matrix block, the sample becomes wet. The test is then repeated for the same angle of inclination and fracture flow prevails with minimal infiltration into the shale matrix. Preferential flow predominates in both samples for all the other tests where there is lateral migration of fluids exiting at certain channel points forming flow paths. Contrarily, there is also longitudinal migration of fluids along the fracture, resulting in wetting fronts with variable widths.

Chapter 5 Results: Quantitative Data

This chapter analyses the quantitative data acquired from the falling head permeability tests. This includes the change in hydraulic head, cumulative volume changes, and the average linear velocities of flow through natural rock fractures. Comparison of flow meter readings at low and high discharge rates as water enters and exits the fracture, water losses and the total running time for these tests are discussed. The calculated unsaturated hydraulic conductivities of the samples are also evaluated, relating the hydraulic conductivity to the change in moisture content.

5.1. Hydraulic Head, Volume and Average Velocity

In the falling head permeability test, the hydraulic head decreases as water passes through a fracture over a certain time interval. The data is presented graphically with two data sets representing each angle of inclination (i.e. 0˚, 23˚, 60˚, and 90˚). The initially dry, wet, and rewetting phase correspond with the visual observations in Chapter 4, and in this section the dry phase is synonymous with the initially dry phase.

A total volume of 1300 ml of water seeps through the fracture of each rock specimen. An inverse linear relationship exists between the hydraulic head and the cumulative volume, that is, as the hydraulic head decreases the cumulative volume of water captured in the outflow catchment increases. The linear regression line of all the graphs have, as expected, very high coefficients of determination (denoted R^2) in the range of 0.9939 to 0.9993 for shale, and 0.9916 to 0.999 for quartzite. As per Figure 5-1 and Figure 5-2, both tests and phases consistently yield similar results. The cumulative volumes for the all the phases are in the ranges of 998-1190 ml for shale and 1079-1116 ml for quartzite, with water loss percentages of 8.46-23.2% (shale) and 14.15-17% (quartzite) respectively.

Note: To decrease the margin of error, the zero point is when the test was stopped, thus removed from the data sets. Dots represent experimental values and solid lines, represent fitting of experimental values.

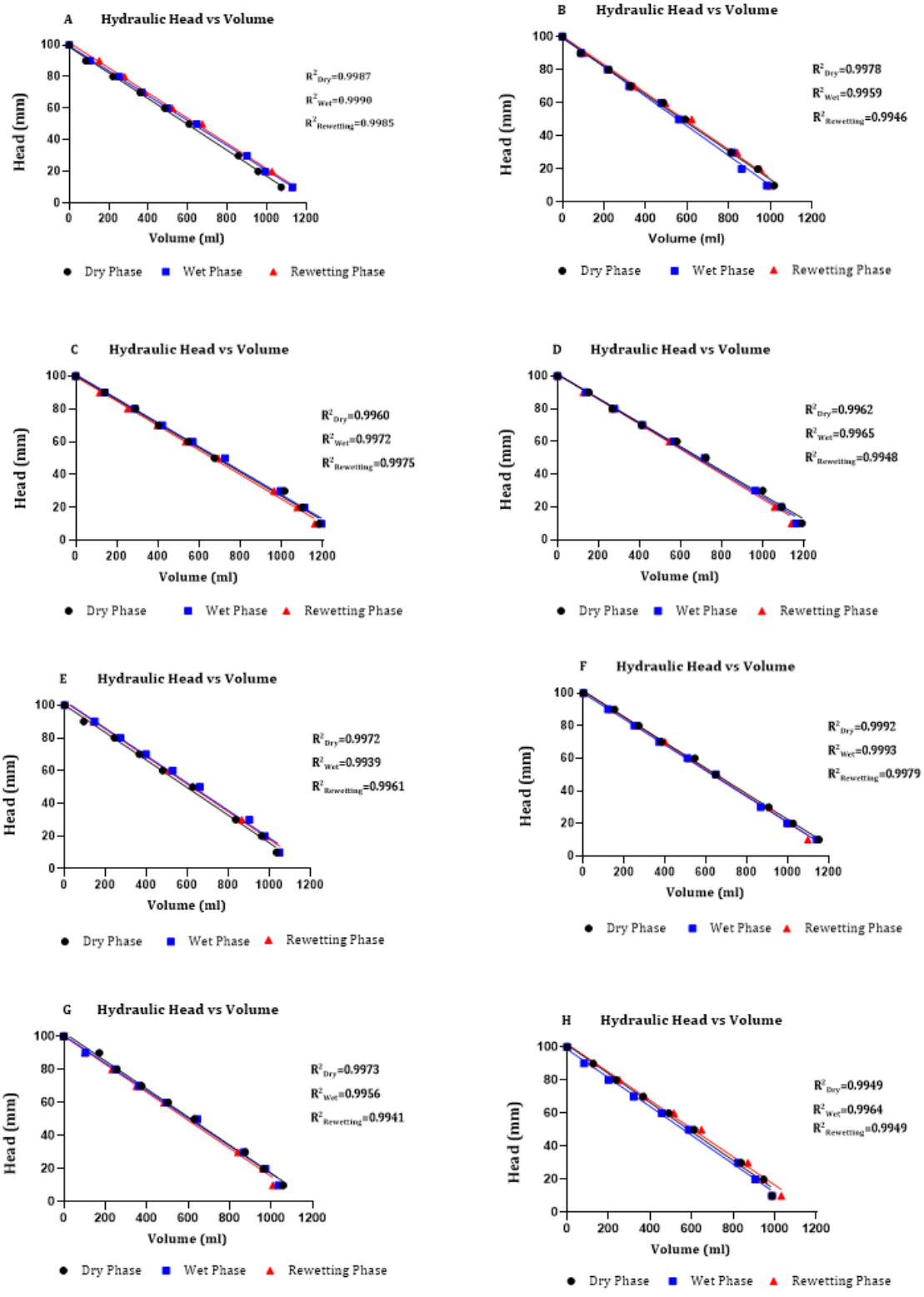

Figure 5-1: Hydraulic head versus cumulative volume graphs for shale, inclined at (A-B) 0˚(horizontal); (C-D) 23˚; (E-F) 60˚; (G-H) the vertical (90˚).

To decrease the margin of error, the zero point is when the test was stopped, thus removed from the data set. Dots represent experimental values and solid lines, represent fitting of experimental values.

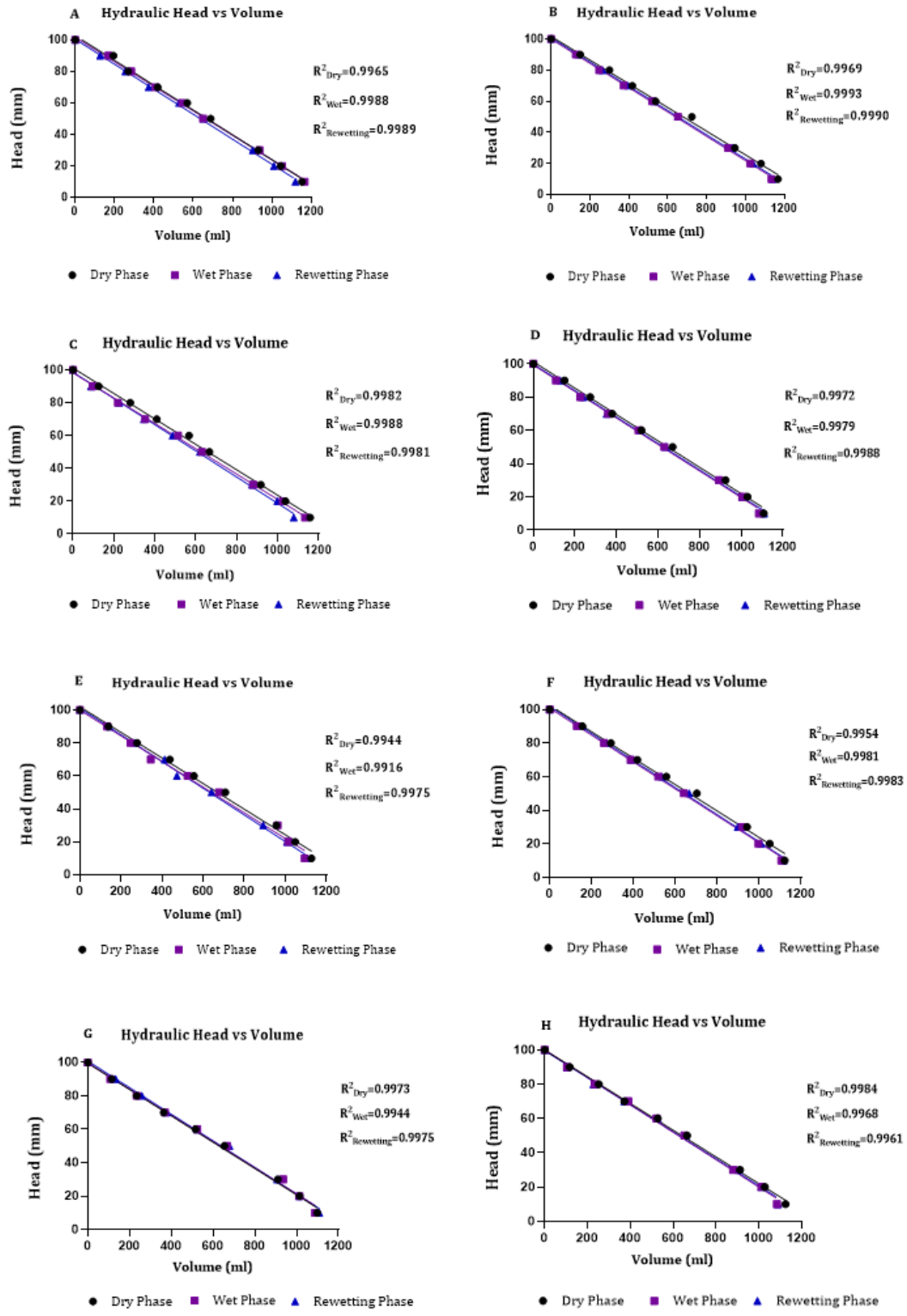

Figure 5-2: Hydraulic head versus cumulative volume graphs for quartzite, inclined at (A-B) 0˚ (horizontal), (C-D) at 23˚, (E-F) 60˚, (G-H) Test 29 and 30 at the vertical (90˚).

Flow meter readings at low discharge rates have average linear velocities of 0.003 m/s for both samples at various inclinations. However, the average linear velocity is also equal to the maximum low flow meter discharge rate. As a result, the true average linear velocities of seepage through the fractures are regarded as those derived from the high discharge flow meter data. In this data, the discharge rates for both samples are not equal to the maximum discharge rate detectable by the flow meter.

There is little variation in the average linear velocity results, despite angle of inclination in each of the samples (Table 5-1). As the hydraulic head drops, the average linear velocity gradually decreases and, in some instances, the change in hydraulic head does not influence the average linear velocity. For example, at a hydraulic head drop of 90 mm to 80 mm, the average velocity remains at 0.021 m/s in the shale sample (Appendix B). This supports Darcy's Law, which states that the flow rate is a function of the hydraulic conductivity and hydraulic gradient, which are both constant parameters independent of the orientation (dip angle) of the fracture. The overall calculated average linear flow velocities in the quartzite fracture are higher than in the shale fracture.

Table 5-1: Average linear velocity results obtained from high flow meter readings.

Inclination	Average Linear Velocity, q (m/s)	
	Shale	Quartzite
Horizontal (0˚)	0.02-0.01	0.07-0.06
23˚	0.03-0.02	0.07- 0.05
60 ˚	0.02	0.06-0.05
Vertical (90˚)	0.02- 0.01	0.06-0.05

*Raw data for Tabular results and all average velocities are given in Appendix C.

5.2. Discharge and Time

The graphical representation of low and high flow meter discharge rates of shale and quartzite are evaluated at different inclinations. This includes all the data acquired for both samples. A linear relationship exists between inflow or outflow volume and time for all orientations in both samples (Figure 5-3 to Figure 5-6), except when shale is inclined at 23˚ for low flow meter discharge rates.

At low flow meter discharge rate tests (Figure 5-3A-D), water drains faster from the shale fracture yielding the highest discharge rates and shortest running time for the test at 0˚ orientation. Visual observations have shown that infiltration of water into the shale sample at 23˚ is slow as water gets stored into the interstitial porosity of the matrix. This also relates to the recorded discharge rates that decrease over time, and at approximately time = 90000 seconds, no water flows out of the fracture therefore the outflow discharge is zero (Figure 5-3B). Thereafter, the discharge rates gradually increase. The total running time for this test is 10 times more than at other orientations. At a 60˚ orientation (Figure 5-3C), the discharge rates fluctuate whereas at vertical inclination 90˚ (Figure 5-3D) the discharge rates decrease. At high flow meter discharge rates (Figure 5-4A-D), trends of the cumulative inflow or outflow volume and water loss values are similar, whereas the discharge rates fluctuate differently at different angles of inclinations for the shale sample.

The inflow-outflow volume and water loss at low and high flow meter discharge rates obtained for quartzite have similar trends (Figure 5-5 and Figure 5-6). However, the total running time for the falling head permeability tests at low flow meter discharge rates is approximately double the total time for tests at high flow meter discharge rates. The volume of water that seeps through the fracture is approximately equal to the outflow volume. Consequently, there is little water remaining in the fracture after each test.

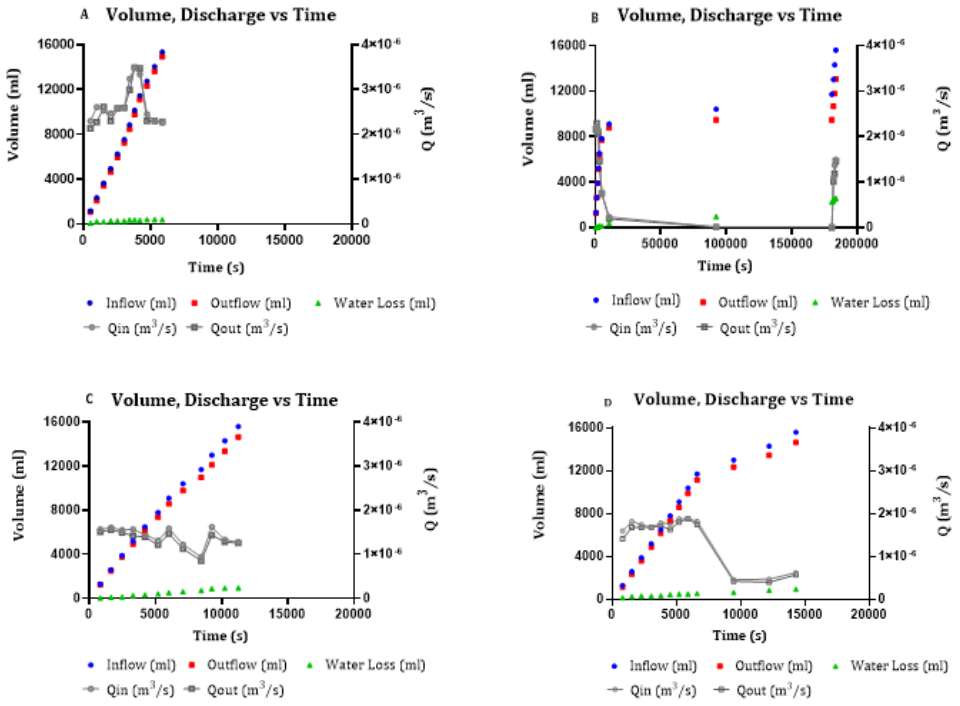

Figure 5-3: Volume, discharge and time graphs for shale at low flow meter rates for (A) 0˚(horizontal), (B) 23˚, (C) 60˚, (D) 90 ˚ inclination.

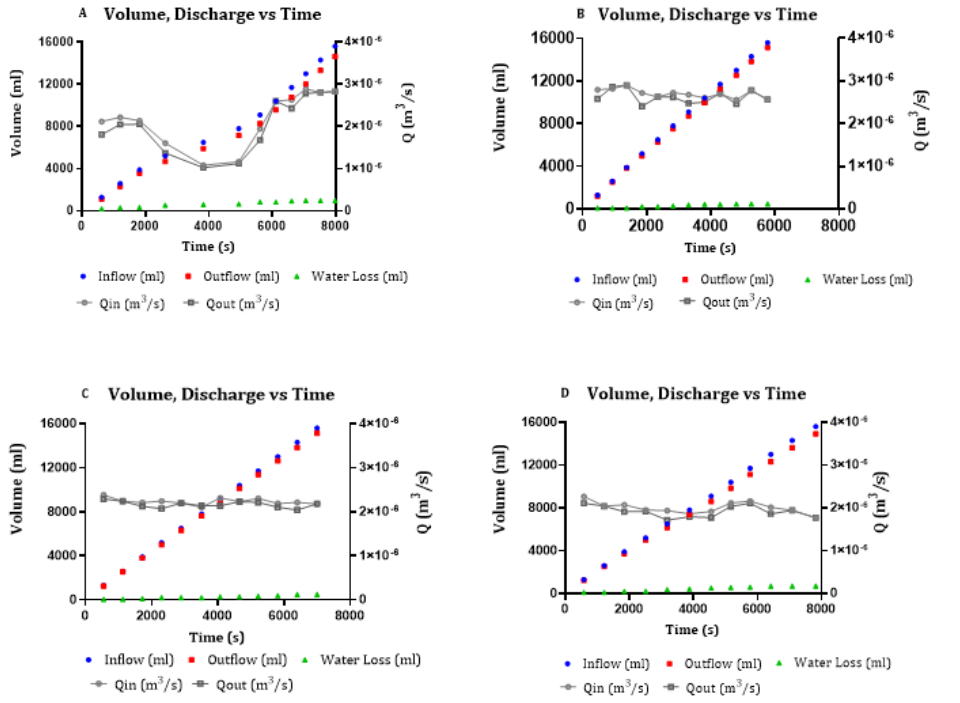

Figure 5-4: Volume, discharge and time graphs for shale at high flow meter rates for (A) 0˚(horizontal), (B) 23˚, (C) 60˚, (D) 90˚ inclination.

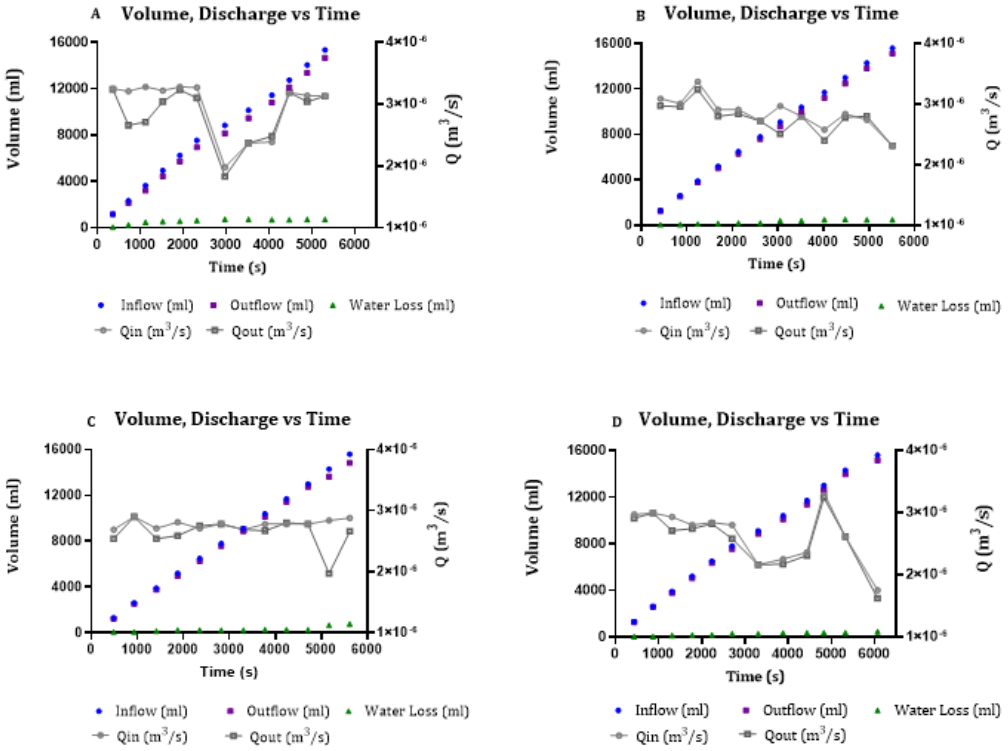

Figure 5-5: Volume, discharge and time graphs for quartzite at low flow meter rates for (A) 0˚ (horizontal), (B) 23˚, (C) 60˚, (D) 90˚ inclination.

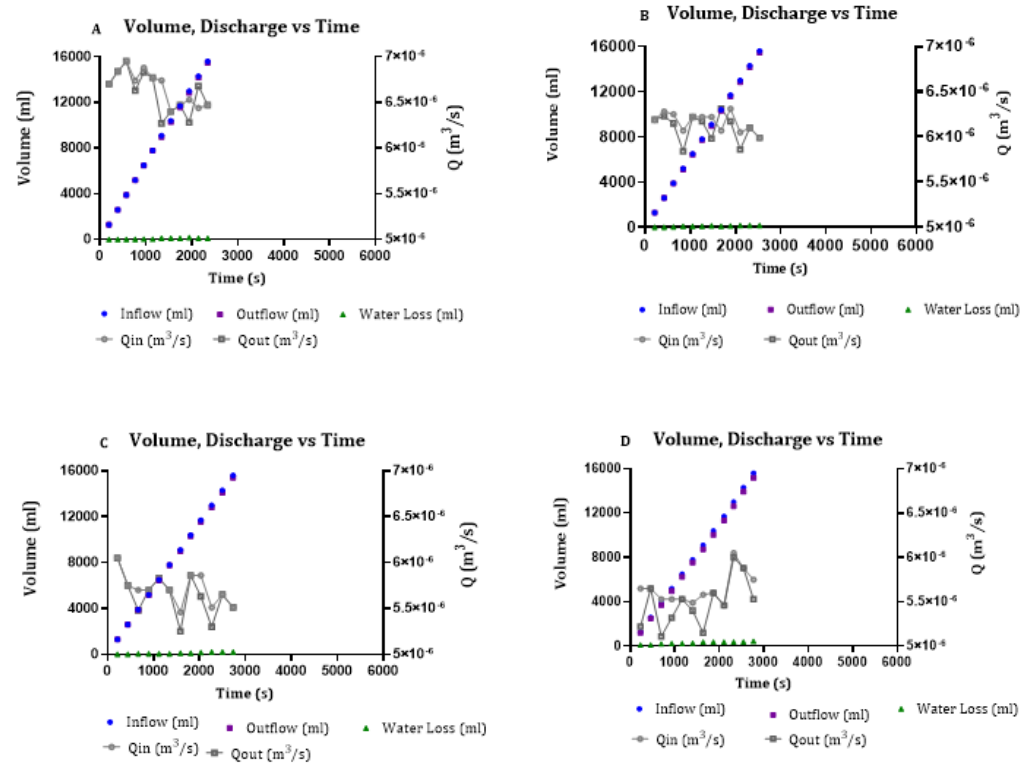

Figure 5-6: Volume, discharge and time graphs for quartzite at high flow meter rates for (A) 0˚ (horizontal), (B) 23˚, (C) 60˚, (D) 90˚ inclination.

5.3. Moisture Content and Hydraulic Conductivity

The hydraulic conductivities and moisture contents for each sample are determined empirically from the falling head permeability tests for the different angles of inclination. For each sample, the results show that the hydraulic conductivity *K* is directly proportional to the moisture content. Shale (Figure 5-7) has low hydraulic conductivities and higher moisture contents in comparison to quartzite (Figure 5-8). Both rock specimens have the highest moisture contents when placed horizontally. The moisture contents and hydraulic conductivities for both the samples orientated at 23°, 60°, and 90° inclination follow no particular order.

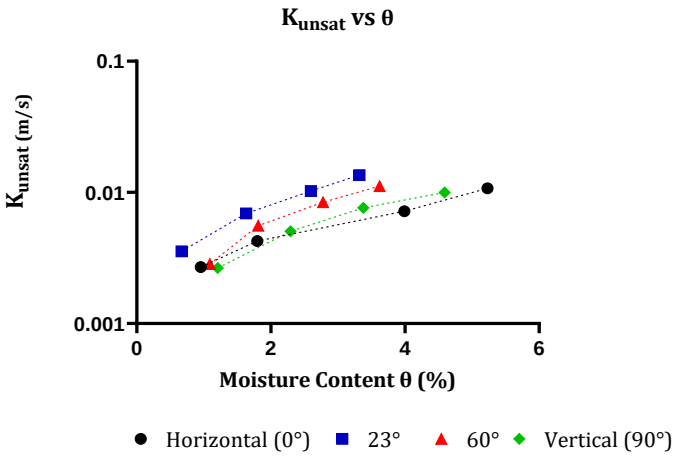

Figure 5-7: Unsaturated hydraulic conductivity of shale as a function of moisture content graph.

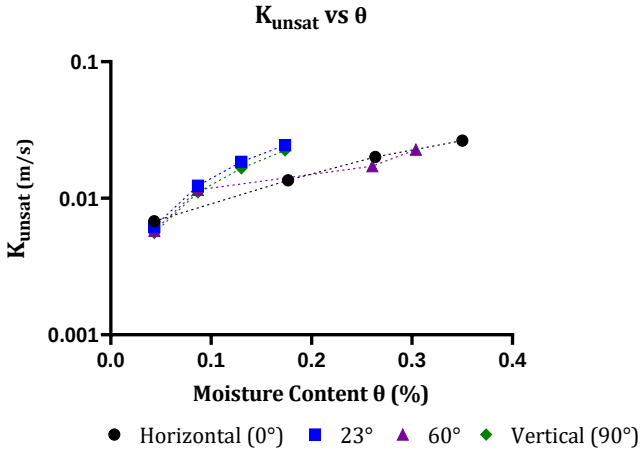

Figure 5-8: Unsaturated hydraulic conductivity of quartzite as a function of moisture content graph.

Chapter 6 Results: Composition and Geometry

6.1. Bulk Composition

The mineral phase composition of shale and quartzite is determined using X-Ray diffraction analysis. The phases on the peak graphs produce an inimitable diffraction pattern, and the relative phase amounts from the peak graphs of the rock specimens are estimated (Figure 6-1 and Figure 6-2). Table 6-1 provides the weight percentages for the different minerals present in both rocks. Shale is composed of quartz, muscovite and clinochlore (member of the chlorite mineral group). Quartzite is predominantly composed of quartz, biotite and magnetite.

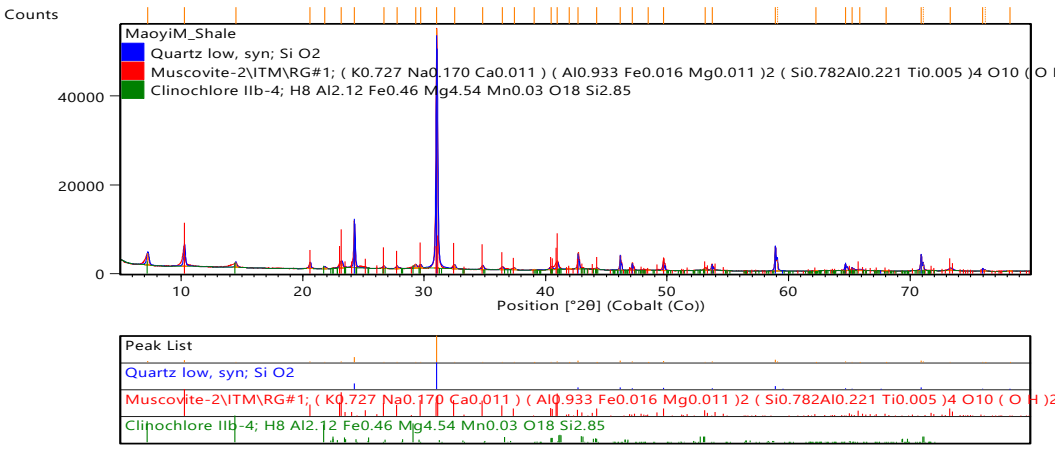

Figure 6-1: Shale diffraction patterns obtained from XRD analysis.

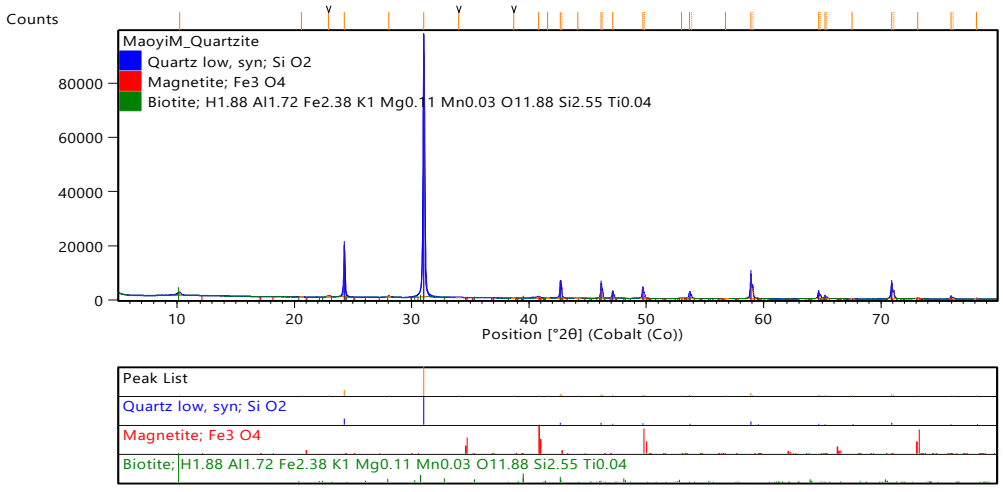

Figure 6-2: Quartzite diffraction patterns obtained from XRD analysis.

Table 6-1: Bulk mineralogical rock composition of shale and quartzite obtained from XRD analysis.

Shale		Quartzite	
Mineral	**Weight %**	**Mineral**	**Weight %**
Quartz	62.26	Quartz	98.07
Muscovite	28.17	Biotite	1.04
Clinochlore	9.57	Magnetite	0.89
TOTAL	100		100

6.2. Porosity

The porosity of each sample is determined by using the results obtained from the mineral weight phase percentages (XRD data). Table 6-2 provides all the parameters used to calculate the porosity, and the results thereof. The porosity of shale is 14.85%, and the porosity of quartzite is -7.64%. The calculated porosity of quartzite is a negative value and porosity cannot be negative because it ranges between 0-90% (Gonzalez de Vallejo and Ferrer, 2011). The bulk dry density is greater than the density of the solids and this implies the mineral density used for quartz is too low.

Table 6-2: Porosity test results.

Sample	M_{dry} (kg)	V_{bucket} (m^3)	V_{sub} (m^3)	ρ_B (kg/m^3)	ρ_s (kg/m^3)	f_M		n (%)
Shale	4.135	0.006	0.0078	2297.2	2697.889	Quartz	62.26	14.85
						Muscovite	28.17	
						Clinochlore	9.57	
Quartzite	11.525	0.008	0.012	2881.5	2676.93	Quartz	98.07	7.64
						Magnetite	0.89	
						Biotite	1.04	

6.3. Flow Regimes and Joint Roughness Coefficient

The relative roughness is related to the Reynolds number (see Appendix A), quotient of maximum amplitude, and average aperture of fracture. These variables infer whether flow in fractured systems will be laminar or turbulent; and whether the flow streamlines within the fractures will be rotational or irrotational.

The range of Reynolds numbers for shale at low flow meter discharge rates approach the critical value (i.e. 2300) needed for turbulence. As a result, flow is described as transitional turbulent flow. On the contrary, at high flow meter discharge rates the calculated Reynolds numbers exceed the critical values and flow is described as turbulent. Quartzite Reynolds numbers for low flow meter discharge rates indicate

laminar flow whereas, for high flow meter discharge rates the Reynolds numbers indicate turbulent flow.

Table 6-3 presents the results of the average aperture of each fracture in the lateral and longitudinal direction (Figure 6-3), the quotient of maximum roughness amplitude area, and relative roughness. The overall average aperture width of quartzite is larger than that of shale. The relative roughness ratios are greater than 0.32 in the lateral and longitudinal direction for both samples, as a result, flow is rotational.

Table 6-3: Relative roughness calculation results.

Sample	2ai= average aperture of fracture (mm)		Quotient of maximum roughness amplitude area, k (mm)		Relative roughness k/Dh= k/(2*2ai)	
	Lateral	Long.	Lateral	Long.	Lateral	Long.
Shale 1	0.42	0.69	0.03	0.32	0.036	0.2318
	0.16	0.44	0.06	0.1	0.1875	0.1136
Shale 2	0.71	0.70	0.33	0.51	0.2323	0.3643
	1.48	0.89	0.16	0.16	0.0541	0.0899
Quartzite 1	1.46	1.94	0.35	1.06	0.119	0.273
	1.64	1.61	0.16	0.51	0.049	0.158
Quartzite 2	1.04	1.02	0.89	0.09	0.428	0.044
	1.003	2.27	0.23	0.835	0.085	0.184

*Long.= longitudinal

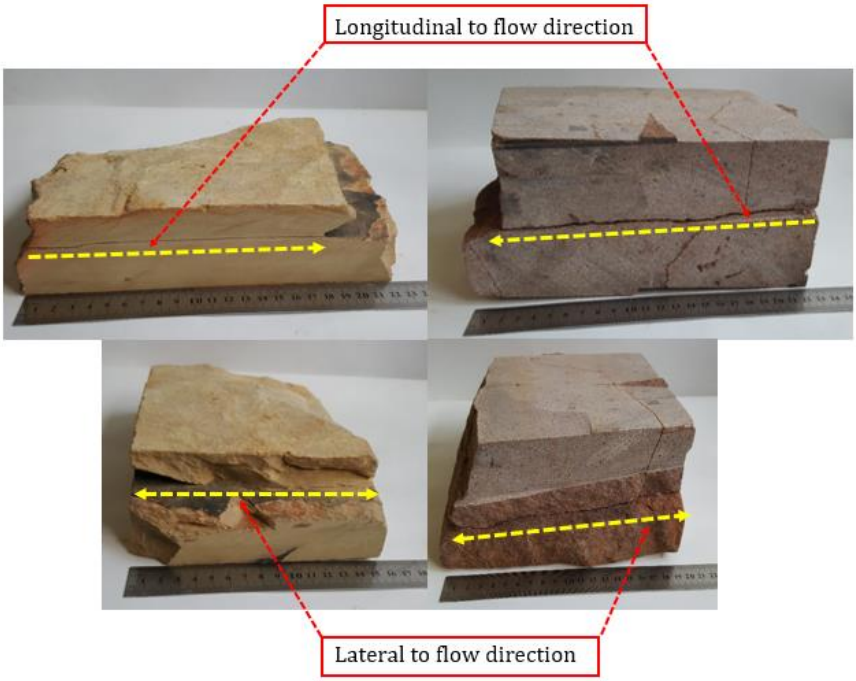

Figure 6-3: Shale and quartzite longitudinal and lateral flow direction.

The joint roughness coefficient (JRC) of each fracture surface was determined using two empirical equations proposed by Bandis et al. (1981) and Barton (1982) (Table 6-4). The method of Bandis et al. (1981) determines the roughness of the upper and lower fracture walls. The method of Barton (1982) determines the joint roughness from the average asperity amplitude and measured length. As such, one lateral and one longitudinal aperture was chosen to represent all four sides of the rock specimen. The smaller dimensions of shale and quartzite (i.e. 1 and 2) are well within the scale of the Barton and Choubey (1977) chart. Shale 1 has the same JRC for the upper and lower fracture surface. The upper fracture plane of Shale 2 has a higher JRC than its lower surface. On the other hand, the lower fracture surfaces of quartzite have higher JRC's than the upper surface. The 2D JRC estimation methods result in similar values. However, there are some anomalous joint roughness coefficients from the Barton (1982) method.

Table 6-4: Joint roughness coefficient results.

	$JRC = JRC_0 \left(\frac{l}{l_0}\right)^{-0.02JRC_0}$ **Bandis et al. (1981)**		$JRC = 400\frac{a}{L}$ **Barton (1982)**	
Shale 1	1.664	1.664	1.28	0.4
Shale 2	1.774	3.147	2.04	0.64
Quartzite 1	4.60	4.18	4.24	2.04
Quartzite 2	3.148	3.706	0.36	3.34

6.4. Summary of Overall Results

The tables below provide an overall summary of the obtained results for this study. This includes the cumulative moisture content, cumulative hydraulic conductivity, and average aperture in the longitudinal and lateral direction. The average roughness coefficient, flow mechanisms and regimes at the different angles of inclination are also included.

Table 6-5: Summary of overall results obtained for shale

Sample	Parameters				Geometry				Flow Behaviour	
	Angle	Average linear velocity, q (m/s)	Cumulative Moisture Content (%)	Cumulative Hydraulic Conductivity (m/s)	Average Aperture (mm)		Average Joint Roughness Coefficient		Flow Mechanism and Regime	
					Lateral	Long.	Bandis et al. (1981)	Barton (1982)	Mech.	Regime
Shale	0°	0.02-0.01	5.229	0.0107	0.29 (Shale 1)	0.565 (Shale 1)	1.664 (Shale 1)	0.84 (Shale 1)	Finger Flow	Low flow meter rates: Transitional turbulent rotational flow
	23°	0.03-0.02	3.322	0.0135						
	60°	0.02	3.6213	0.011	1.095 (Shale 2)	0.795 (Shale 2)	2.461 (Shale 2)	1.34 (Shale 2)		High flow meter rates: Turbulent rotational flow
	90°	0.02- 0.01	4.589	0.0099						

- These are average values and can be back calculated from the results chapters (i.e. 5 and 6) and raw data in the appendices.
- Long.= Longitudinal
- Mech. = Mechanism

Table 6-6: Summary of overall results obtained for quartzite

Sample	Parameters				Geometry				Flow Behaviour	
	Angle	Average linear velocity, q (m/s)	Cumulative Moisture Content (%)	Cumulative Hydraulic Conductivity (m/s)	Average Aperture (mm)		Average Joint Roughness Coefficient		Flow Mechanism and Regime	
					Lateral	Long.	Bandis et al. (1981)	Barton (1982)	Mech.	Regime
Quartzite	0°	0.07-0.06	0.35	0.026	1.55 (Qtz 1)	1.76 (Qtz 1)	4.39 (Qtz 1)	3.14 (Qtz 1)	Film Flow	Low flow meter rates: Laminar rotational flow
	23°	0.07- 0.05	0.17	0.025						
	60°	0.06-0.05	0.30	0.022	1.02 (Qtz 2)	1.65 (Qtz 2)	3.427 (Qtz 2)	1.85 (Qtz 2)		High flow meter rates: Turbulent rotational flow
	90°	0.06-0.05	0.17	0.022						

- These are average values and can be back calculated from the results chapters (i.e. 5 and 6) and raw data in the appendices.
- Qtz= Quartzite
- Long.= Longitudinal
- Mech. = Mechanism

Chapter 7 Discussion

7.1. Visual Observations

Water is introduced into the point source of each sample and exits the fracture under free-draining conditions. The rate of imbibition in both the samples in the distinct phases is minimal, due to low matrix permeability and possible surface coatings on the fracture surfaces as also found by Montazer and Wilson (1984) and Pruess (1999). Preferential flow prevails in both samples and, as a result, imbibition into the pore spaces is reduced. Hysteric effects are more prominent when water resists imbibition under partially saturated conditions.

The water spreading on the fracture walls of both the samples replicates hydrophilic behaviour at a contact angle of less than 90˚. Doe (2001) explicitly states the contact angle is assumed to be 0˚ when the fluid spreads on the surface. However, the fluid spreads on both the samples but the minerals present in the rocks have different wetting properties. Surface roughness also enhances the wetting behaviour. Wetting on the shale fracture surface and its side wall are in the form of drops. The observed drops are theoretically classified as fingers or finger-tips because water spreads on the surface leaving wetted flow paths behind. The finger formation in the shale indicates unstable infiltration of water into the sample; this mechanism may also accelerate flow while sustaining capillary saturation. Alternating cycles of wet and dry flow paths are also observed, which is consistent with the studies of Su (1999) and Brouwers and Dippenaar (2018) that describes this as intermittent flow, where one cycle of a finger snaps, reforms, and then snaps again. Continuous threads of water with sufficient fluid mass exit the quartzite fracture as films. Water drains faster in the quartzite fracture as per Tokunaga and Wan (1997), whereby film flow will result in rapid infiltration of water into the unsaturated zone.

Flow occurs in the lateral and longitudinal direction, forming either flow paths or wetting fronts for all orientations. A fluid finger or film will either flow in the direction of the gravitational potential; or, as water flows along the fracture, gravity destabilises it and the fluid gravitates vertically downwards, as stated by Nicholl and Glass (2007). This demonstrates that there is less capillarity, and more gravitational drainage in both samples for all angles of inclination.

The observed flow patterns in both samples indicate inconsistent flow path sequences, formation of new flow paths, or merging of flow paths for all the phases. The flow mechanisms remain the same during the distinct phases (i.e. initially dry, wetting, and rewetting phases, respectively). Water from the initially dry phase creates persistent pathways for the wet and rewetting phase, where water will keep on rewetting the preceding flow paths (as per Glass et al., 1995). This results in an increase in the dispersion of the wetting front and flow paths widen as more water rewets the initial flow paths. Su (1999) affirms that the flow paths for the initially dry phase will control infiltration behaviour at two scales. Firstly, the fluid is restricted within the pre-existing wetted flow path. Secondly, at a smaller scale, the flow path will be controlled by the spatial structure of the individual fluid clusters. This includes the direction and advancement of fingers or films, which will affect the fluid velocity, flow path width and the wetting front, consequently, the fluid will either split or merge. In some instances, static fluids (or pools) are observed at the aperture in either of the wetting phases (i.e. initially dry, wet, and rewetting). After a critical fluid mass is reached, the fluid moves individually or in small fluid clusters that move as a compact body on the fracture aperture. This is supported by Dragila and Weisbrod (2003), who found that surface wetting provides for changes in flow discharge by changing fluid thickness, correlating with the change in speed.

When quartzite is orientated at 23°, there are large air pockets (air bubbles) at the outlet fracture, possibly indicating bubble flow within the fracture. The flow pattern within the fracture cannot certainly be defined because the rocks are not transparent. The two-phase occurrence of fluids for other orientations for quartzite and all angles for shale can either be stratified flow when both air and water are continuous, or mixed flows when one phase (water or air) is continuous within the fracture. Two-phase flow within fracture is also governed by the velocity of air or water, their interaction, change in pressure, and the surface geometry of the fluid flow path.

7.2. Influence of Geometry

Geometric intricacies play an integral part in flow anisotropy. The chosen angles of inclination provide a general overview of rock mass geometry. The Reynolds number is a function of discharge and is inversely proportional to the fracture aperture. Merging the results of the Reynolds numbers and the relative roughness ratios, the flow regime at the 20 m*l*/min flow meter for shale is transitional turbulent rotational flow and laminar rotational flow for quartzite. Conversely, for the 200 m*l*/min (shale) and 500 m*l*/min (quartzite) flow meter, the flow regime is turbulent rotational flow. The increase in Reynolds numbers demonstrates significant inertial forces and non-Darcian flow (as defined by Ranjith and Darlington, 2007). The fracture walls are classified as hydraulically rough because the results indicate rotational flow. Furthermore, the Reynolds number increases with increasing fracture roughness and the fracture walls will diverge the flow streamlines which induces turbulence and flow tortuosity.

The joint roughness coefficient (JRC) values were determined using two different measuring techniques. This includes the laboratory micro-roughness empirical equation of Bandis et al. (1981), and the average maximum amplitude along a measured length of Barton (1982). The obtained JRC-values for shale and quartzite range between the first and third standard profiles of the Barton and Choubey (1977) chart. Fracture walls of shale and quartzite are not identical, as the JRC results varied except for Shale 1. In addition to this, the different 2D JRC method estimations yield similar results and some anomalous joint roughness coefficients. The anomalies are due to non-uniform asperity height differences along the aperture lengths from Barton's (1982) method. As emphasised by Gonzalez de Vallejo and Ferrer (2011), natural rocks are heterogenous and anisotropic, so anomalous results in this study are to be expected. Variations in the surface morphologies may create regions with lower wetting resistance, where the fluid deviates from the flow path as stated by Berkowitz (2002). Roughness induces turbulence from the onset and also accounts for flow channelling; this will also depend on the degree of roughness on the fracture surface. Rough-walled fractures result in variable aperture, which can lead to overestimation of flow when using the Cubic Law, as described by Tzelepis et al. (2015).

The rock fracture of each of the samples is clean, matched and tightly jointed. The aperture of the shale is narrower than that of quartzite. The aperture width influences

the observed flow mechanisms as tight discontinuities are more likely to have forces counteracting free water movement, therefore affecting the permeability. Moreover, capillary forces are favoured in narrower apertures, whereas larger gravitational forces are favoured in wider apertures.

Upon wetting, the left side of the of the fracture surfaces become wet and effects of contact bridging are evident, as the right side of the fracture surface remains dry (Figure 7-1). Water exits the fracture at certain channel points when orientated horizontally, and at 23°, as per Figure 7-1c. Conversely, at 60° and 90° inclination, water exits at the outlet fracture surface and minimal water wets the fracture walls (Figure 7-2). This is similar to the findings of Jones et al. (2018b) and Tokunaga et al. (2000), where flow in fractures will occur in depressions (channel points) where the fluid will easily invade, whilst contact obstacles constraint flow. Once the fluid breaches the contact obstacle at a certain elevation, the fluid will spill into the next channel point or depression. In vertical fractures (Figure 7-2), the contact obstacles control the flow paths, and the fluid will migrate between the fluid bridges around the contact obstacles. Furthermore, contact obstacles delay the flow path lengths; hence, water drains faster, travelling in straight line paths in larger surface areas, with minimal channel points.

It is understood that the geometry of the rock fractures will affect fluid flow due to the change in aperture, roughness and contact obstacles. Based on the visual observations of this study, the angle of inclination of the rock mass will also influence the development of the flow patterns that form in fractured rocks.

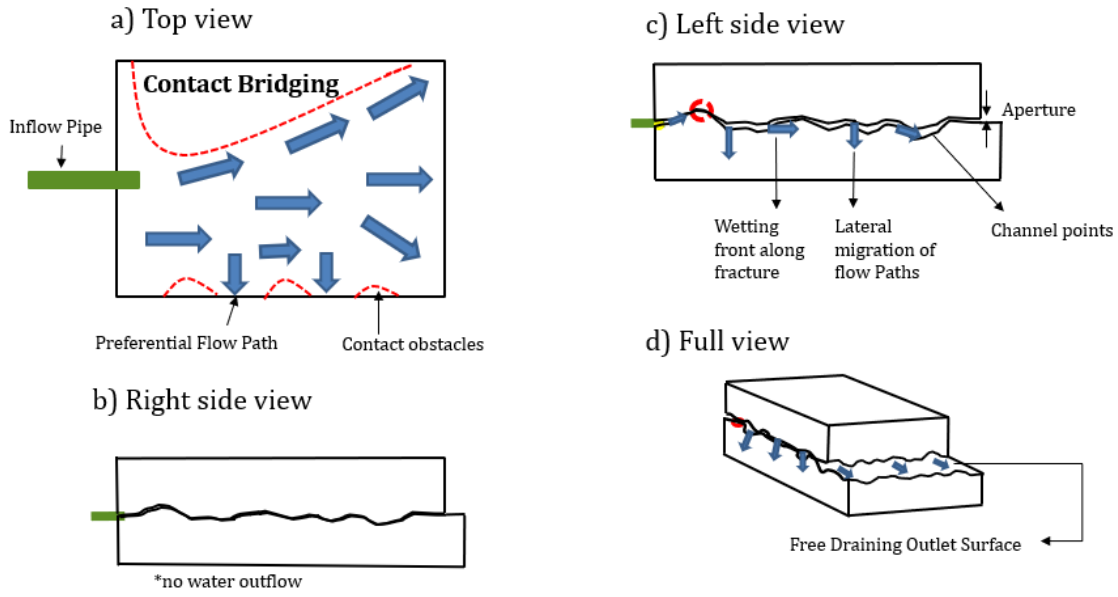

Figure 7-1: Schematic representing the observed preferential flow paths in natural fractured systems at 0° and 23° inclination as follows : (a) the water preferentially flows on the fracture surface and the contact points restrict the water flow; (b) there is no water outflow on the right-side as the fracture is tight; (c) water exits the fracture aperture at certain channel points; (d) water freely draining on the outlet fracture surface.

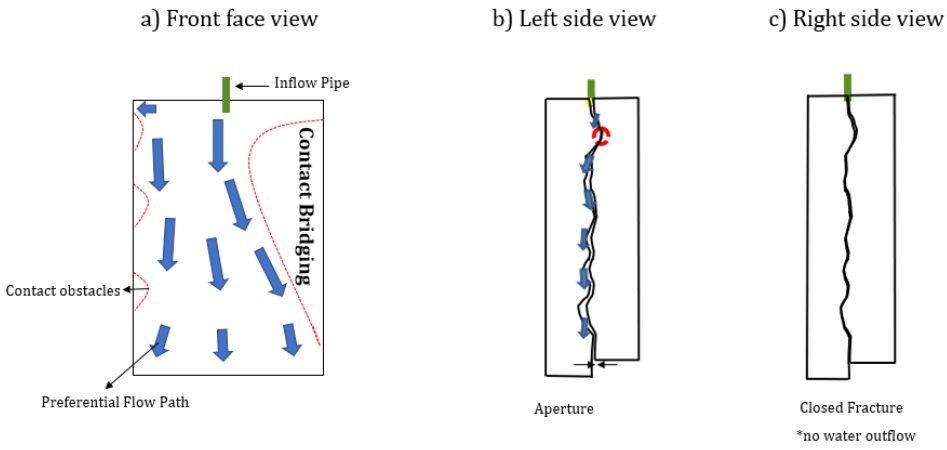

Figure 7-2: Schematic representing the observed preferential flow paths in natural fractured systems at 60° and 90° inclination as follows: (a) the water first exits from the middle of the fracture then progresses laterally to the left then to the right (b) water flows along the fracture (c) there is no water outflow on the right-side as the fracture is tight.

7.3. Quantitative results

The hydraulic head and the cumulative volume data plot well within the regression line, showing a good relationship between the samples and the response variable (Figure 5-1 and Figure 5-2). The hydrostatic head of this sample is measured at 1 m and, as anticipated, the flow rate is high at higher hydraulic gradients, and reduces as the hydraulic head decreases.

When the static pressure decreases, flow increases. The change in hydraulic head characterises the change in the potential energy of water flow, as defined by Bernoulli's principle. There is also a change in area as the water flows from a 6 mm diameter pipe into the rock fracture; in achieving continuity, the velocity will change inversely proportional to the width of wetting perpendicular to the flow direction, as indicated by Jones et al. (2018a).

The hydraulic head decreases at a similar rate for the initially dry, wet or rewetting phase. The retention of water in the fracture will also depend on adhesion and time interval the water is in contact with the solid despite the phase (i.e. initially dry, wet and rewetting). In addition to this, the average linear velocities at different orientations are similar and, therefore, the angle of inclination does not accelerate the flow rate. As the fracture permeability and hydraulic gradient remain unchanged, it is expected that the average flow rate should remain unchanged, albeit possible to have different linear flow velocities related to different degrees of saturation (again, as per continuity principle).

The calculated discharge rates are well within the same order of magnitude. There is a lag between the cumulative discharge rate for water inflow (Q_{in}) and outflow (Q_{out}), representing the wetting of the fracture. The duration of the test takes longer for flow meters with 20 ml/min rates compared to the flow meters of 200 ml/min and 500 ml/min rate, implying that the flow meter controls the flow rate at low discharge rates, while at higher discharge rates, influx depends on the permeability of each of the samples. A linear relationship exists between time, inflow and outflow volume, whereas water loss is very minimal. Not all the water drains out of the fracture at the same time, with some being retained and exiting the fracture with the next phase readings, likely requiring higher cohesive forces to overcome adhesive forces trapping some moisture

in the fracture. Consequently, negative water loss values are recorded because the total outflow volume is higher than the total inflow volume.

Shale acts a double porosity medium with a porosity of 14.85%, where there is storage in the matrix and transmission of water through the fracture. Fracture flow predominates in the quartzite, with a porosity of -7.64%, where the fracture acts both as storage and transmits flow. Porosity accounts for the water loss values, measures the void spaces in rocks and cannot be negative. The porosity of quartzite can be 7% (Hirth and Tullis, 1989), or the primary porosity for the quartzite might be close to absolute zero. This depends on many factors, including mineral density, method of quantification, rock composition, aperture, and fracture porosity. Furthermore, the calculated porosity of both the samples may change based on the chosen scale, that is, the size of the intact rock and number of fractures present in the rock mass, and volume of investigation as defined by the representative elementary volume (REV) model (Barenblatt et al., 1960; Bear, 2007).

The most notable water loss is in shale when inclined at 23˚. Water infiltrates, gets stored in the pore spaces and there is no transmission of water through the fracture. In addition to this, at 60˚, the duration of the test is longer as some of the water imbibes into the matrix pores and the discharge rates (Q_{out}) decrease. The two matrix imbibition events on the shale sample cannot be regarded as outliers; in fact, they could be triggering mechanisms for complex unsaturated zone conditions, such as a sudden increase in excess pore water pressures. This raises questions as to what happens during infiltration events, or flash floods in fracture flow, because the moisture content when imbibition will commence in fractured low permeability materials under partially saturated conditions is still unknown. Knowledge of moisture thresholds to determine when water will imbibe or gravitate will help with predicting unsaturated zone flow models (as per Dippenaar and Van Rooy, 2018).

The hydraulic conductivity is governed by pore and throat sizes, and their connectivity available for retaining water. The quartzite has a wider aperture than the shale and yields higher hydraulic conductivities and lower moisture contents. Aperture does influence the hydraulic conductivity of the samples, and shale has more small pores and possible charged minerals, which will promote more adhesion. The natural moisture content of the samples changes due to cycles of wetting and drying, and little variation

is seen in the overall hydraulic behaviour (except for shale inclined at 23°). The obtained hydraulic conductivities of the fractures (K_f) for both samples are in the order of 10^{-3} m/s, with varying moisture. Theoretically, the hydraulic conductivity is a function of moisture content. As the porosity is less than the moisture content, the unsaturated hydraulic conductivity is not equal to the saturated hydraulic conductivity, and full saturation is not reached (e.g. Das, 2008; Dippenaar et al., 2014).

Chapter 8 Conclusions

8.1 Assumptions and Limitations

This research is limited to two natural rock samples that have similar dimensions and different mineralogical compositions. Natural rocks are not transparent, as a result, the preferential flow paths on the fracture surface cannot be observed visually. However, the flow mechanisms are deduced when the water exits the fracture on the sidewalls and is understood in the context of previous studies by other authors conducted with transparent acrylic specimens.

Pipes with the same diameter (6 mm) and flow meter tubes were used for the falling head permeability test for shale and quartzite. The effect of frictional losses in the pipe, connections between the tubes and pipes, entry and exit points are assumed to be constant for all experiments and not considered. Moreover, the fluid is assumed to be non-viscous, and thus, internal friction that may reduce the energy is assumed to be constant. In-situ stress conditions, confining pressures and fluid pressures are equally important in natural rock fracture flow. However, these are beyond the scope of this study and are assumed to be consistent.

Samples are dried at 105℃ because at this temperature, it is assumed that all the water from the rock is removed without altering the chemical and physical characteristics of the samples.

Porosity values are not entirely accurate, and results will be influenced by deviations from values used. However, porosity itself will only truly affect imbibition and reasons for water losses and does not significantly affect the flow observed and flow rates determined.

8.2 Summary

Partially saturated flow through natural rock fractures is a complex topic, due to factors affecting water movement in the unsaturated zone, as well as the anisotropic and heterogenous nature of rocks. Falling head permeability tests are conducted to evaluate flow through single natural fractures. Samples used for this study include a shale sample obtained from the Timeball Formation of the Pretoria Group, and a quartzite sample from the Swaershoek Formation of the Waterberg Group, South Africa. Rock

specimens are tested for different angles of inclination, that is, 0˚, 23˚, 60˚, and 90˚, under continuous influx conditions. Experiments are performed under high and low flow meter discharge rates to evaluate flow. In each test, samples are wetted from initially dry, wetting, and to rewetting phase conditions. Samples are then oven dried, and the cycle is repeated.

Visual observations show that water preferentially flows on the fracture surfaces in the lateral and longitudinal direction, despite the different rock mineralogical compositions. Water spreads on the surface of the rock specimens at a contact angle of less than 90˚, resulting in either finger (s) for shale and films (s) for quartzite. The flow mechanisms indicate fluid instabilities and rapid infiltration of water under unsaturated conditions. Fluid flow in the wetting and rewetting phase forms new flow paths or follow the pre-existing wetted flow paths from the initially dry phase. As a result, flow paths merge, widen and or there is an increase in the dispersion of the wetting front. The advancement of the flow paths and wetting front will mainly depend on the fluid mass, its velocity and angle of inclination. The preferential flow paths in these natural systems are similar to those observed in parallel plates experiments by Jones et al. (2018b). It is difficult to deduce the type of flow that occurs within the fracture, because natural rocks are not transparent. Typical flow patterns within a rock fracture, stratified or mixed flow patterns, may occur within the fracture depending on the air-water interaction.

Geometric intricacies, such as roughness, aperture variability, contact obstacles, and angle of inclination have an influence on the observed flow behaviour. In wider apertures, water flows easily and more fluid drains from the fracture. Therefore, gravitational forces are dominant in quartzite and capillary forces are significant in the shale sample that has a narrower aperture. Contact obstacles constrain flow in rock specimens orientated horizontally (0˚) or at 23˚. In contrast, at 60˚ or vertical inclination, contact obstacles control the flow paths, where the fluid moves in-between the fluid bridges that occur around contact obstacles. The location of topographic depressions or ridges, which act as channel points or contact obstacles, depend on the degree of roughness and geometry of fracture surfaces.

The joint roughness of the fracture surfaces in both samples are determined through two methods, as proposed by Bandis et al. (1981) and Barton (1982), respectively. The calculated joint roughness coefficients are between 0-6 for both samples, with standard

roughness profiles ranging between the first and third profile of the Barton and Choubey (1977) chart. There are anomalous joint roughness coefficients obtained from the rock specimens; however, this is expected because natural rocks are not homogenous nor isotropic. Furthermore, 2D estimation of JRC needs further refinement in order to more accurately estimate the effects of geometric controls on flow behaviour in anisotropic media.

The Bernoulli principle accounts for the change in the hydraulic head for the falling head permeability test. The continuity principle applies to the change in flow area of water flow through the water supply inlet that is connected to the inlet pipe, and the inlet pipe is inserted into the rock fracture. The discharge rates of the low and high flow meters discharge rates are within the same order of magnitude. The duration of the tests is longer in the 20 m*l*/min flow meters compared to the flow meters of 200 m*l*/min and 500 m*l*/min. The flow meter at low discharge rates controls the rate of flow, whereas at higher discharge rates, influx depends on the permeability of each of the samples.

Results both qualitatively and quantitatively provide evidence for a double porosity system, especially for the shale. Water is stored in the pore spaces, while the fracture itself acts both as storage space and transmits flow. The water loss percentages are in the range of 8.46-23.2% for shale, and 14.15-17% quartzite, excluding the 100% water loss in shale inclined at 23˚.

Discharge rates decrease when water imbibes into the pore spaces. Reynolds numbers are dependent on the discharge rates and are also affected by the aperture width. In rough-walled discontinuities, the flow tends to transition from laminar to turbulent flow, meaning that the Cubic Law is invalid in such cases. At low discharge rates, the Reynolds numbers for shale indicates transitional turbulent rotational flow and laminar rotational flow for quartzite. At high discharge rates, the flow regime is turbulent rotational flow. Quartzite yielded higher discharge rates than shale, but the aperture width affected the calculated Reynolds number. As the Reynolds numbers increase, inertial effects are of importance and the fracture does not show Darcian behaviour.

8.3. Main Findings

The fundamental concepts addressed in this study are intertwined, as depicted in Figure 8-1. Partially saturated flow through natural single fractures is affected by the properties of the geologic media, including the mineralogical composition, geometrical intricacies (i.e. orientation, aperture, roughness, and stress regime), as well as surface wettability and porosity, which will ultimately influence the flow mechanisms and regimes.

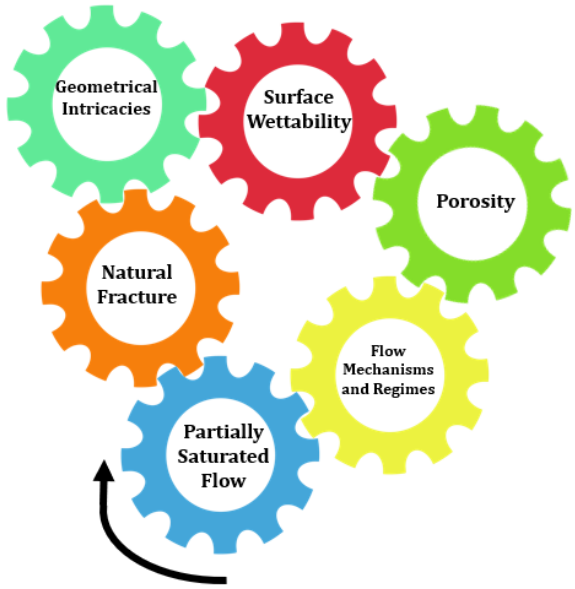

Figure 8-1: Fundamental Concepts

For example, two samples that have the same mineralogy and the rate of influx into the fracture, will have similar surface wetting properties. The contact angle between the fracture surface and water will depend on the competition between adhesion and cohesion or spreading of fluid in the fracture. If cohesion dominates, flow mechanisms such as drops or rivulets are expected, whereas, when the fluid spreads on the surface due to adhesion, the flow mechanisms are to be defined as films, or fingers.

The representative elementary volume distinguishes porous medium properties, which vary spatially and temporarily, depending on the system boundary conditions (REV, Barenblatt et al., 1960). If two similar natural single fractures without any random pore heterogeneities are under investigation, the porosity will be the same; however, if the volume of scale of one sample is extended, the porosity may change based on the microscopic and macroscopic heterogeneities.

Fractured rocks behave as double porosity media. Primary porosity is known to store water, while secondary porosity transmits water. In low permeability matrix materials, imbibition into primary porosity may occur at certain moisture contents. When flow occurs through fractures at some moisture threshold, infiltration into the interstitial porosity occurs, which will result in low discharge rates affecting the flow regime.

In rough-walled discontinuities, flow tends to transition from laminar to turbulent flow. Relative roughness ratios may be applied to further classify the streamlines when flow is laminar or turbulent. When flow is influenced by the fracture walls, the streamlines diverge, known as rotational flow and vice versa for irrotational flow. Stress changes in the rock mass will either increase or decrease the aperture width, and cause a change in permeability. This will affect the discharge rates, influence the distribution of the hydraulic head, and affect the seepage forces acting on the rock mass. The dip of the rock mass will also have an effect on the observed flow patterns.

8.4 Way Forward

Insight into unsaturated flow through discreet natural rock fractures aid in improved understanding of groundwater recharge and contamination, reduction in shear strength of wet fractures in rock mass, and possible solutions to the drainage of rock slopes and excavations. In order to truly understand the influence of fracture geometry on flow, more complex experimental work entailing differing aperture, roughness and infill will be beneficial. This needs to be validated and upscaled at field level as the results of this study are aligned to what has previously been observed by authors (e.g. Jones et al. 2018a) in smooth parallel acrylic plate models progressively built into more complex systems.

References

Abdassah, D. & Ershaghi, I., (1986). Triple porosity system for representing naturally fractured reservoirs. *SPE Formation Evaluation*, 1(2), pp. 113-127.

Aydin, A., 2001. Fracture void structure: implications for flow, transport and deformation. *Environmental Geology International Journal of Geociences,* 40(6), pp. 672-677.

Bai, M., Meng, F., Roegiers, J. C. & Abousleiman, Y., (1998). Modellling two-phase fluid flow and rock deformation in fractured porous media. In: J. F, et al. eds. *Poromechanics.* A.A. Balkema; Rooterdam, pp. 333-338.

Bandis, S., Lumsden, A. C. & Barton, N. P., (1981). Experimental studies of the shear behaviour of rock joints. *International Journal of Rock Mechanics and Mining Sciences,* 18, pp. 1-21.

Barenblatt, G. I., Zheltov, I. P. & Kochina, I. N., (1960). Basic concepts in the theory of seepage of homogeneous liquids in fissured rocks. *Journal of Applied Mathematics ,* 24, pp. 852-864.

Barton, N., (1973). Review of a new shear-strength criterion for rock joints. *Engineering Geology,* 7(4), pp. 287-332.

Barton, N., (1982). Modelling rock joint behaviour from in situ block tests: implications for Nuclear Waste Reposity Design., Columbus, Ohio: ONWI-308, ONWI.

Barton, N., Bandis, S. & Bakhtar, K., (1985). Strength, deformation and conductivity coupling of rock joints. *International Journal of Rock Mechanics and Mining Sciences & Geomechanics Abstracts,* 22(3), pp. 121-140.

Barton, N. & Choubey, V., (1977). The shear strength of rock joints in theory and practice. *Rock Mechanics ,* 10(1-2), pp. 1-54.

Barton, N. & De Quadros, E. F., (1997). Joint aperture and roughness in the prediction of flow and groutability of rock masses. *International Journal of Rock Mechanics and Mining Sciences,* 34, Paper No. 252.

Bear, J., (1988). *Dynamics of Fluids in Porous Media.* New York: Dover Publications.

Bear, J., (2007). *Hydraulics of Groundwater.* New York: Dover Publications.

Berg, J. C., (1993). Role of acid-base interactions in wetting and related phenomena. In: J. C. Berg, ed. *Wettability.* New York: Decker, pp. 75-148.

Berkowitz, B., (2002). Characterizing flow and transport in fractured geological media: A review. *Advances in Water Resources,* 25, pp. 861-884.

Bieniawski, Z. T., (1989). *Engineering Rock Mass Classifications*. John Wiley & Sons Inc.

Bo, A., Zhu, C., Kuiming, L., Sitong, L., Zhigang, T., Haipeng, L. & Haoran, Y. (2019). The influence of rainfall on landslide stability of an open-pit mine: The case of Haizhou open-pit mine. *Geotechnical and Geological Engineering.* https://doi.org/10.1007/s10706-019-00851-y.

Brouwers, L. B. & Dippenaar, M. A., (2018). Partially saturated flow from sand into a discrete smooth open vertical fracture at the soil-rock interface: experimental studies. *Bulletin of Engineering Geology and the Environment*. https://doi.org/10.1007/s10064-018-1258-x.

Carillo, M. L. K., Letey, J. & Yates, S., (2000). Measurement of initial soil-water contact angle of water repellent soils. *Soil Science Society of America Journal*, 63, pp. 433-436.

Cheng, C., Perfect C., Donnelly B., Bilheux H., Tremsin A., McKay L., DiStefano V., Cai J., & Santodonato L., (2015). Rapid imbibition of water in fractures within unsaturated sedimentary rock. *Advances in Water Resources*, 77, pp. 82-89.

Cherubini, C., Giasi, C. & Pastore, N., (2012). Bench scale laboratory tests to analyze non-linear flow in fractured media. *Hydrology and Earth System Sciences*. https://doi:10.5194/hess-16-2511-2012.

Cornwell, D. K. & Murphy, H. D., (1985). Experiments with non-Darcy flow in joints with large scale roughness. In: O. Stephansson, ed. *Proc Int Symp. on Fundamentals of Rock Joints*., pp. 323-334.

Das, B., (2008). *Advanced Soil Mechanics*. New York: Taylor & Francis Group.

Deer, W., Howie, R. & Zussman, J., (1996). *An introduction to the Rock-Forming Minerals*. Prentice Hall.

Dippenaar, M. A. & Van Rooy, J. L., (2016). On the cubic law and variably saturated flow through discrete open rough-walled discontinuities. *International Journal of Rock Mechanics and Mining Sciences*, 89, pp. 200-211.

Dippenaar, M. A. & Van Rooy, J. L., (2018). Vadose Zone Characterisation for Hydrogeological and Geotechnical Applications. In: Shakoor A. & Cato K. eds., IAEG/AEG *Annual Meeting Proceedings, San Francisco, California, 2018—Volume 2*. https://doi.org/10.1007/978-3-319-93127-2_10.

Dippenaar, M. A., Van Rooy J., Breedt N., Huisamen A., Muravha S., Mahlangu S. & Mulders J., (2014). *Vadose Zone Hydrology: Concepts and Techniques*, Pretoria: Water Research Commission.

Doe, T. W., (2001). What do drops do? Surface wetting and network geometry effects on vadose-zone fracture flow. In: National Research Council. eds. *Conceptual models of flow and transport in the fractured vadose zone*, pp. 243-270.

Dragila, M. I. & Weisbrod, N., (2003). Parameters affecting maximum fluid transport in large aperture fractures. *Advances in Water Resources*, 26 (12), pp. 1219-1128.

Durham, W. B. & Bonner, B. P., (1994). Self-propping and fluid flow in slightly offset joints at high effective pressures. *Journal of Geophysical Research*, 99(B5), pp. 9391-9.

Fitts, C. R., (2002). *Groundwater Science*. London: Academic Press.

Freeze, R. A. & Cherry, J. A., (1979). *Groundwater*. New Jersey: Prentice-Hall.

Gates, C., (2018). *Estimating Wettability of Rock Fracture Surfaces from Contact angle and Roughness Measurements*. MSc Dissertation, (unpub.). The University of Tennessee.

Gattinoni, P., Scesi, L. & Terrana, S., (2009). Water flow in fractured rock masses: numerical modeling for tunnel inflow assessment. *Geophysical Research Abstracts*, 11, EGU2009-468, 2009, EGU General Assembly 2009.

Glass, R. J. & Nicholl, M. J., (1996). Physics of Gravity Fingering of Immiscible Fluids within Porous Media: An overview of current understanding and selected complicating factors. *Geoderma*, 70, pp. 133-163.

Glass, R. J., Nicholl, M. J. & Tidwell, V. C., (1995). Challenging models for flow in unsaturated, fractured rock, through exploration of small-scale processes. *Geophysical Research Letters*, 22(11), pp. 1457-1460.

Gonzalez de Vallejo, L. I. & Ferrer, M., (2011). *Geological Engineering*. Leiden: CRC Press/Balkema.

Hirth G. & Tullis J., (1989). The effects of pressure and porosity on the micromechanics of the brittle-ductile transition in quartzite. *Journal of Geophysical Research: Solid Earth*, 94 (B12), pp. 17825-17838.

Hoek, E. & Bray, J., (1977). *Rock slope engineering*. 2nd Revised ed. The Institution of Mining and Metallurgy, London.

Hofmann, H., Blocher, G., Milsch, H., Babadagli, T., & Zimmerman, G., (2016). Transmissivity of aligned and displaced tensile fractures in granitic rocks during cyclic loading. *International Journal of Rock Mechanics & Mining Sciences*, 87, pp. 69-84.

Indraratna, B. & Ranjith, P., (2001). *Hydromechanical aspects and unsaturated flow in jointed rock*. A.A. Balkema.

ISRM [International Society for Rock Mechanics], (1981). *Rock Characterisation, Testing and Monitoring*. Brown, E. ed. Pergamon Press.

Jang, H. S., Kang, S. S. & Jang, B. A., (2014). Determination of joint roughness coefficients using roughness parameters. *Rock Mechanics and Rock Engineering*, 47(6), pp. 2061-2073.

Johnson, M., Anhaeusser, C. & Thomas, R., (2006). *The Geology of South Africa*. Pretoria: Geological Society of South Africa.

Jones, B. R., Brouwers, L. B. & Dippenaar, M. A., (2018a). Partially to fully saturated flow through smooth, clean, open fractures: qualitative experimental studies. *Hydrogeology Journal,* 26, pp. 945-961.

Jones, B. R., van Rooy, J. L. & Dippenaar, M. A., (2018b). On the Differing Role of Contact Obstacles on Variably Saturated Flow in Vertical and Horizontal Fractures. In: Shakoor A. & Cato K. (eds.), *IAEG/AEG Annual Meeting Proceedings, San Francisco, California, 2018—Volume 4*. https://doi.org/10.1007/978-3-319-93133-3_11

Knappett, J. A. & Craig, R. F., (2012). *Craig's Soil Mechanics*. New York: Spon Press.

Kovács, G., (1981). *Developments in Water Science: Seepage Hydraulics (Vol. 10)*. Elsevier.

Lewis, R. W. & Ghafouri, H. R., (1997). A novel finite element double porosity model for multiphase flow through deformable fractured porous media. *International Journal for Numerical and Analytical Methods in Geomechanics*, 21, pp. 789-816.

Liu, Q. & Fan, H., (2012). The characteristics and estimation of flow through a single rough-walled fracture. *Journal of Hydrodynamics*, 24, pp. 315-322.

Lomize, G., (1951). *Water Flow in Jointed Rock*. Moscow: Gosenergoizdat.

Luo, S., Zhao, Z., Peng, H. & Pu, H., (2016). The role of fracture surface roughness in macroscopic fluid flow and heat transfer in fractured rocks. *International Journal of Rock Mechanics and Mining Sciences,* 87, pp. 29-38.

Mathews, M., (2010). *Installing Flow Meters on Dairies*. University of California.

Mèheust, Y. & Schmittbuhl, J., (2001). Geometrical heterogeneities and permeability anisotropy of rough fractures. *Journal of Geophysical Research*, 106 (B2), pp. 2089-2102.

Montazer, P. & Wilson, W. E., (1984). *Conceptual hydrologic model of flow in the unsaturated zone, Yucca Mountain, Nevada.* U.S Geological Survey.

National Research Council, (1996). *Rock Fractures and Fluid Flow: Contemporary Understanding and Applications*. Washington D.C.: National Academy Press.

National Research Council, (2001). *Conceptual Models of Flow and Transport in the Fractured Vadose Zone*. Washington DC: National Academy Press.

Nelson, R. A., Amoco, B. P. & Houston, T. X., (2001). *Geologic Analysis of Naturally Fractured Reservoirs*. 2nd ed. Boston: Gulf Professional Publishing.

Nicholl, M. & Glass, R., (2007). Wetting phase permeability in a partially saturated horizontal fracture. In: *Proceedings of 5th Annual International Conference on High Level Radioactive Waste Management*, pp. 22–26.

Nicholl, M., Glass, R. & Nguyen, H., (1992). Gravity-Driven Fingering in Unsaturated Fractures. In: *Proceedings of the Third Annual International Conference on High Level Radioactive Waste Conference, Las Vegas, Nevada, April 12-16.*

Nicholl, M. J. & Glass, R., (2005). Infiltration into an analogue fracture: Experimental observations of gravity-driven fingering. *Vadose Zone Journal*, 4, pp. 1123-1151.

Nicholl, M. J., Glass, R. J. & Nguyen, H. A., (1993). Wetting front instability in an initially wet unsaturated fracture. In: *Proc.4th Int. Conf. High Level Radioactive Waste Mgmt., 20161-2070, Las Vegas, April 26-30.*

Oron, A. & Berkowitz, B., (1998). Flow in rock fractures: the local cubic law assumption reexamined. *Water Resources Research*, 34(11), pp. 2811-2825.

Pearce, D., Crafford J., Riemann K., Hartnady C., Peck H. & Harris K., (2014). *The Economics of Sustainable Aquifer Ecosystem Services: A Guideline for the Comprehensive Valuation of Aquifers and Groundwater*. Water Research Commission.

Pruess, K., (1999). A mechanistic model for water seepage through thick unsaturated zones in fractured rocks of low matrix permeability. *Water Resources Research*, 35(4), pp. 1039-1051.

Qian, J., Zhan, H. B., Zhao, W. & Sun, F., (2005). Experimental study of turbulent unconfined groundwater flow in a single fracture. *Journal of Hydrology*, 311, pp. 134-142.

Ranjith, P. G. & Darlington, W., (2007). Nonlinear single-phase flow in real rock joints. *Water Resources Research*. https://doi.org/10.1029/2006WR005457.

Renshaw, C. E., (1995). On the relationship between mechanical and hydraulic apertures in rough-walled fractures. *Journal of Geophysical Research*. https://doi.org/10.1029/95JB02159: 629-636.

Richard, I. A., (1931). Capillary conduction of liquids through porous mediums. *Physics, Volume 1,* pp. 318-333.

Segole, K. P., Jones, B. R. & van Rooy, J. L., (2017). On the influence of varying aperture on flow mechanisms in an initially dry vertical smooth parallel fracture under free-draining conditions. In: *Proceedings of the 9th South African Young Geotechnical Engineers Conference, Durban, 13-15 September*.

Singh, K., Singh, D. & Gamage, R., (2016). Effect of sample size on the fluid flow through a single fractured granitoid. *Journal of Rock Mechanics and Geotechnical Engineering*, 8, pp. 329-340.

Singh, K., Singh, D. & Ranjith, P., (2015). Laboratory simulation of flow through single fractured granite. *Rock Mechanics and Rock Engineering*. https://doi.org/10.1007/s00603-014-0630-9.

Sketjne, E., Hansen, A. & Gudmundsson, J., (1999). High-velocity flow in a rough fracture. *Journal of Fluid Mechanics*, pp. 1-28.

Slokkte, D. T., (2010). *Surface roughness of natural rock fractures: implications for prediction of fluid flow*. PhD thesis, (unpub.). The University of Texas at Austin.

Su, G., (1999). *Flow Dynamics and Solute Transport in Unsaturated Rock Fractures*. PhD thesis, (unpub.). University of California.

Su, G. W., Geller, J. T., Pruess, K. & Wen, F., (1999). Experimental studies of water seepage and intermittent flow in unsaturated, rough-walled fractures. *Water Resources Research*, 35, pp. 1019-1037.

Tokunaga, T. K. & Wan, J., (1997). Water film flow along fracture surfaces of porous rock. *Water Resources Research*, 33(6), pp. 1287-1295.

Tokunaga, T., Wan, J. & Sutton, S., (2000). Transient film flow on rough fracture surfaces. Water Resources Research, 36, pp. 1737-1746.

Torsaeter, O. & Silseth, J. K., (1985). *The effects of sample shape and boundary conditions on capillary imbibition*. The Norwegian Institute of Technology, The University of Trondheim.

Tzelepis, V., Moutsopoulos, K. N., Papaspyros, J. N. A. & Tsihintzis, V. A., (2015). Experimental investigation of flow behaviour in smooth and rough artificial fractures. *Journal of Hydrology*, 521, pp. 108-118.

Von Scherenberg, N. L. & Seyler, H. G., (2012). Assessing the impact of saline intrusion with density dependent flow modelling for the fractured Peninsula Aquifer in Hermanus, South Africa. *Water Science and Technology*, 12, pp. 387-397.

Wang, J. S. & Narasimhan, T. N., (1985). Hydrologic mechanisms governing fluid flow in saturated, fractured porous media. *Water Resources Research*, 21, pp. 1861-1874.

Wang, J. S. & Narasimhan, T. N., (1993). Unsaturated flow in fractured porous media. In: *Flow and Contaminant Transport in Fractured Rock*, pp. 325-391.

Wang, J. S. Y. & Hudson, J. A., (2015). Fracture flow and underground research laboratories for nuclear waste disposal and physics experiments. In: B. Faybishenko, S. M. Benson & J. E. Gale, eds. *Fluid Dynamics in Complex Fractured-Porous Systems*. New Jersey: Wiley, pp. 21- 41.

Warren, J. & Root, P. J., (1963). The behaviour of naturally fractured reservoirs. *Society of Petroleum Engineers Journal*, 3, pp. 245-255.

Witherspoon, P. A., Wang, J. S. Y., Iwai, K. & Gale, J. E., (1980). Validity of cubic law for fluid flow in a deformable rock fracture. *Water Resources Research*, 16(6), pp. 1016-1024.

Witkke, W., (1990). Rock Mechanics -Theory and Applications with Case Histories. Springer.

Wittke, W., (2014). *Rock Mechanics Based on an Anisotropic Jointed Rock Model (AJRM)*. Wilhelm Ernst and Sohn.

Wu, Z., Fan, L. & Zhao, S., (2018). Effects of hydraulic gradient, intersecting angle, aperture, and fracture length on the nonlinearity of fluid flow in smooth intersecting fractures: an experimental investigation. *Geofluids.* https://doi.org/10.1155/2018/9352608.

Xia, C., Qian, X., Lin, P., Xiao W., Gui, Y., (2017). Experimental investigation of nonlinear flow characteristics of real rock joints under different contact conditions. *Journal*

of Hydraulic Engineering. https://doi.org/10.1061/(ASCE)HY.1943-7900.0001238.

Xu, Z., Zhao, Z., Sun, J. & Lu, M., (2015). Determination of hydraulic conductivity of fractured rock masses: A case study for a rock cavern project in Singapore. *Journal of Rock Mechanics and Geotechnical Engineering*, 7, pp. 178-184.

Yeo, I., (2001). Effect of contact obstacles on fluid flow in rock fractures. *Geosciences Journal*, 5, pp. 193-143.

Yin, Q., He, L., Jing, H. & Zhu, D., (2018). Quantitative estimates of nonlinear flow characteristics of deformable rough-walled rock fractures with various lithologies. *Processes*. https://doi:10.3390/pr6090149

Yong, R. Ye, J., Liang, Q., Huang, M. & Du, S., (2017). Estimation of the joint roughness coefficient (JRC) of rock joints by vector similarity measures. *Bulletin of Engineering Geology and the Environment*. https://doi 10.1007/s10064-016-0947-6.

Zhang, Z., Nemcik, J. & Ma, S., (2013). Micro- and macro-behaviour of fluid flow through rock fractures: an experimental study. *Hydrogeology Journal*, 21(8), pp. 1717-1729.

Zimmerman, R. W., Al-Yaarubi, A., Pain, C. C. & Grattoni, C. A., (2004). Non-linear regimes of fluid flow in rock fractures. *International Journal of Rock Mechanics and Mining Sciences*, 41, p. 384.

Zimmerman, R. W. & Bodvarsson, G. S., (1996). Hydraulic conductivity of rock fractures. *Transport in Porous Media*, 23, pp. 1-30

Appendices

Appendix A: Falling head permeability tests, hydraulic conductivity and moisture content data

Attached electronic file (IGL890.xl) includes:

- Shale falling head permeability test data
- Summary of all the shale falling head permeability test data
- Quartzite falling head permeability test data
-Summary of all the quartzite falling head permeability test data
- Moisture Content and unsaturated hydraulic conductivity data.

Appendix B: Average linear Velocity and Determination of Moisture Content

Average Linear Velocity: Shale

Inclination	Test no.	Hydraulic Head (mm)	Initially Dry Phase		Wetting Phase		Rewetting Phase	
			Time (s)	q_{Dry} (m/s)	Time (s)	q_{Wet} (m/s)	Time (s)	$q_{Rewetting}$ (m/s)
Horizontal	17	90	36	0.0233	42	0.0233	63	0.0242
		80	95	0.0233	101	0.025	116	0.0242
		70	154	0.0233	152	0.0242	164	0.0233
		60	215	0.0225	214	0.0233	224	0.0233
		50	280	0.0217	277	0.0233	289	0.0233
		30	411	0.0208	400	0.0225	415	0.0217
		20	478	0.02	458	0.0217	474	0.0217
		10	546	0.0196	522	0.0217	541	0.0208
		0	614	Stopped	587	Stopped	609	Stopped
	18	90	47	0.0183	77	0.0117	83	0.0125
		80	127	0.0175	187	0.0117	195	0.0117
		70	196	0.0167	296	0.0108	296	0.0117
		60	290	00167	439	0.0108	424	0.0117
		50	373	0.01583	560	0.01	533	0.0117
		30	540	0.015	816	0.01	775	0.0108
		20	626	0.015	940	0.0092	878	0.0108
		10	719	0.01417	1072	0.0092	998	0.01
		0	810	Stopped	1203	Stopped	1116	Stopped
23 Degrees	21	90	42	0.0333	42	0.0333	35	0.0333
		80	87	0.0333	86	0.0333	76	0.0333
		70	124	0.0325	126	0.0333	119	0.0333
		60	171	0.032	172	0.033	162	0.033
		50	213	0.0316	223	0.0325	213	0.0325
		30	329	0.03083	314	0.0316	304	0.0316
		20	366	0.03	360	0.0308	349	0.0308
		10	417	0.0283	409	0.0291	398	0.0291
		0	465	Stopped	461	Stopped	448	Stopped
	22	90	46	0.0333	44	0.0316	39	0.0325
		80	80	0.0333	90	0.0308	85	0.0316
		70	126	0.0325	134	0.0308	133	0.0316
		60	179	0.0325	187	0.0303	177	0.0308
		50	228	0.03167	239	0.03	233	0.0308
		30	324	0.0308	336	0.0286	324	0.0296
		20	374	0.0291	389	0.028	373	0.0283

		10	425	0.028	436	0.02667	427	0.0267
		0	478	Stopped	495	Stopped	477	Stopped
60 Degrees	25	90	33	0.0283	58	0.0253	56	0.025
		80	90	0.027	109	0.025	109	0.0241
		70	137	0.0266	159	0.025	164	0.0241
		60	189	0.0253	214	0.0246	220	0.0233
		50	250	0.025	279	0.0236	281	0.0233
		30	358	0.0233	392	0.023	399	0.0216
		20	418	0.023	451	0.0216	461	0.0213
		10	477	0.0216	516	0.0203	525	0.02
		0	546	Stopped	581	Stopped	589	Stopped
	26	90	57	0.0266	49	0.0246	58	0.0236
		80	105	0.0258	103	0.0241	114	0.0233
		70	153	0.025	159	0.0233	171	0.0233
		60	221	0.0246	218	0.0233	230	0.0225
		50	273	0.0236	282	0.023	298	0.022
		30	394	0.023	400	0.0216	420	0.0216
		20	446	0.023	460	0.0216	483	0.0208
		10	512	0.0225	527	0.0216	549	0.02
		0	580	Stopped	592	Stopped	618	Stopped
Vertical	29	90	64	0.0266	45	0.0233	43	0.0236
		80	99	0.0258	109	0.023	100	0.0233
		70	150	0.025	162	0.0225	156	0.0225
		60	208	0.0241	226	0.022	220	0.022
		50	266	0.0236	297	0.0216	297	0.02167
		30	380	0.023	427	0.0203	420	0.02
		20	445	0.0216	486	0.02	480	0.02
		10	508	0.0208	555	0.0186	550	0.0183
		0	574	Stopped	637	Stopped	628	Stopped
	30	90	52	0.0241	38	0.0216	63	0.0208
		80	109	0.0216	96	0.0208	124	0.0203
		70	169	0.0216	158	0.0203	187	0.02
		60	235	0.0208	228	0.02	257	0.02
		50	306	0.02	298	0.0196	329	0.0196
		30	449	0.0186	449	0.0183	475	0.0183
		20	516	0.01833	518	0.0175	541	0.0175
		10	592	0.0166	592	0.0166	619	0.0166
		0	667	Stopped	672	Stopped	698	Stopped

Where q= average linear velocity

*Stopped= when the valve was closed at the end of the test.; reading is regarded as an outlier to avoid any errors.

Average Linear Velocity: Quartzite

Inclination	Time (s)	Hydraulic Head (mm)	Initially Dry Phase		Wetting Phase		Rewetting Phase	
			Time (s)	q_{Dry} (m/s)	Time (s)	q_{Wet} (m/s)	Time (s)	$q_{Rewetting}$ (m/s)
Horizontal	17	90	0	0.075	23	0.0733	17	0.075
		80	26	0.075	39	0.0733	34	0.075
		70	36	0.075	57	0.0716	51	0.0733
		60	56	0.075	76	0.0716	72	0.0733
		50	76	0.0733	93	0.07	91	0.0716
		30	94	0.07	134	0.07	129	0.07
		20	133	0.0683	154	0.0683	148	0.0683
		10	153	0.066	175	0.0666	168	0.6666
		0	173	Stopped	190	Stopped	187	Stopped
	18	90	20	0.075	17	0.075	19	0.075
		80	40	0.075	33	0.075	36	0.0733
		70	57	0.0733	51	0.0733	54	0.0733
		60	75	0.0716	71	0.0733	74	0.0716
		50	101	0.0716	91	0.0716	91	0.0716
		30	135	0.07	130	0.07	133	0.07
		20	158	0.0683	150	0.0683	152	0.0683
		10	175	0.0667	170	0.0667	171	0.0666
		0	193	Stopped	189	Stopped	192	Stopped
23 Degrees	21	90	18	0.07	14	0.0683	13	0.0683
		80	40	0.07	33	0.0666	34	0.0666
		70	60	0.0683	53	0.0666	52	0.0666
		60	83	0.0683	77	0.0666	75	0.065
		50	100	0.0666	97	0.065	98	0.0633
		30	145	0.0633	139	0.0633	142	0.0616
		20	164	0.0633	162	0.0633	162	0.0616
		10	188	0.0616	184	0.0616	185	0.0583
		0	210	Stopped	207	Stopped	208	Stopped
	22	90	22	0.0683	16	0.0683	19	0.0683
		80	41	0.0666	34	0.0666	35	0.0683
		70	57	0.0666	54	0.0666	53	0.0666
		60	80	0.065	76	0.0666	77	0.0666
		50	103	0.065	97	0.065	98	0.065
		30	146	0.0633	141	0.0633	141	0.0633
		20	167	0.0616	163	0.0616	163	0.0616
		10	190	0.0583	186	0.0583	185	0.06
		0	214	Stopped	209	Stopped	209	Stopped
60 Degrees	25	90	22	0.0633	21	0.0633	22	0.065
		80	44	0.0633	39	0.0633	42	0.0633
		70	71	0.0616	56	0.0616	67	0.0616
		60	90	0.0616	85	0.0616	81	0.0583
		50	118	0.06	113	0.06	110	0.0583
		30	164	0.0583	165	0.0583	153	0.0583
		20	185	0.0566	179	0.0566	178	0.0566
		10	205	0.055	199	0.055	201	0.055
		0	215	Stopped	226	Stopped	228	Stopped
	26	90	24	0.065	20	0.065	24	0.065
		80	45	0.065	41	0.0633	43	0.0633
		70	66	0.0633	61	0.0633	63	0.0616
		60	88	0.0633	84	0.0616	87	0.0616
		50	114	0.0616	104	0.0616	111	0.06
		30	157	0.06	153	0.06	154	0.0583
		20	180	0.0583	176	0.0566	178	0.0566
		10	204	0.055	201	0.055	203	0.055
		0	228	Stopped	223	Stopped	228	Stopped
Vertical	29	90	18	0.0633	17	0.0633	21	0.0633
		80	38	0.0616	38	0.0616	42	0.0616
		70	59	0.0616	60	0.0616	63	0.06
		60	86	0.06	85	0.0616	87	0.06
		50	109	0.06	111	0.06	113	0.06
		30	156	0.0583	156	0.06	160	0.0566
		20	179	0.0566	179	0.0566	184	0.055
		10	206	0.0533	204	0.0533	208	0.0533
		0	230	Stopped	230	Stopped	235	Stopped

	30	90	19	0.0616	17	0.0616	17	0.0616
		80	41	0.0616	39	0.06	38	0.06
		70	62	0.06	65	0.06	62	0.06
		60	88	0.06	87	0.06	88	0.06
		50	114	0.0583	112	0.0583	113	0.0583
		30	161	0.0566	160	0.055	160	0.0566
		20	187	0.055	184	0.055	184	0.055
		10	211	0.0533	210	0.0516	211	0.0516
		0	235	Stopped	235	Stopped	237	Stopped

Where q= average linear velocity

*Stopped= when the valve was closed at the end of the test.; reading is regarded as an outlier to avoid any errors.

Moisture Content: Shale

Inclination	Test no.	$M_{cms}\ (g)$	$M_{cds}\ (g)$	$M_c\ (g)$	$M_w\ (g)$	$M_s\ (g)$	θ (%)
Horizontal (0°)	17	4580	4540	350	40	4190	0.9546
	18	4535	4500	350	35	4150	0.8433
	19	4545	4455	350	90	4105	2.1924
	20	4550	4495	350	55	4440	1.2387
23°	21	4555	4525	350	30	4495	0.6674
	22	4535	4495	350	40	4145	0.9650
	23	4535	4495	350	40	4145	0.9650
	24	4525	4495	350	30	4145	0.7238
60°	25	4525	4480	350	45	4130	1.0896
	26	4530	4500	350	30	4150	0.7223
	27	4535	4495	350	40	4145	0.9650
	28	4530	4530	350	35	4145	0.8444
Vertical (90°)	29	4540	4490	350	50	4140	1.2077
	30	4540	4495	350	45	4145	1.0856
	31	4545	4500	350	45	4150	1.0843
	32	4525	4475	350	50	4125	1.2121

Moisture Content: Quartzite

Inclination	Test no.	$M_{cms}\ (g)$	$M_{cds}\ (g)$	$M_c\ (g)$	$M_w\ (g)$	$M_s\ (g)$	θ (%)
Horizontal (0°)	17	11890	11885	350	5	11535	0.0433
	18	11890	11875	350	15	11525	0.1333
	19	11885	11875	350	10	11525	0.0868
	20	11880	11870	350	10	11520	0.0868
23°	21	11875	11870	350	5	11520	0.0434
	22	11875	11870	350	5	11520	0.0434
	23	11870	11865	350	5	11515	0.0434
	24	11870	11865	350	5	11515	0.0434
60°	25	11870	11865	350	5	11515	0.0434
	26	11870	11865	350	5	11515	0.0434
	27	11885	11865	350	20	11515	0.1737
	28	11870	11865	350	5	11515	0.0434
Vertical (90°)	29	11870	11865	350	5	11515	0.0434
	30	11870	11865	350	5	11515	0.0434
	31	11870	11865	350	5	11515	0.0434
	32	11870	11865	350	5	11515	0.0434

Appendix C: Aperture data and microscopy images

Shale 1

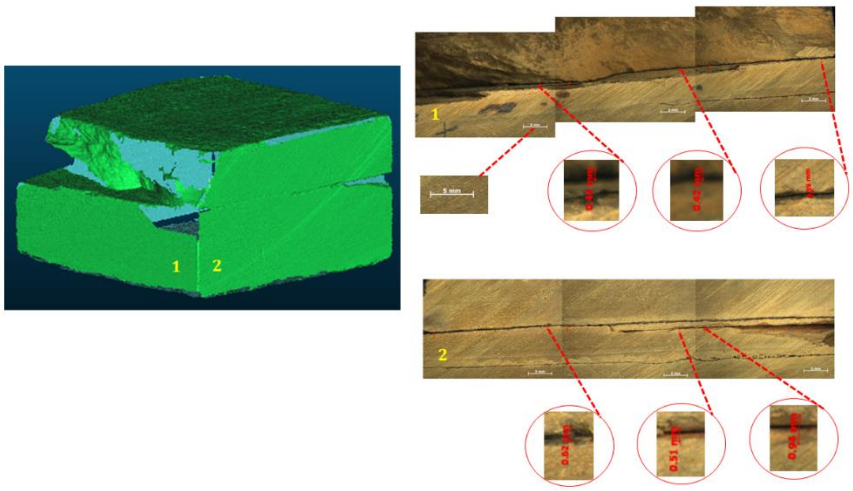

1. $Aperture_{avg} = \frac{0.45 + 0.42 + 0.39}{3} = 0.42\ mm$

2. $Aperture_{avg} = \frac{0.62 + 0.51 + 0.94}{3} = 0.69\ mm$

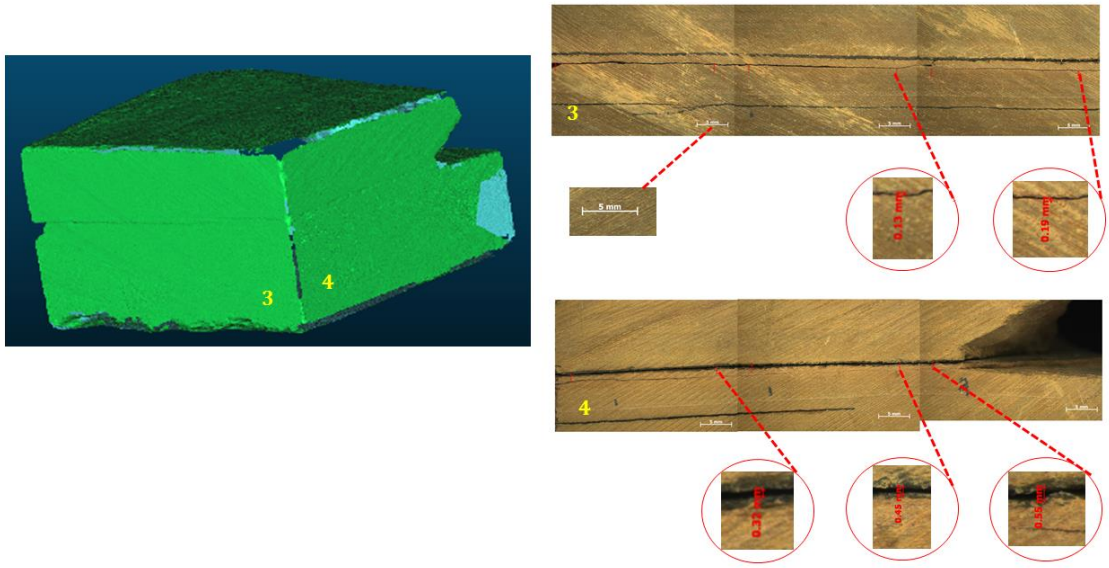

3. $Aperture_{avg} = \frac{0.13 + 0.19}{2} = 0.16\ mm$

4. $Aperture_{avg} = \frac{0.32 + 0.45 + 0.55}{3} = 0.44\ mm$

Shale 2

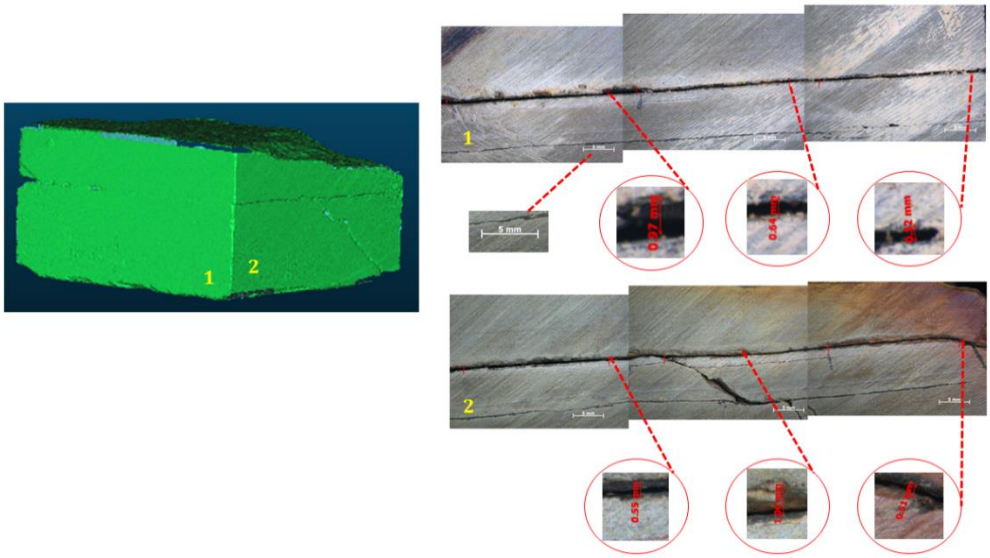

1. $Aperture_{avg} = \frac{0.97 + 0.64 + 0.52}{2} = 0.71\ mm$

2. $Aperture_{avg} = \frac{0.55 + 1.06 + 0.51}{3} = 0.70\ mm$

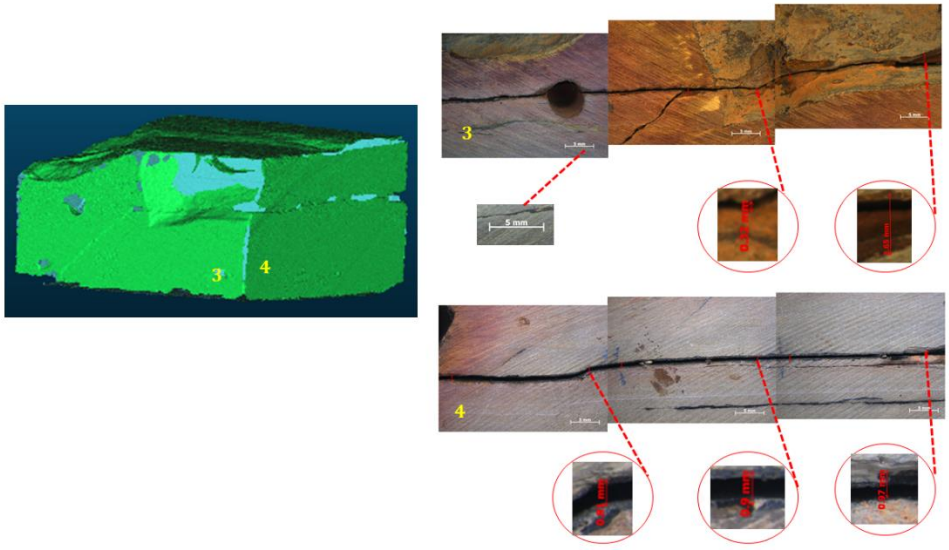

3. $Aperture_{avg} = \frac{0.32 + 2.65}{2} = 1.485\ mm$

4. $Aperture_{avg} = \frac{0.81 + 0.9 + 0.97}{3} = 0.89\ mm$

Quartzite 1

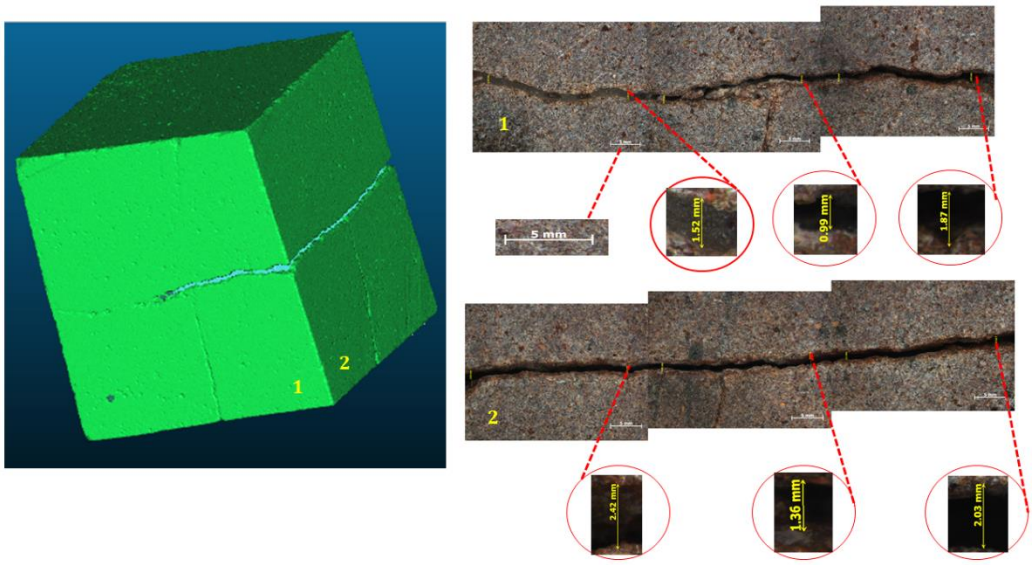

1. $Aperture_{avg} = \frac{1.52 + 0.99 + 1.87}{3} = 1.46\ mm$ 2. $Aperture_{avg} = \frac{2.42 + 1.36 + 2.03}{3} = 1.94\ mm$

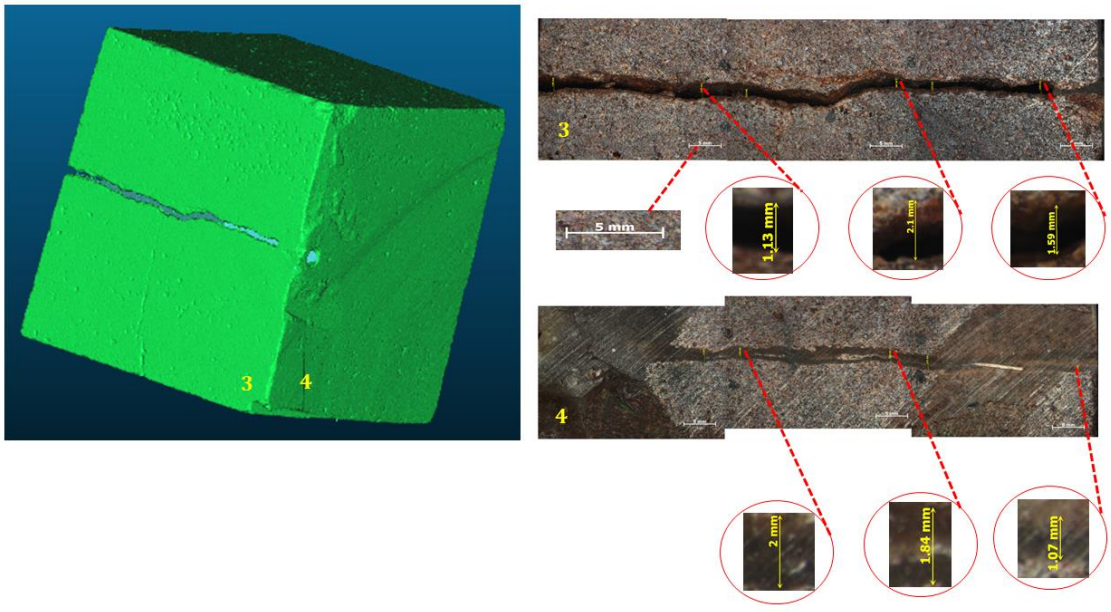

3. $Aperture_{avg} = \frac{1.13+2.1+1.59}{3} = 1.61\ mm$ 4. $Aperture_{avg} = \frac{2+1.84+1.07}{3} = 1.64\ mm$

Quartzite 2

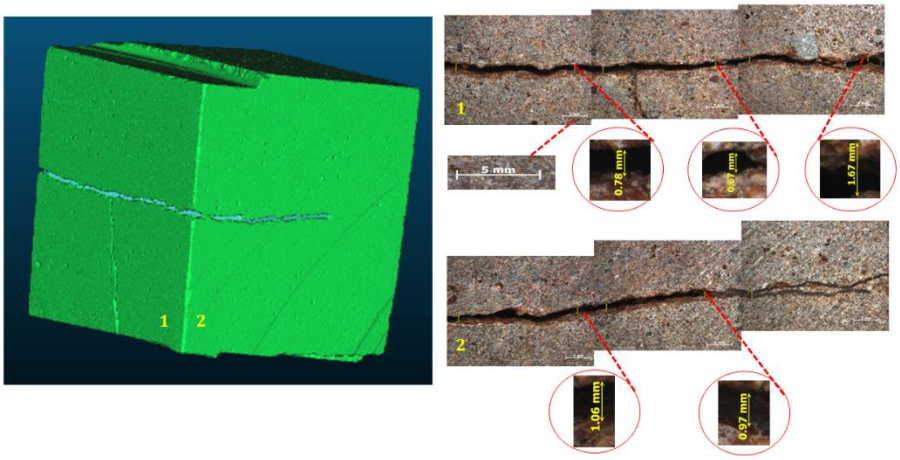

1. $Aperture_{avg} = \frac{0.78+0.67+1.67}{3} = 1.04\ mm$ 2. $Aperture_{avg} = \frac{1.06+0.97}{2} = 1.02\ mm$

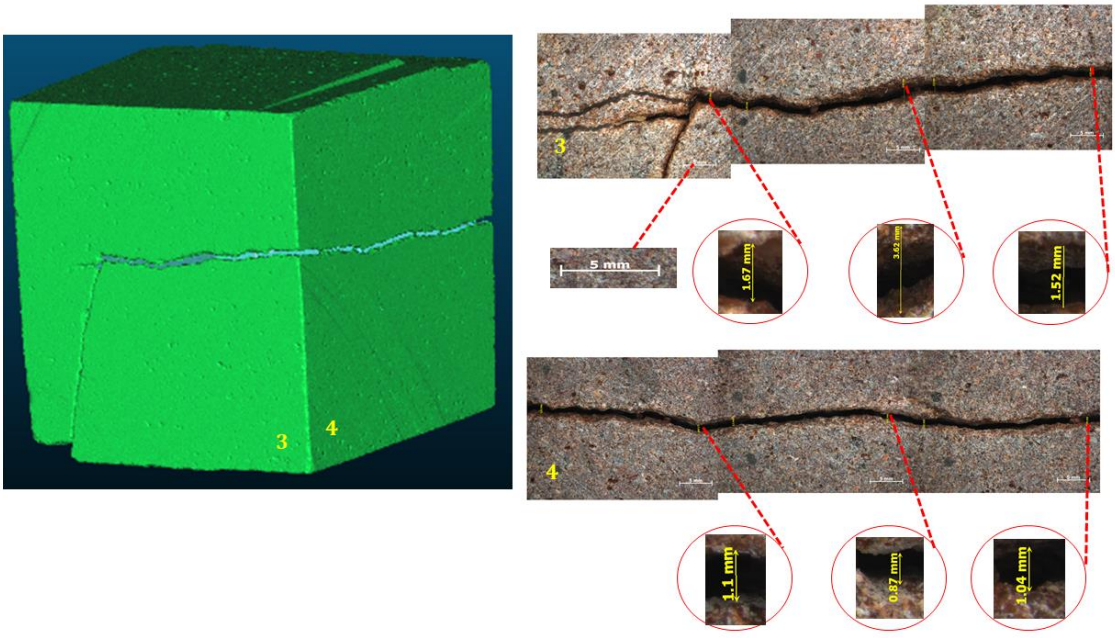

$Aperture = \frac{1.67+3.62+1.52}{3} = 2.27\ mm$ 4. $Aperture_{avg} = \frac{1.1+0.87+1.04}{3} = 1.003\ mm$

Appendix D: Joint Roughness Coefficient calculations

Quartzite-1

$$JRC = JRC_0 \left(\frac{l}{l_0}\right)^{-0.02JRC_0}$$

$\therefore JRC_{(up)} = 7\left(\frac{2}{0.1}\right)^{-0.02\times7} = 4.60$ $\quad\quad$ $\therefore\ JRC_{(down)} = 9\left(\frac{2}{0.1}\right)^{-0.02\times9} = 5.24$

$\therefore JRC_{(up)} = 8\left(\frac{2}{0.1}\right)^{-0.02\times8} = 4.95$ $\quad\quad$ $\therefore\ JRC_{(down)} = 6\left(\frac{2}{0.1}\right)^{-0.02\times6} = 4.18$

Quartzite -2

$$JRC = JRC_0 \left(\frac{l}{l_0}\right)^{-0.02JRC_0}$$

$\therefore JRC_{(up)} = 4\left(\frac{2}{0.1}\right)^{-0.02\times4} = 3.148$ $\quad\quad$ $\therefore\ JRC_{(down)} = 5\left(\frac{2}{0.1}\right)^{-0.02\times5} = 3.706$

$\therefore JRC_{(up)} = 4\left(\frac{2}{0.1}\right)^{-0.02\times4} = 3.148$ $\quad\quad$ $\therefore\ JRC_{(down)} = 6\left(\frac{2}{0.1}\right)^{-0.02\times6} = 4.18$

Shale-1

$$JRC = JRC_0 \left(\frac{l}{l_0}\right)^{-0.02JRC_0}$$

$\therefore JRC_{(up)} = 1\left(\frac{10}{0.1}\right)^{-0.02\times1} = 0.912$ $\quad\quad$ $\therefore\ JRC_{(down)} = 1\left(\frac{10}{0.1}\right)^{-0.02\times1} = 0.912$

$\therefore JRC_{(up)} = 2\left(\frac{2}{0.1}\right)^{-0.02\times2} = 1.664$ $\quad\quad$ $\therefore\ JRC_{(down)} = 2\left(\frac{2}{0.1}\right)^{-0.02\times2} = 1.66$

Shale- 2

$$JRC = JRC_0 \left(\frac{l}{l_0}\right)^{-0.02JRC_0}$$

$$\therefore JRC_{(up)} = 3\left(\frac{10}{0.1}\right)^{-0.02\times3} = 2.276 \qquad \therefore\ JRC_{(down)} = 2\left(\frac{10}{0.1}\right)^{-0.02\times2} = 1.664$$

$$\therefore JRC_{(up)} = 2\left(\frac{2}{0.1}\right)^{-0.02\times2} = 1.774 \qquad \therefore\ JRC_{(down)} = 4\left(\frac{2}{0.1}\right)^{-0.02\times4} = 3.147$$